Experimental investigation of electrokinetic phenomena in planar and porous substrates

by

Rakesh Saini

A thesis submitted to the

Graduate Program in the Department of Chemical Engineering

in conformity with the requirements for

the degree of Master of Applied Science

Queen's University

Kingston, Ontario, Canada

June 2014

Abstract

Nowadays, there are various electrokinetic phenomena which are utilized in a wide range of applications, ranging from microfluidics and colloid and interface science to electrochemistry. However, even after 200 years of research on electrokinetic phenomena, there are still open questions with respect to fundamental understanding. The focus of this thesis is on three different phenomena, i.e., streaming potential, streaming current and electroosmosis. Hence, the thesis is divided in two parts:

The first part focuses on the applicability of the classical Helmholtz-Smoluchowski theory on streaming potential and streaming current measurements of poly(methyl methacrylate) (PMMA) wafers, to infer the zeta potential of this substrate in contact with liquids of defined pH and ionic strength. In detail, we perform electrical impedance spectroscopy measurements to infer the electrical resistance in a PMMA microchannel and derive novel correlations for the electrokinetic characterization of the substrate. We conclude that convection can have a significant impact on the electrical double layer configuration which is reflected by changes in the surfaces conductivity.

The second part of the thesis is concerned with electroosmotic flows in porous substrates where we develop a phenomenological correlation which is based on dimensional reasoning. A large set of experiments is carried out using a relatively simple and cost-effective setup including different sintered packed beds of borosilicate microspheres. A centre-of-mass model of the experimental setup allows for the interpretation of various effects. Streaming current measurements result in a correlation for the zeta potential of borosilicate depending on ionic strength and pH of the liquid. Finally, a quantitative expression for electroosmotic flow in packed beds of granular material is derived from the experiments. This correlation can be employed with other materials as well.

Co-Authorship

The work presented in this thesis was accomplished under the supervision of Dr. Dominik P. J. Barz, who provided continual feedback and corrections to the manuscript. He also provided additional contributions by drafting a few sections of the articles and then further revising them critically for important intellectual content. All the work related to conception, design of experiments, acquisition of data, analysis and interpretation of data was performed in a substantial way under my supervisor's guidelines. The manuscript will further be improved to provide a final format to be published into a journal article.

Acknowledgments

Table of contents

List of Tables

List of Figures

List of Abbreviations

AC   Alternating current

DC   Direct current

DI   De–ionized

DL   Diffuse layer

EDL   Electrical Double Layer

EEC   Equivalent electrical circuit

EIS   Electrical impedance spectroscopy

EKC   Electrokinetic cell

EO   Electroosmosis

EOF   Electroosmotic flow

EOP   Electroosmotic pump

HS   Helmholtz-Smoluchowski

LDEP   Laser doppler electrophoresis

ODE   Ordinary differential equation

PFA   Perfluoroalkoxy alkane

PMMA Poly(methyl methacrylate)

PTFE   Polytetrafluoroethylene

RC   Resistance-Capacitance

SC   Streaming current

SL   Stagnant layer

SP   Streaming potential

ZP   Zeta potential

List of Symbols

$\Delta\varphi_{SP}$ Streaming potential $[m^2kgs^{-3}A^{-1}]$

Ω_i Dimensionless group numbers for capillary force balance [-]

Φ Dimensional analysis correlation function [-]

Π Preliminary dimensionless group [-]

β Charge transfer coefficient [-]

δ Ratio of particle diameters [-]

ϵ Electrical permittivity of the medium $[m^{-3}kg^{-1}s^4A^2]$

μ Viscosity of the medium $[m^{-1}kgs^{-1}]$

ψ Porosity of the packed bed [-]

ρ Density of the medium $[m^{-3}kg]$

σ_B Bulk conductivity $[m^{-3}kg^{-1}s^3A^2]$

σ_S Surface conductivity $[m^{-3}kg^{-1}s^3A^2]$

σ_o Surface tension of the liquid/air interface $[kgs^{-2}]$

σ_{DL} Diffuse layer surface conductivity $[m^{-3}kg^{-1}s^3A^2]$

θ Contact angle of the liquid/air interface$[rad]$

θ_D Dynamic contact angle of the liquid/air interface$[rad]$

θ_e Static equilibrium contact angle of the liquid/air interface$[rad]$

φ_i Electrical potential $[m^2kgs^{-3}A^{-1}]$

ζ Zeta potential of the substrate $[m^2kgs^{-3}A^{-1}]$

Nomenclature

$A_{xy/p}$ Cross-section area of section xy or element p $[m^2]$

C_i Capacitance of element i $[m^{-2}kg^{-1}s^4A^2]$

D Large particle diameter $[m]$

Du Dukhin number, $\sigma_S/(\sigma_B h_2)$ [-]

E Electric field strength $[mkgs^{-3}A^{-1}]$

F Faraday constant, 96485.33 $[sAmol^{-1}]$

F_j Force term due to j effect $[mkgs^{-2}]$

I Ionic strength $[m^{-3}mol]$

I_C Conduction current $[A]$

I_{SC} Streaming current $[A]$

K_1 Proportional constant in Blake-Kozeny equation [-]

M Factor for wall effect [-]

PB Packed-Bed number [-]

P_c Wetted perimeter of channel/pore cross section $[m]$

RW Rice-Whitehead number [-]

R_T Electron transfer resistance $[m^2kgs^{-3}A^{-2}]$

R_g Universal gas constant, 8.314 $[m^2kgs^{-2}K^{-1}mol^{-1}]$

R_i Ohmic resistance of element i $[m^2kgs^{-3}A^{-2}]$

R_{2B} Bulk resistance $[m^2kgs^{-3}A^{-2}]$

R_{2S} Surface resistance $[m^2kgs^{-3}A^{-2}]$

R_μ Viscous flow resistance $[m^{-4}kgs^{-4}]$

Re Reynolds number, $(\rho v D)/\mu$ [-]

S_L Wetted surface area per bed length $[m]$

S_v Surface area per unit volume $[m^{-1}]$

Sm Electroosmotic Smoluchowski Number [-]

V_{eof} Dimensionless EOF velocity [-]

V_{xy}	Volume of the xy compartment of the 1D EOF set-up $[m^3]$	
Z_{if}	Dimensionless z–coordinate of the liquid/air interface $[-]$	
ΔR_2	Resistance change $[m^2 kg s^{-3} A^{-2}]$	
Δp	Pressure difference $[m^{-1} kg s^{-2}]$	
Δp_{xy}	Pressure difference due to xy process $[m^{-1} kg s^{-2}]$	
$\bar{T}$	Absolute temperature $[K]$	
$\bar{U}$	AC voltage $[m^2 kg s^{-3} A^{-1}]$	
$\bar{Z}$	Impedance $[m^2 kg s^{-3} A^{-2}]$	
$\bar{z}_i$	Valency of the ion i $[-]$	
$\dot{V}_{eof}$	EO volumetric flow rate $[m^3 s^{-1}]$	
$\dot{V}$	Volumetric flow rate $[m^3 s^{-1}]$	
c_i	Concentration of the ion i $[m^{-3} mol]$	
cp	Index for capillary $[-]$	
d	Small particle diameter $[m]$	
d_h	Hydraulic diameter $[m]$	
d_i	Diameter of the particle size i $[m]$	
d_p	Effective particle diameter $[m]$	
d_{pb}	Diameter of the packed bed $[m]$	
$d_{x,i}$	Inner diameter of the x component $[m]$	
el	Electrode index $[-]$	
f	Frequency $[s^{-1}]$	
g	Gravity constant, 9.81 $[m s^{-2}]$	
h_2	Microchannel height $[m]$	
h_{eq}	Equilibrium height in the capillary $[m]$	
j_S	Surface current density $[m^{-1} A]$	
j_o	Exchange current density $[m^{-2} A]$	

l_2	Microchannel length $[m]$
l_D	Debye length of the medium $[m]$
l_{xy}	Length of the xy compartment of the 1D EOF set-up $[m]$
m	Number of physical dimensions [-]
n	Number of physical quantities [-]
q	Correlation function for dimensional analysis [-]
$r_{x,o}$	Outer radius of the x component $[m]$
r_{xy}	Radius of the xy component $[m]$
rv	Index for Reservoir [-]
t	Time $[s]$
t_r	Charge relaxation time $[s]$
v	Velocity of the liquid in capillary $[ms^{-1}]$
v_+, v_-	Absolute ion mobility of cation and anion $[kg^{-1}s^2A]$
v_d	Small particle volume fraction [-]
v_{eof}	Superficial electroosmotic velocity $[ms^{-1}]$
vis	Index for viscous term [-]
w_2	Microchannel width $[m]$
w_i	Weight fraction of particle size i [-]
x	Downstream direction in micro channel [m]
x_i	Number fraction of the particle size i [-]
z	Coordinate system w.r.t. bottom of the capillary $[m]$
z_c	z–coordinate of the center of mass of the capillary system $[m]$
z_{if}	z–coordinate of the liquid/air interface $[m]$
z_{xy}	z–coordinate of the xy compartment of the 1D EOF setup $[m]$

Chapter 1

Introduction

The purpose of this introduction is to establish an overarching framework for our research. Hence, here we give a brief introduction into selected fundamental aspects of the involved phenomena which are not entirely covered in the manuscript parts of this thesis.

Research on electrokinetic phenomena dates back to the beginning of the 19th century, when F. F. Reuss, for the first time carried out experiments which were published in 1809. Reuss used a U-tube which was filled with a plug of clay and observed a flow when he applied a voltage across the plug. In terms of modern terminology, these electrically-induced flow experiments are the first known study of the electrokinetic phenomenon of electroosmosis. Also, the discovery of the phenomenon of electrophoresis , i.e., the migration of charged species (here the clay particles) under the influence of a voltage, can also be attributed to the work of Reuss.

Later, Gustav Wiedemann published a paper in 1852 to quantitatively describe electroosmosis (as noted by Wall et al. [1]). This was more than a half century before the Smoluchowski equation was established, which is nowadays considered as one of the original equations for electrokinetics. The next important discovery in the field of electrokinetics came in 1859, when the physicist Georg Quincke observed the generation of an electrical potential when water was pumped through plugs of porous material, the so-called streaming potential. These different observations required a universal theory, which was introduced by the concept of a space charge in the liquid adjacent to the charged solid surface. That is, there is a liquid volume (space) where there is an excess of charges (counter-ions), which are oppositely charged to those of the surface.

This space charge theory is considered the foundation for the concept of the electrical double layer (EDL) which was first quantitatively described by H. von Helmholtz in 1879. Helmholtz used the concept of a capacitor to describe the characteristics of the space

charge. By 1880, all the "classical" electrokinetic phenomena - electroosmosis, electrophoresis, streaming potential/current and sedimentation potential were discovered [1]. Brief details about the early history of these phenomena can be obtained from review articles published in the last years[1, 2].

1.1 Electrical double layer

The introduction of the electrical double layer concept allowed for the explanation of electrokinetic phenomena as well as other effects like aggregation of charged particles due to electrostatic interactions. The capacitor based model of Helmholtz was later expanded by Gouy 1910, who introduced the concept of a diffusive charge layer. The same concept was independently proposed by D. L. Chapman in 1913 [1]. Hence, the model is commonly referred to as the Gouy-Chapman (GC) model. Essentially, the diffusive layer theory proposes that the distribution of the ions in the EDL is due to the equilibrium of the (attractive/repulsive) electrostatic forces and the dispersive influence of thermal diffusion (Brownian motion). That is, the distribution in the EDL can be described by a Boltzmann approach. Nowadays, a modified GC model is commonly used which was introduced by Stern in 1924. Stern proposed that adjacent to the surface, the electrostatic interactions must have a stronger influence and there must be a layer of somewhat immobile ions adjacent to the diffusive layer. This model is called the Gouy-Chapman-Stern (GCS) model.

Figure 1.1 illustrates the configuration of this EDL model. Essentially, at the wall there is a layer of immobile adsorbed counter-ions (Stern layer). Adjacent to that, there is a layer of counter-ions with a decreased mobility which is usually referred to as the shear plane. The next layer is the diffusive layer. This layer consists not only of counter-ions but also has a considerable fraction of co-ions. All these liquid layers do not fulfill the electro-neutrality condition, in contrast to the bulk liquid. The potentials associated with the different layers are illustrated in figure 1.1 as well. At the surface, the potential is

Stern Shear
Layer Plane ── Diffuse Layer

Bulk Liquid

Negatively Charged Solid Surface

y_o y_s y_z l_D y_d y

Distance

Surface Pot.

Ψ_w Stern Pot.

Ψ_s Zeta Pot.

ζ

Potential

y_o y_s y_z y y_d
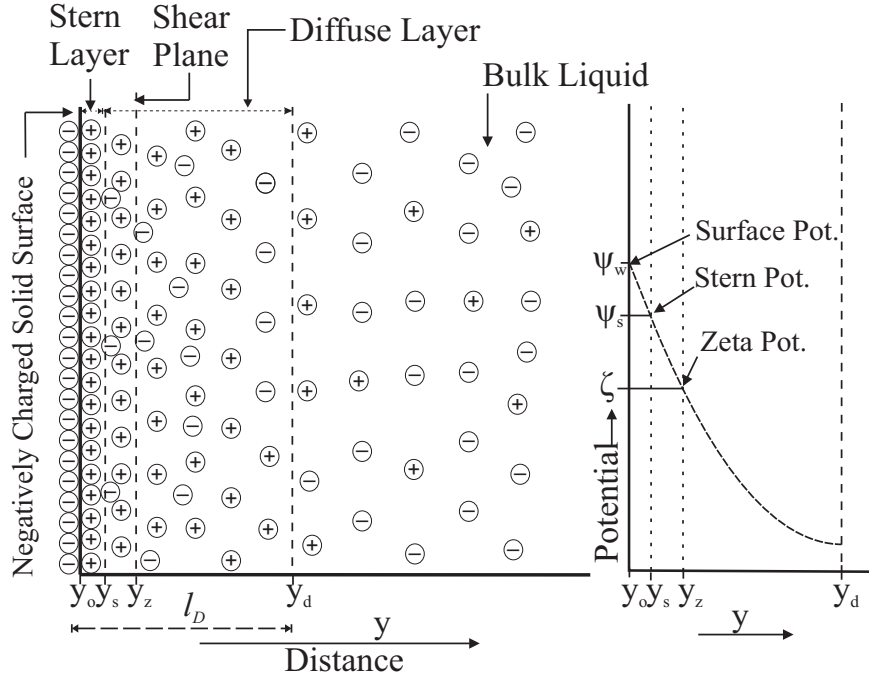
Figure 1.1: Sketch of an electric double layer according to the GCS model.

called surface potential and solely describes the presence of the surface charges. This value can usually not be measured. The potential at the Stern layer is accordingly called Stern potential and describes the influence of the surface charge diminished (shielded) by the layer of adsorbed ions. Finally, the potential at the shear plane, which is the central quantity in electrokinetics, is called zeta potential and is the only potential which can be determined by the measurement of electrokinetic phenomena. Another important parameter of an EDL is the so-called Debye length which gives an estimation of the thickness of the diffuse layer. A quantitative correlation for the Debye length can be derived from the Poisson-Boltzmann equation.

Previous decades have seen different interpretations of the electric double layer theory together with experimental and analytical studies, but the most largely accepted model is still the Gouy-Chapman-Stern (GCS) model because of its simplicity and analytical approach, as stated by Henderson et al. [3]. In the following, we review some literature which

is concerned with the surface conductivity and the influence of the Stern layer since these are important aspects for the first part of this thesis. The reviewed work is generally concerned with surfaces of colloidal particles; but it also applies to the planar surfaces that we utilize in this thesis.

1.1.1 Stern layer structure and surface conductivity

Lyklema et al. [4] provides a review on different aspects of surface conductivity in electrokinetics. The surface conductance is defined as an excess local charge which originates due to the presence of the EDL. Since only mobile charges can contribute to the surface conductivity, the surface conductivity provides information about the dynamic properties of the EDL. The Dukhin number (Du) is a dimensionless parameter which defines the relative importance of the surface conductivity compared to the bulk conductivity of the liquid. The Du number depends on the zeta potential, the concentration of the electrolyte solution and typical geometrical dimensions such as the particle diameter or the channel height. Bikerman first introduced an analytical equation to calculate the surface conductivity, however, it was based on the structure of the diffuse layer only (as cited by [5]).

In the GCS model, the Stern layer is considered as a static layer of adsorbed ions along with solvent molecules which are present due to chemical and physical interactions between the electrolyte solution and the surface. This layer is usually assumed to be unaffected by the liquid movement, contrary to the liquid and ions within the diffuse layer which move in the presence of an electric field, pressure or ion concentration gradient. However, there is literature which claims that the Stern layer consists of charges with a decreased but still present mobility. Consequently, if there are somewhat mobile ions in the Stern layer, they should move under the influence of an electrical field likewise to the ions in the diffuse layer.

Hence, the surface conductivity results from a combination of both the diffuse and the inner layers of the EDL. An early approach to include the stagnant layer contribution was

made by Urban [6] who discussed the effect of surface conductivity on various electroki-
netic phenomena and developed an equation for the surface conductivity including the ion
transport in the Stern layer.

Saville et al. [7] observed discrepancies for the zeta potential values of polymer lattices,
obtained from the measurement of the suspension conductivity and the electrophoretic mo-
bility which could not be explained by the change in the fluid viscosity and the dielectric
constant in the Stern layer. He proposed a model which is based on a lateral ion transport
in the Stern layer. As noted by Saville et al. [7], there were also some earlier attempts by
Henry (1948), Dukhin (1983) and van der Put (1983) where they consider the effect of sur-
face conductivity respectively on electrophoretic mobility, dielectric properties of colloidal
suspensions and observed electrokinetic data on porous plugs. But most of these models
either lacked the details regarding the ion transport processes involved in the Stern layer
or were modeled in an approximate way. The dynamic model proposed by the Saville et al.
considers the existence of an equilibrium between the ions in the diffuse layer and those in
the Stern layer. Therefore, the polarization of ions in one layer affects the ion distribution
in the other layer. This mathematical model of Stern layer ion transport, which was later
applied successfully to interpret their own experimental results [8], was explained on the
basis of ion-conduction inside the Stern layer due to an applied electric field as well as ion
diffusion due to a concentration gradient. Inspired by Saville et al.'s work, L.R. White et al.
[9] developed a new model where the effect of the ion transport in the Stern layer of colloidal
particles is treated in a different fashion. They studied the overall effect of the Stern layer
ion transport in conjunction with adsorption models on the electrophoretic mobility and on
the electrical conductivity. They take into account the specific surface interaction forces in
the Stern layer as well as the viscous, electrostatic and thermodynamic forces acting on the
ions while modeling a mobile Stern layer structure.

In their paper concerned with the properties of the stagnant (Stern) layer, Lyklema et
al. [10] emphasized the importance of ionic conduction in the stagnant layer for different

electrokinetic phenomena. They observed only a slight difference between the tangential mobilities of counter-ions in the bulk to those in the stagnant layer which they also found in agreement with the experimental evidence [4]. Based on molecular dynamics simulations, they studied the mobilities of ions under the influence of an external electric field and observed that the contribution of the stagnant layer to the charge transport in the bulk cannot be neglected. It was found that the (stagnant layer) ions move in parallel to the solid surface and remain comparatively slow but not static.

R.J. Hunter [11] analyzed the importance of the stagnant layer conduction while studying different electrokinetic phenomena of colloidal particles. They predict that the stagnant layer conduction occurs in some but not all systems; an assumption which is based on their low frequency surface conduction measurements. However, the author admits that this technique is not simple and can result in considerable errors.

Joly et al. [12] simulate the hydrodynamics of the EDL as a function of the wettability of different charged planar surfaces. A major deviation from the model of a static Stern layer is observed in the case of non-wetting surfaces where the electrokinetic effects becomes highly pronounced due to the occurrence of a velocity slip at the solid surface which results in an increased zeta potential value.

To summarize, there is literature which claims that the Stern layer is not entirely stagnant. That is, the ions in this layer have a finite mobility and contribute to the effect of surface conductivity. However, there are discrepancies regarding the relevance of this Stern layer conduction. Also, the majority of the work is of a theoretical nature and concerned with single particles and there are only limited experimental results which support these sophisticated theories. In the first part of this thesis, we focus on the streaming current and the streaming potential method to infer the zeta potentials of Poly(methyl methacrylate) (PMMA) wafers and consider the surface conductivity. Hence, we proceed this thesis by a further discussion of the streaming current and the streaming potential. For the sake of simplification, we restrict the discussion to microchannels.

1.2 Streaming current and streaming potential

The **streaming current** is the convective current which is generated in the EDL due to the transport of counter-ions induced by an external force field, such as a pressure gradient, which induces a liquid flow. To calculate the streaming current, the current density i.e. the product of liquid velocity and charge density, is integrated over the whole cross sectional area of the channel. The streaming current is usually observed to be proportional to the applied pressure gradient for a given liquid concentration. The streaming current can only be measured if two electrodes are inserted in the channel. The electrodes are connected through a very low resistance external circuit; i.e., in short circuit condition.

The **streaming potential** phenomenon also arises when a liquid is forced to move through the channel. If the electrodes are connected to a voltmeter having high resistance, i.e., rather an open circuit condition, the streaming current results in a local accumulation of charge which must be accompanied by a spatial potential difference which is called streaming potential. The generation of the streaming potential across the channel results in a conduction current. The assumption that the conduction current occurs only in the bulk liquid, results in erroneous values for the zeta potential measurements. Therefore, the surface conductivity term should be included in the total conduction [13].

1.2.1 Some important considerations for the measurement of streaming current and streaming potential.

As mentioned by van Wagenen [14], a critical condition to measure the streaming potential values accurately is to establish a steady, developed laminar flow in the channel. The author achieved all these conditions by developing a parallel, flat plate configuration. This "micro slit" essentially has dimensions that allows, to good approximation, for the application of a one dimensional flow. This novel cell configuration proved its importance for the measurement of zeta potential values in the subsequent years compared to other streaming

measurement methods which included long capillary tubes, porous plugs of micro-particles or fibers. Considering the importance of this cell design in a very accurate quantitative surface characterization, it has been used by several researchers with slight modifications [15–17]. In this work, we also use a similar cell configuration.

As mentioned by Voigt [18], during the measurements of streaming potential and streaming current on surfaces covered with charged layers, the surface conduction is usually neglected for solutions having a concentration more than $10^{-3}M - 10^{-4}M$ due to decrease in EDL thickness. Though this is done for surfaces having moderate potentials and for bulk liquid volumes which are sufficiently large compared to the surface area.

Another problem with respect to the measurement of the streaming potential is the so-called electrode polarization as pointed out by Korpi et al. [19], which can alter the streaming potential values to a significant degree. Electrode polarization occurs if charges accumulate in the vicinity of the electrode. If these charges are not consumed by an electrode reaction, a potential gradient induces a conductive current which falsifies the measurement of the streaming potential. Therefore, in the current work, we use reversible Ag/AgCl electrodes which are frequently renewed while using both low and high salt concentrations.

1.2.2 Electrical impedance spectroscopy for in-situ cell characterization

It is important to understand all the electrical processes which are involved in the measuring of streaming current and potential. Therefore, we employ electrical impedance spectroscopy (EIS) to investigate various electrical quantities such as the electrode charge transfer resistance and the ohmic resistance of the solutions. EIS has found applications in studying different processes such as corrosion as well as electrochemical reactions in batteries and fuels cells [20]. While performing EIS measurements, a potentiostat can be used either in a two electrode mode or in a three electrode mode depending on the requirement. For the work done in the first part of this thesis, we perform various EIS measurements using two electrodes where one electrode functions as the working electrode and the other one as

the counter electrode. Here, a constant small AC voltage is applied over a wide range of frequencies without creating any adverse effects on other processes. This applied voltage results in the generation of an AC current signal. The impedance of the circuits is determined by dividing the applied voltage by the current generated at the same frequency.

The results of an EIS experiment can be represented in two ways; a Nyquist plot or a Bode plot. In Nyquist plots, the real and imaginary parts of the impedance values are plotted on the X-axis and on the Y-axis, respectively. Each point on the curve represents the total impedance of the system. Unlike Nyquist plots, the Bode plot gives the absolute values of the total impedance and the phase shift on log-log charts versus the respective frequency values.

The EIS measurements can be fitted to an equivalent electrical circuit diagram, where different circuit elements such as resistors, capacitors and inductors can be modeled depending on the physical, electrochemical behavior of the system. In the first part of this thesis, we use a Nyquist plot to calculate different impedance values of the measurement cell measured at various experimental conditions.

We are not aware of any work which employs EIS for the electrical characterization but that of Ariza et al. [21]. In this work, the authors performed the electrokinetic characterization of active layers of nano filtration membranes to calculate parameters such as ion transport numbers, fixed charge concentration, solution resistance and zeta potential by streaming potential measurements. Here, they fit equivalent circuits for the obtained impedance curves showing three sub-circuits with each having resistance and capacitor in parallel. These three circuits represent elements for the electrolyte solution, the active layer of the membrane and the membrane porous sub-layer, each calculated for a different frequency range. However, the results of the soft and complex membrane surface cannot easily be transferred to the rigid microchannel that we use in our work.

1.3 Electroosmosis

In the second part of this thesis, we investigate electroosmosis in packed beds of granular (spherical) material for different experimental conditions. Here, we briefly discuss some relevant phenomena -

The term **electroosmosis** refers to the induced motion of a (bulk) liquid when an external electric field is applied tangentially to the EDL. That is, the electrical field drives the ions in the EDL and the liquid outside of the EDL is dragged by viscous interactions. Electroosmosis can be utilized to pump liquids with an absence of moving/mechanical parts which is especially beneficial for small scale applications. This and other advantages compared to conventional pumps result in a broad range of potential applications in microfluidics such as point-of-care testing [22], drug delivery [23] as well as energy applications such as micro fuel cells [24, 25]. In this regard, the utilization of porous structures in micro- and nano-scale devices is especially beneficial since relatively high flow rates along with high pump pressures can be induced. Here, the major advantage of utilizing porous structures lies in the large (active) interface area per unit volume which makes the electrokinetic phenomena more prominent. The Smoluchowski equation can be used to calculate the electroosmotic velocity in a pore where the channel size is large enough to ignore the EDL distortion due to the applied electric field and therefore, electric and hydrodynamic field lines are considered parallel [26]. But in the case of pores with sophisticated and/or unknown pore geometries, it becomes quite difficult to infer the change in the electric field and velocity profile quantitatively on a microscopic level where the EDL overlap might also take place. Hence, we carry out several EOF experiments to observe these phenomena on a macroscopic level by applying external electric fields to porous beds having different structural characteristics.

1.3.1   Joule heating during EOF

Electrokinetic flow is considered to be a significantly improved way of generating flow of liquids and samples in microfluidic devices as compared to pressure regulated flows. But the inevitable effect of Joule heating related to the application of the electric field creates flow disturbances due to non-uniform temperature distributions. Here, the heat generation occurs due to the flow of an electric current through the liquid electrolyte which has a resistive value depending on its ionic concentration and the dimensions of the channel. The heat generated is proportional to the square of the current flowing through the channel. The amount of heat also linearly scales with the duration of the electric field (electroosmotic flow). The induced temperature gradient influences most properties of the liquid such as permittivity, density and viscosity. Usually, the electroosmotic flow profile is considered as a plug-like velocity profile but in the presence of Joule heating it deviates from that, which can have negative impacts for lab-on-a-chip analytics [27]. Several numerical and analytical investigations have been done to predict the influence of Joule heating in single microchannels. Xuan [27] developed an analytical model to show the effect of Joule heating not only on heat and mass transport but also on momentum and species transport in capillaries. The temperature gradient induces an additional flow with concave and convex flow patterns, depending on the flow conditions.

Another important phenomenon related to the application of high electric fields is the pH change which can have a significant effect on micro channel flow. Laszlo et al. [28] observed a change in pH due to electrochemical hydrolysis of water at the electrodes during the generation of electrokinetic flow. The authors predict a strong dependency of the EOF on the pH of the electrolyte in case of silica and glass surfaces. This change can be suppressed by renewing the electrolyte regularly or by adding a sufficient amount of buffer solution. Other researchers like Bello et al. [29] also support this observation by simulation of the electric current in capillary electrophoresis and its influence on the pH value and the

composition of the electrolyte. The accompanying experiments by Bello et al. show a good agreement with the results predicted by theory. In the case of capillary electrophoresis, the pH change affects the electrochromatographic separation by changing the migration time through variation in EOF as well as by directly changing the mobilities of the pH sensitive ions.

It is clear from the above analysis that Joule heating as well as electrode reactions in micro channels can have a significant influence on the EOF as well as on the species separation efficiency by altering the temperature and the pH profile of the solution. A prediction of these effects in porous beds is difficult since they depend on different parameters such as the porous structure, the electrolyte concentration and the applied electric field. Therefore, in this work, we aim to perform experiments in a parameter range which ensures that our results are unaffected by Joule heating and pH changes.

1.4 Motivation for the thesis

The thesis is divided into two major objectives which are both related to electrokinetic phenomena but from a different perspective. Hence, we discuss both motivations separately as given below.

1.4.1 Streaming potential and streaming current

The motivation for the first paper comes from a review of streaming potential and streaming current literature where we realized the following:

- Almost all work on the electrokinetic characterization of solid substrates using streaming current and/or streaming potential measures the electrical features of the setup and/or electrolyte with an ex-situ experiment. That is, the conductivity of the electrolyte is measured in a separate measurement cell and at rest. Therefore, we perform in-situ electrical property measurements for different flow conditions in the current

research.

- The effect of surface conductivity on the overall conductivity under different flow conditions has been investigated earlier to some extent. However, these works utilize direct current (DC) or low frequency alternating current (AC) methods. Therefore for the first time, we apply high frequency AC conditions to characterize electrical properties of the medium and the solid substrate to exclude parasitic capacitive effects.

- Silver/silver chloride electrodes are generally considered as reversible. However, this statements stems from electrochemistry where the electrolytes are present in considerable concentrations. Contrary, the electrolytes are much diluted in electrokinetic measurements. We investigate whether the reversibility assumption still holds.

1.4.2   Electroosmosis in porous structures

The Motivation for the second paper, which is concerned with electroosmosis in porous structures, originates from:

- There is a lack of correlations for electroosmosis in porous substrates which correlates the flow to the liquid parameter and the characteristics of the packed beds. Such a correlation is required for the design of electroosmotic pumps which have various applications.

- The method of capillary interface tracking to measure electroosmosis has been used earlier. However, these works equalized the capillary flow and the electroosmotic flow rate. We utilize a centre-of-mass-model which incorporates physical effects such as hydrostatic pressure to obtain an improved influence on the nature of the packed bed flow. Moreover, this model also clearly shows when we have an influence of Joule heating which is another issue which is mainly neglected in literature.

1.5 Thesis Outline

The thesis consists of two major objectives both related to the electrokinetic phenomena. The first part of the thesis, which is concerned with the streaming current/potential phenomena, has already been submitted for publication while the second part, concerned with electroosmosis, is in draft format state for submission. Hence, the thesis is organized as followed:

After a brief and general introduction into electrokinetics, we present the respective work on streaming current and potential. This part is structured in a specific introduction, theory, experimental methods and materials, results and a conclusions section. Then, we present the work on electroosmosis in packed beds which comprises a specific introduction, theory, experimental methodology, results and conclusions. We conclude this with the some final remarks and some recommendations for future work.

Chapter 2

Streaming potential revisited: The influence of convection on the surface conductivity

2.1 Abstract

Electrokinetic phenomena play an important role in the electrical characterization of surfaces. In terms of planar or porous substrates, streaming potential and/or streaming current measurements can be used to determine the zeta potential of the substrates in contact with aqueous electrolytes. In this work, we perform electrical impedance spectroscopy measurements to infer the electrical resistance in a microchannel with the same conditions as for a streaming potential experiment. Novel correlations are derived to relate the streaming current and streaming potential to the Reynolds number of the channel flow. Our results not only quantify the influence of surface conductivity, and here especially the contribution of the stagnant layer, but also reveal that channel resistance and therefore zeta potential are influenced by the flow in the case of low ionic strengths. We conclude that convection can have a significant impact on the electrical double layer configuration which is reflected by changes in the surface conductivity.

2.2 Introduction

The formation of an electrical double layer (EDL) occurs when a surface, featuring electrical charges which are characterized by the so-called zeta potential (ZP), is in contact with a liquid which contains mobile charges. The surface charges attract counter-ions in the liquid which constitutes an interfacial layer with an electrical net charge; contrary to the liquid bulk which remains electrically neutral. Electrokinetic phenomena arise due to interaction of an EDL and an external force field such as pressure or electrical potential gradient.

Comprehensive review is available, e.g. in [26, 30].

There has been a renaissance of electrokinetics research which is mainly based on two motivations. On the one hand, novel phenomena such as alternating current (AC)-electroosmosis [31] have been discovered after a century of research in the field. On the other hand, various microfluidic concepts utilize electrokinetic phenomena, c.f. [32]. Additionally, the conversion of mechanical into electrical energy in nanofluidic channels has recently attracted increased interest [33, 34]. More traditionally, electrokinetic phenomena play an important role in the electrical characterization of surfaces; the motivation ranges from geophysical research over material to colloid and interface science. The electrokinetic phenomenon streaming potential (SP) results from a liquid flow along a stationary surface featuring an EDL. The convection of the EDL induces a streaming current (SC) which, vice versa, generates an electrical potential difference which can be conveniently measured, i.e. the SP.

The classical correlation which was developed to relate SP and SC to the ZP is the Helmholtz-Smoluchowski (HS) theory [35]. Nowadays, SP measurements are performed with various cell designs including microchannels formed by two parallel flat plates [14], microfluidic on-chip devices [36], asymmetric cells [15], cells coupled with fluorescence microscopy [37] or rotating disk electrodes [38]. Despite some progress/variations in cell designs, the vast majority of SP experiments utilize the classic HS correlation (cf. [37, 39–43]).

However, even the early work on SP noted that the classical HS theory has several shortcomings. Essentially, it does not account for the so-called surface conductivity, even though Smoluchowski himself pointed out that an excess of ions near a charged surface makes a definite contribution to the overall conductivity [44]. Hence, considerable errors can occur if the conductance (resistance) of the setup is calculated based on the bulk conductivity. The term bulk conductivity (resistivity) implies that the specific conductivity is not influenced by the boundaries of the measuring volume and, hence, it is measured ex-situ in large volumes such as beakers. In this article, we use the terms ex-situ and

16

in-situ for resistance measurements outside and inside of the SP cell, respectively. An early approach to include the effect of surface conductivity is the so-called Fairbrother-Mastin procedure [45]. Here, in-situ resistance measurements for liquids of low and high ionic strengths are employed with a modified HS equation to include the effect of surface conductivity. Generally, these in-situ resistance measurements are performed with direct current (DC) or very rarely with alternating current (AC) methods of very low frequencies. Additionally, the review of the literature reveals that the resistance is generally measured with resting liquids and not under experimental flow conditions (cf. e.g. [16, 39, 46, 47]). We discuss below that this can considerably alter the results. One exception is the work of Werner et al. who performed consecutive SP and SC measurements [48]. The ratio of SP and SC gives the in-situ cell resistance for experimental conditions but averaged over the investigated flow range.

There are several literature sources that claim that the HS correlation tends to give imprecise ZPs for other reasons than surface conductivity as summarized e.g. in [30]. This is in contrast to the work of Overbeek who, based on the Onsager relation, claimed that one electrokinetic experiment is sufficient to infer all other phenomena [49]. That is, the result of a SP experiment is equivalent to the result of an electroosmotic or SC experiment. This is practically not observed since each electrokinetic methods has its very own experimental difficulties and their influence on the results can be significant as shown for PMMA in our previous work [50]. Joule heating in electroosmotic experiments can considerably impact the electroosmotic mobility and thus falsifies the ZP inferred from it. SC measurements are challenging since the currents are on the order of nA and asymmetry potentials induce unwanted conduction currents. SP measurements at low ionic strengths and narrow gaps require electrical equipment with extremely high internal impedance to obtain reliable results [26].

There are also several works which, based on dimensional reasoning, assert that the SP gradient (and therefore the ZP) depends on the flow conditions as discussed in [47, 51, 52].

The same situation is claimed by Lu et al. based on a different motivation. In their work, a non-linear decay of the SP in the downstream direction of their measurement cell is found and explained with a convective influence on the EDL [53]. Such a behaviour would question the applicability of the HS correlation to obtain even approximate results, since respective flow parameters are not included and all ZPs which are commonly reported from SP experiments would be only apparent ZPs.

Motivated by these open questions, we perform SP and SC experiments in PMMA microchannels having different channel heights. For a better comparability of the different microchannel experiments, we derive novel correlations for the electrokinetic phenomena depending on the Reynolds number of the channel flow. In contrast to others, we measure the electrical characteristics of the aqueous electrolytes in-situ and under experimental conditions by employing electrical impedance spectroscopy (EIS). The application of this method allows for an evaluation of the influence of surface conductivity and that of the flow on the ZP. Additionally, we investigate the reversibility of the commonly used silver/silver chloride (Ag/AgCl) electrodes, especially for low ionic strength liquids.

The chapter is structured as follows: First, we review the theory of SC and SP and derive correlations which relate the phenomena to the Reynolds number. We also discuss some aspects of surface conductivity. Second, we describe the experimental methodology used in this work. Third, we present the experimental results of the electrical and electrokinetic experiments. Finally, the chapter is completed with some concluding remarks.

2.3   Theory

In this section, we briefly introduce the general theory of SC and SP. Figure 2.1 shows a sketch of the electrokinetic cell (EKC) used in this work which illustrates the underlying physicochemical phenomena. The EKC consists of two reservoirs (indexed 1,3) with incorporated electrodes which are connected by a microchannel (indexed 2). The microchannel
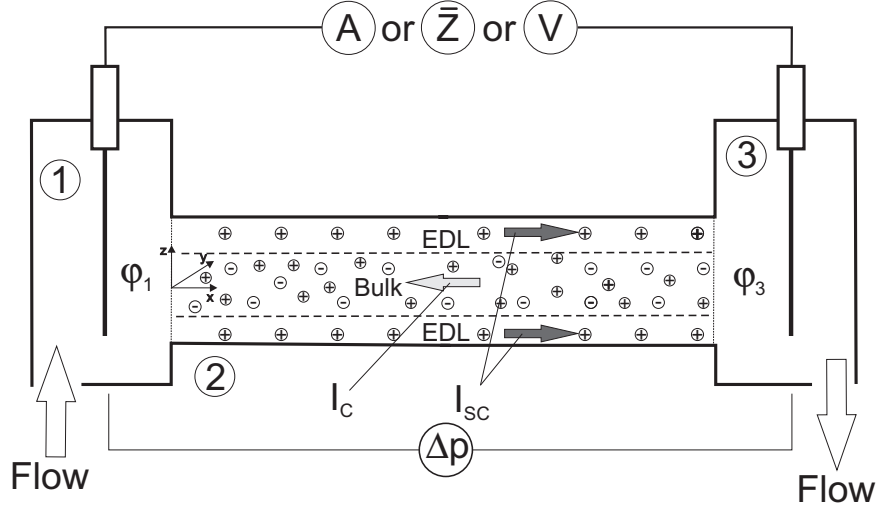
Figure 2.1: Schematic of the electrokinetic cell (EKC) used in this work to measure the electrokinetic phenomena of streaming potential and streaming current. The dimensions are not to scale.

is formed by two parallel plates, made from the substrate to be characterized. The microchannel consists of width w_2, length l_2 and height h_2; such that $l_2 > w_2 \gg h_2$. The EDL at the interface liquid/microchannel wall is characterized by the ZP ζ. A pressure difference Δp drives the liquid through the channel. This generates a convective charge transport in the EDL which is called SC I_{SC}. If we operate the EKC in a open circuit mode, a potential difference between the reservoirs is built up. This potential difference is called SP $\Delta\varphi_{SP} = \varphi_1 - \varphi_3$ which, in turn, induces the conduction current I_C between the electrodes. Whether we measure SC or SP depends on the electrical instrument connected to the EKC. This is indicated by the different symbols which connect the electrodes; i.e., amperemeter, and voltmeter and an "impedance meter" used for the electrical characterization.

For further description, we analyze the equivalent electrical circuits (EEC) for the different operation modes as given in fig. 2.2. The main motivation here is that the EEC of the SP/SC does not correspond to the one for the electrical characterization. Generally, the SC and SP circuits are similar and consist of an internal and external circuit. The internal circuit, indicated by the dotted-dashed line, comprises a current source symbolizing the SC.

19
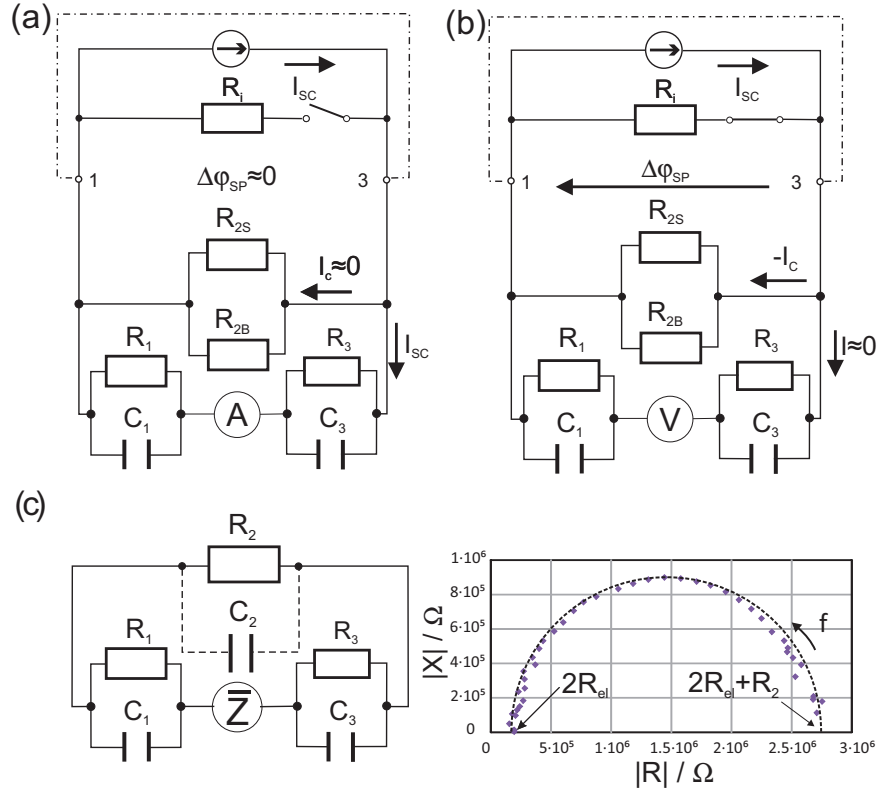
Figure 2.2: Equivalent electrical circuits for (a) SC measurements; (b) SP measurements; (c) EIS (left) with a typical Nyquist plot (right) measured in a microchannel of height $h_2 = 60\mu m$ and ionic strength $I = 0.5mM$

Additionally, there is an internal resistor R_i which is required to generate the SP. The outer circuit consists of the electrical elements symbolizing electrodes and microchannel. We computed that there is practically no influence of the liquid reservoirs on the electrical problem. A well-accepted model for electrodes is a RC element, where the electron transfer resistance is modelled with an ohmic resistor while the electrode's EDL is considered a capacitor, both arranged in parallel [54]. We make the reasonable assumption that $R_1 = R_3 = R_{el}$ and $C_1 = C_3 = C_{el}$. The ionic path in the microchannel is modelled with ohmic resistors. Here, we distinguish between the resistor of the bulk liquid R_{2B} and surface R_{2S}. If we measure the SC, an amperemeter is connected to the electrodes which has practically no internal resistance as depicted in fig. 2.2(a). Hence, the entire SC flows through the electrodes and

the conduction current is practically zero since the microchannel resistance is much higher than that of the amperemeter. For SP measurements, illustrated in part (b), we connect a voltmeter to the EKC. The voltmeter should have an internal resistance much higher than that of the channel. Then, the SC in conjunction with the internal resistor R_i induces the SP between the terminals (reservoirs) 1 and 3. Practically, no current flows through the electrodes and the voltmeter. The SP induces the conduction current which goes through the microchannel resistors R_{2B} and R_{2S}.

The situation changes when we perform an in-situ electrical characterization of the EKC using electrical impedance spectroscopy (EIS) as given in fig. 2.2(c) (left). Essentially, we apply an alternating excitation across the EKC and measure the alternating answer for different excitation frequencies. A typical result is given as well in fig. 2.2(c) (right). We discuss the method in more detail in section 2.4.3 and give here only a brief summary. For fairly conductive electrolytes, EIS allows for a separate determination of the total microchannel resistor $R_2 = 1/(1/R_{2B} + 1/R_{2S})$ and the electrode resistor R_{el}. However, for electrolytes with a very low ion content, there is the so-called bulk capacitance C_2 arranged in parallel to R_2 (dashed line) and only the total external resistance $R_2 + 2R_{el}$ can be measured.

To summarize the EEC analysis: The current paths in the EKC depend on the connected instrument. For SC measurements, the SC goes through the electrodes while for SP the conduction current goes through the microchannel but not through the electrodes. EIS only allows for the measurement of the total microchannel resistance but not for the single contributions of bulk and surface. For low ionic strengths, the electrode transfer resistance is included in the measured resistance.

We now derive the electrokinetic and hydrodynamic correlations in the EKC where we generally follow the standard assumptions as e.g. given in [13]. However, we deviate in some points: (i) We do not use the pressure difference since we perform experiments with

different channel heights. Hence, we relate the electrokinetic phenomena to the Reynolds number, which expresses hydrodynamics independent of the channel geometries. (ii) The hydrodynamic correlations are given independent of channel's cross section to ensure a general applicability for laminar flows in arbitrary geometries. (iii) The correlations (gradients) are given in a differential form and are not limited to a linear order. We also do not account for diffusive transport which has significant contributions in colloidal and membrane systems as described in e.g. [55, 56].

A differential SC in a microchannel of arbitrary cross section A_c, using a linearized velocity profile in the EDL, can be written as

$$dI_{SC} = -A_c \frac{\varepsilon \zeta}{\mu} d\left(\frac{dp}{dx}\right). \tag{2.1}$$

Here, ε is the liquid permittivity; μ is the dynamic viscosity; and $d(dp/dx)$ is a differential change of the pressure gradient in flow direction x. The differential pressure gradient can be expressed in terms of a differential volumetric flow rate according to $d(\frac{dp}{dx}) = R_\mu d\dot{V}$, where the viscous flow resistance R_μ depends on the cross section of the microchannel. Using the velocity amplitude u_0 of an equivalent plug flow, the hydraulic diameter $d_h = 4A_c/P_c$, where P_c is the wetted perimeter of the cross section, and the liquid density ρ, we can write the differential Reynolds number in a channel of arbitrary cross section as $dRe = 4\rho/(\mu R_\mu P_c) d(\frac{dp}{dx})$. After some rearrangements, we obtain

$$dI_{SC} = \frac{-A_c^2 R_\mu}{d_h} \frac{\varepsilon \zeta}{\rho} dRe \tag{2.2}$$

for the differential SC in a channel of arbitrary cross section depending on the differential Reynolds number. Equation (2.2) can be employed to obtain the ZP from measurements of I_{SC} vs. Re.

For a steady state and no current flowing through the electrodes (cf. fig. 2.2(b)), the

differential SC corresponds to the negative differential conduction current which can also be expressed using Ohm's law. That is,

$$dI_{SC} = -dI_C = d\left(\frac{d\varphi}{dR}\right) \approx d\left(\frac{\Delta\varphi_{SP}}{R_2}\right) \tag{2.3}$$

where the gradient of the electrical potential with respect to the ohmic resistance $d\varphi/dR$ can also be approximated with the ratio of SP and total microchannel resistance. After inserting eq. (2.2) in (2.3), integration over the channel length l_2 and further rearrangements, we obtain the general expression

$$\zeta = \frac{d_h}{A_c^2} \frac{\rho/\varepsilon}{R_\mu R_2} \frac{d\Delta\varphi_{SP}}{dRe} \tag{2.4}$$

which relates the ZP to the gradient of the SP with respect to the Reynolds number. The presence of the viscous resistance R_μ indicates that this electrokinetic phenomenon originates from the viscous drag of the electrical charge in the EDL. To obtain a correlation for a specific channel, the geometric parameters have to be customized. In this work, we use a microchannel of rectangular cross section of area $A_c = w_2 h_2$. The correlation between volumetric flow rate and pressure gradient is an infinite analytical series solution where the flow resistance can be approximated as $R_\mu \approx \frac{12\mu}{h_2^3 w_2}$ [57]. Inserting the geometric parameters in eq. (2.4), we obtain

$$\zeta = \frac{h_2^2}{6(h_2 + w_2)} \frac{\rho}{\varepsilon\mu} \frac{1}{R_2} \frac{d\Delta\varphi_{SP}}{dRe}. \tag{2.5}$$

Note that the correlation depends on the channel resistance R_2 that we measure in-situ under the same conditions as for the SP experiments.

The classical HS theory considers only the bulk liquid resistance in the microchannel $R_{2B} = \frac{l_2}{w_2 h_2} \frac{1}{\sigma_B}$. Hence, the HS equivalent of eq. (2.5) is

$$\zeta = \frac{h_2^3 w_2}{6 l_2 (h_2 + w_2)} \frac{\rho\sigma_B}{\varepsilon\mu} \frac{d\Delta\varphi_{SP}}{dRe}. \tag{2.6}$$

The modification of the classical HS correlation incorporates the surface conductivity (surface resistance R_{2S}) arising from the EDL at the interfaces. The ions in the EDL have a different concentration than those of the bulk; the mobility may differ as well. This phenomenon is quantified in terms of the surface conductivity σ_S which is the surface equivalent to the bulk conductivity σ_B. Whatever the ion distribution in the EDL, σ_S can always be defined through the 2D analog of Ohm's law; i.e. $j_S = -\sigma_S \frac{d\varphi}{dx}$ where j_S is the surface current density in A/m [26]. The influence of the surface conduction is usually expressed by the dimensionless Dukhin number $Du = \sigma_S/(\sigma_B h_2)$. We realize that the surface conductivity is scaled with the channel height, i.e., it becomes prominent for very narrow channels as well as for low ionic strengths. Finally, considering the relations above, we use the ohmic resistance $R_2 \equiv \frac{1}{1/R_{2B}+1/R_{2S}}$ and obtain the equivalent modified HS eq. which accounts for the surface conductance of the upper and lower channel wall according to

$$\zeta = \frac{h_2^3 w_2}{6 l_2 (h_2 + w_2)} \frac{\rho \sigma_B}{\varepsilon \mu} (1 + 2Du) \frac{d\Delta\varphi_{SP}}{dRe}. \tag{2.7}$$

The present perception is that the surface conductivity can have contributions owing to the diffusive layer (DL) charge, adjacent to the plane of shear, and to the stagnant layer (SL) charge; it is $\sigma_S = \sigma_{DL} + \sigma_{SL}$ (cf. e.g. [58]). The DL contribution was first derived for symmetric electrolytes by Bikerman in 1933 (as cited in [5]) as

$$\sigma_{DL} = \sqrt{8\varepsilon R_g \bar{T} I} \left(\frac{\nu_+}{A(\zeta) - 1} - \frac{\nu_-}{A(\zeta) + 1} + \frac{4\varepsilon R_g \bar{T}}{\bar{z} F \mu} \frac{1}{A(\zeta)^2 - 1} \right) \tag{2.8}$$

where R_g is the universal Gas constant; ν_+ and ν_- are the absolute values of the ion mobility of cation and anion, respectively; and I and $\bar{T}$ are the ionic strength and the absolute temperature of the symmetric electrolyte. The function $A(\zeta) = \coth\left(\frac{\bar{z} F \zeta}{4 R_g \bar{T}}\right)$ derives from the analytical solution of the charge distribution at an infinite plate and contains the valency $\bar{z}$ and the Faraday constant F. This expression includes the contribution of migration and that of electroosmosis which results in an additional mobility of the charges. The

expression is valid for negative surface charges. In the case of positive ones, the cationic and anionic mobilities have to be exchanged. The stagnant layer conductivity σ_{SL} may include a contribution due to the specifically adsorbed charge and another one due to the part of the DL that may reside behind the plane of shear [26]. The charge on the solid surface is generally assumed to be immobile and, hence, does not contribute to σ_S [26]. Further comprehensive treatise of surface conductivity is available, e.g. in [58].

2.4 Experimental methods and materials

This section describes details of the experimental setup, materials and methods that we use in this work.

2.4.1 Experimental setup

The experimental setup consists of the electrokinetic cell (EKC) and several fluidic and electrical components (sketch of the setup is given in chapter 3). The EKC is connected to a polyethylene vessel containing the aqueous electrolyte. This vessel can be charged with a controlled pressure by a nitrogen gas cylinder (Ultra High Purity 99.999%, MEGS, Canada) to pump the aqueous solution through the EKC. The pressure drop across the EKC is measured by two pressure gauges. Two Ag/AgCl electrodes are inserted in the EKC for the measurement of electrical signals. Electrodes are made from silver wires (99.99% trace metals, Sigma-Aldrich, Canada) by anodic deposition of silver chloride in a $3.0M$ KCl solution (ACS reagent grade, Sigma-Aldrich, Canada) at a current density of $1mA/cm^2$ for 45 minutes. The electrodes are connected to a potentiostat (PGSTAT302N, Metrohm Autolab B.V., The Netherlands) which allows for the measurement of electrical signals; the input impedance of the instrument is $> 1T\Omega$.

The custom-build EKC is constructed from two Teflon® blocks containing fluidic and electrical connections, liquid reservoirs and allows for the incorporation of two test wafers

of dimensions $70mm \times 30mm \times 1.5mm$ to form the microchannel. We use test wafers made from PMMA sheets since a comprehensive data set which can be used for verification is available from our previous work [50]; however, any material can be tested as long as it features the specified dimensions. Gaskets are used inside the PTFE blocks to form a well-defined gap between the PMMA wafers. Microchannel geometries used in this work are of length $l_2 = 7cm$, width $w_2 = 2.5cm$ while heights ranging from $h_2 \simeq 5..300\mu m$ are achieved depending on the gaskets. Two types of gaskets are used: (i) rigid (spacer) gaskets made of PTFE sheets or Kapton® (Polyimide) which give microchannel heights of $h_2 \gtrsim 50\mu m$ and $h_2 \lesssim 50\mu m$, respectively; (ii) soft gaskets of latex rubber which are used for sealing purposes.

2.4.2 Streaming potential/current protocol

SP and SC measurements are carried out using the following procedure. First, PMMA wafers are cleaned using a cleaning procedure as described in [15]. PMMA wafers and gaskets are then installed in the EKC and the assembled device is connected to the setup. Four different microchannel heights ($h_2 = 6, 60, 175, 300\mu m$) are used in this work. Verification of the microchannel height is done each time the cell is assembled by using electrical and hydrodynamic resistance measurements. The observed accuracies are around 30% and 10% for $h_2 < 100\mu m$ and $h_2 > 100\mu m$, respectively. Electrolyte solutions are prepared using NaCl (ACS reagent, Sigma-Aldrich, CA) dissolved in a DI water matrix ($\sigma \lessapprox 1\mu S/cm$). The limit for the lowest ionic strength that we prepare is $I \approx 0.002mM$ where we consider the contribution of the carbonic acid equilibrium to the water matrix. There is no buffer reagents added to adjust the pH value since there is no influence of the pH value on the ZP of PMMA in an acidic and neutral regime (cf. [50]). Hence, the electrolytes' pH value is around 5.5 ± 1. Ex-situ conductivity and pH testings are performed using a modular pH and conductivity meter (Mettler-Toledo, SevenMulti, Switzerland). Subsequently, the electrolyte solution is filled in the vessel which is then pressurized by the nitrogen gas. Before

26

each experiment, the respective electrolyte is pumped through the EKC for 30 minutes at a pressure difference of $\Delta p = 25 kPa$. The actual experiment is undertaken by adjusting pressure differences in the range of $10kPa$ to $75kPa$; the measurement of the electrokinetic phenomenon is done for 60 seconds at a constant pressure. We use the corresponding time-averaged value for data evaluation. For each ionic strength, 5 pressure values are applied to obtain a correlation between SP or SC and Reynolds number of the flow. Note, that the available range of Reynolds numbers depends on the microchannel height. For the largest and smallest height, the investigated range is $Re \approx 0..4000$ and $Re \approx 0..0.04$, respectively. To minimize the asymmetry potential, the electrodes are short-circuited between two consecutive measurements. Furthermore, the electrodes are renewed between measurements of different ionic strengths or when the asymmetry potential becomes quite significant.

2.4.3   Electrical impedance spectroscopy

We measure the channel resistance in-situ under operation conditions by employing EIS. The impedance $\bar{Z} = R + jX$ is a measure of the ability of an electrical circuit to resist the passage of an alternating current. It consists of time-independent, linear elements expressed by an ohmic resistor (real part) R and the reactance (imaginary part) X which describes the time-dependent behaviour of non-linear elements such as capacitors or inductors. It can be determined by applying an alternating voltage $\bar{U}$ to the EKC and measuring the resulting alternating current $\bar{I}$. The impedance is defined likewise to Ohm's Law as $\bar{Z} = \bar{U}/\bar{I}$. If the EEC contains non-linear elements, the current and impedance feature a phase shift. For EIS, the impedance is scanned for a range of excitation frequencies which often allows for specification of the single EEC elements. The use of EIS, as opposed to DC measurements, has a number of advantages. AC signals at appropriate frequencies eliminate the parasitic influence of liquid viscous relaxation and other capacitive elements in the setup. A typical example is the electrode capacitance (cf. fig. 2.2), but also those of plugs and cables which can considerably influence the results if DC or AC voltages of low frequencies are used.

Additionally, DC or low frequency measurements may induce electrochemical reactions at the electrodes which considerably alter pH and ionic strength of the liquid; information on EIS can be found in e.g. [59]. For further evaluation, the charge relaxation time $t_r = \varepsilon/\sigma$, i.e., the ratio of the liquid permittivity and conductivity, can be used. The relaxation time is the time scale at which free charges relax from the liquid bulk to the outer boundaries [60]; it is a measure of how long it takes for a perturbated electrical system to become polarized by conduction processes. We estimate that we require frequencies higher than $f \gg 1/t_r \simeq 100 kHz$ to exclude polarization effects in case of very low ionic strengths.

Essentially, we measure impedances in the EKC for resting liquids and various flows in a frequency range of $f \sim 0..10^6 Hz$. The impedance data are interpreted based on the EEC in conjunction with Nyquist plots as given in fig. 2.2(c). A Nyquist plot contains impedance data for the measured frequency range; the imaginary and real parts are plotted on the y-axis and x-axis, respectively. The Nyquist plots measured in this work are full or partial semicircles depending on the scanned frequency range; this is in accordance to the theory as given by the EEC. A full semicircle crosses the x-axis at $f = 0$ and at $f \to \infty$.

In the case of high ionic strengths, scans are performed over the entire frequency range. In this case, there is no significant influence of the bulk capacitance C_2 and the electrode capacitors C_{el} are short-circuited at high excitation frequencies. Hence, the x-intercept at $f \to \infty$ corresponds to the total ohmic resistance of the microchannel R_2. The interpretation is more demanding for very low ionic strength liquids. For this case, the aqueous electrolyte is more or less pure water and behaves more like a dielectric than a conductive liquid. An alternating electrical field re-orientates the polar water molecules resulting in a displacement current. Hence, a fraction of the high-frequency alternating current goes through C_2 and bypasses R_2. The x-intercept value at $f \to \infty$ does not correspond to R_2 anymore. The interpretation of the EEC gives that the x-intercept value at $f = 0$ corresponds to the total ohmic resistance $R_2 + 2R_{el}$ of the external circuit. Though, this value

cannot be directly measured since the already discussed parasitic capacitive effects occur at low frequencies gives very scattered data. In this case, we measure only in a medium to high frequency range and fit the EIS data to a semicircle correlation. The fit is used to infer $R_2 + 2R_{el}$ from the x-intercept at $f = 0$. Consequently, further experiments are required to obtain R_{el} which then allows for the identification of R_2.

Hence, we use a modified setup where the EKC is replaced by narrow glass capillaries of different lengths $l = 3, 6.8, 9.4cm$. The capillaries are connected to the setup by T-junctions with Ag/AgCl electrodes incorporated. Defined electrolyte solutions are pumped through the capillaries and the respective impedances are measured. The plot of impedance, at constant Reynolds number and ionic strength, vs. the capillary length reveals a linear correlation. We extrapolate the capillary length to $l = 0$ to find the impedance of the two T-junctions. The ohmic resistance of the electrolyte solution in the T-junction can be neglected to good approximation. Hence, the resistance at $l = 0$ corresponds to that of both electrodes for the given ionic strength.

2.5 Experimental results and discussion

The experimental results are given in two subsections, namely EIS and electrokinetic experiments. All results are given in the form of mean values and their standard deviations, based on at least three replicates or on standard errors.

2.5.1 Electrical impedance spectroscopy experiments

The first set of experiments is performed to determine the ohmic resistor R_{el} depending on the ionic strength of the aqueous NaCl electrolyte. The results are given in table 2.1 as electron transfer resistance $R_T = R_{el}A_{el}$ where A_{el} is the wetted electrode area. The data shows that the lower the ionic strength, the higher the electrode transfer resistance. A

Ionic strength I/mM	Electron transfer resistance $R_T/(\Omega\,m^2)$	Exchange current density $j_0/(A/cm^2)$
0.002	129.686 ± 14.557	$1.947 \cdot 10^{-8} \pm 11\%$
0.01	12.554 ± 1.982	$2.011 \cdot 10^{-7} \pm 16\%$
0.1	1.804 ± 0.302	$1.400 \cdot 10^{-6} \pm 17\%$
1	0.060 ± 0.014	$4.226 \cdot 10^{-4} \pm 23\%$
10	0.023 ± 0.003	$1.110 \cdot 10^{-4} \pm 13\%$
50	0.002 ± 0.0002	$1.656 \cdot 10^{-3} \pm 10\%$

Table 2.1: Electron transfer resistance and exchange current density of an $Ag/AgCl$ electrode in aqueous NaCl electrolytes measured by EIS.

regression yields the logarithmic correlation $\log\left(\frac{R_T}{\Omega m^2}\right) = -1.023\log\left(\frac{I}{mol/L}\right) - 4.001$. Table 2.1 also gives the corresponding exchange current densities – a measure for the electrode reversibility – which are calculated the standard way (cf. [54]). For example, a mercury-sulphate electrode features an exchange current density of $j_0^0 = 10^{-12}A/cm^2$ at standard state and is therefore highly polarizable [54]. In terms of a SC experiment, such an electrode cannot be employed since it does not take up the electrical charges which build up in the electrode EDL even at high overpotentials. In contrast, a Ag/AgCl electrode at standard state features $j_0^0 = 13.4A/cm^2$ and is therefore considered as fully reversible [54]. This means that the SC is entirely consumed by the electrodes at overpotentials which are practically zero and there is no unwanted potential difference which induces a conduction current. However, an electrokinetic experiment is generally conducted under conditions not comparable to the standard state and the data in table 2.1 indicate that a Ag/AgCl electrode at low ionic strengths is far away from being fully reversible. A fact that is mainly neglected in the respective literature. The question arises whether this induces a significant conduction current during SC measurements or not. To answer this question, we estimate the potential difference between the electrodes using the Butler-Volmer eq. in conjunction with the equilibrium current densities in table 2.1 and a charge transfer coefficient (symmetry factor) of $\beta = 0.3$. We estimate that the influence on the SC is on the order of or less than $\lesssim 1\%$. Hence, the influence of the non-ideal electrodes can be neglected with respect

to the higher standard deviations of our measurements. Though, we assume that the errors become significant for worn out electrodes and low chloride concentrations underlining the importance to renew the electrodes on a frequent basis.
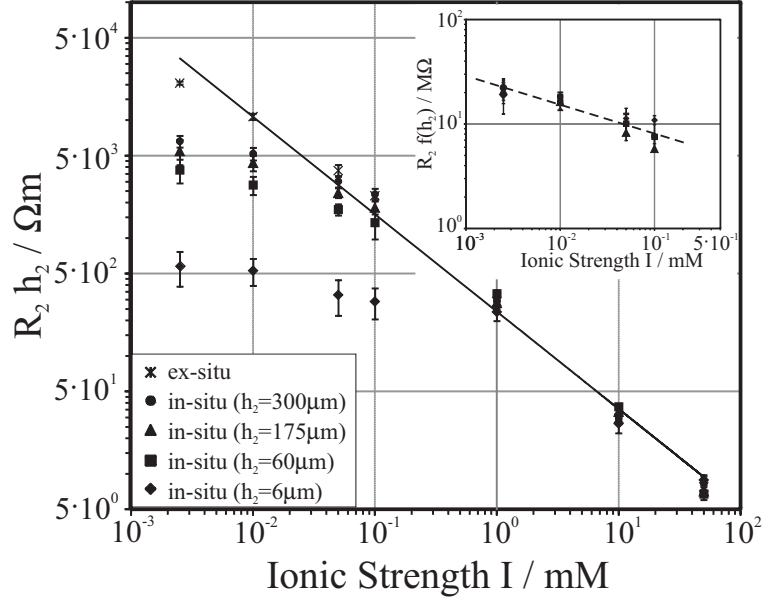
Figure 2.3: Microchannel resistance times the channel height vs. the ionic strength for stagnant liquids ($Re = 0$). The inset shows the collapse of the low ionic strength data if scaled appropriately.

In terms of SP measurements, we subtract the electrode resistances from the total resistance of the external circuit that we measure using in-situ EIS. Figure 2.3 shows the results of various microchannels for stagnant liquids ($Re = 0$). In detail, we plot the product of microchannel's resistance and height versus the ionic strength of the NaCl solution, both on a logarithmic scale. We also show the corresponding values inferred from ex-situ measurements; i.e., we use the bulk conductivities σ_B and compute the corresponding resistances based on the microchannel geometries. Then, the motivation for this representation becomes clear. The correlation between the product of ex-situ resistance and channel height and ionic strength is linear as indicated by the solid line. The situation is different for

the resistances which are measured in-situ. While we find a similar linear relationship for intermediate to high ionic strengths, we find generally lower values for all investigated microchannels at low ionic strengths of $I \lesssim 0.1mM$. Generally, the lower the ionic strength and the smaller the channel height, the higher is the deviation from the ex-situ results. Figure 2.3 also contains an inset which demonstrates that the $I \lesssim 0.1mM$ data collapses onto a single curve, to a good approximation, if the resistances are multiplied with an adequate scale $f(h_2)$. Hence, a regression can be performed using two correlations which depend on the range of the ionic strength; we obtain

$$\frac{R_{2,0}(h_2, I)}{M\Omega} \approx \begin{cases} \frac{l_2}{w_2 h_2} \frac{l}{\sigma_B} & \text{for} \quad I \gtrsim 1mM \\ \frac{\left(\frac{I}{mol/L}\right)^{-0.272}}{0.0041\frac{h_2}{\mu m}+0.2865} & \text{for} \quad I \lesssim 0.1mM. \end{cases} \tag{2.9}$$

Further EIS experiments are performed for various Reynolds number flows. For some conditions (discussed below), we observe that the resistance changes linearly with the Reynolds numbers, to a good approximation. Detailed results are given in figure 2.4(a) in the form of relative resistance change per Reynolds number $\Delta R_2/Re$ vs. ionic strength. Here, relative means that the absolute changes per Reynolds number are scaled with the respective resistance for stagnant liquids $R_{2,0}$. The connections between the data points are for the sake of a better illustration. A twofold behaviour of $\Delta R_2/Re$ in terms of the ionic strength can be found. Generally, $\Delta R_2/Re$ at a given channel height remains more or less constant for $I \lesssim 0.1mM$. For $I \gtrsim 0.1mM$, we observe a decrease of $\Delta R_2/Re$ with an increasing ionic strength. We also notice that the smaller the channel height the higher $\Delta R_2/Re$; the difference can be several orders of magnitudes. In this context, we should recall that there are considerably different Reynolds number regimes for the different channel heights. Essentially, the change of the microchannel resistance is rather insignificant
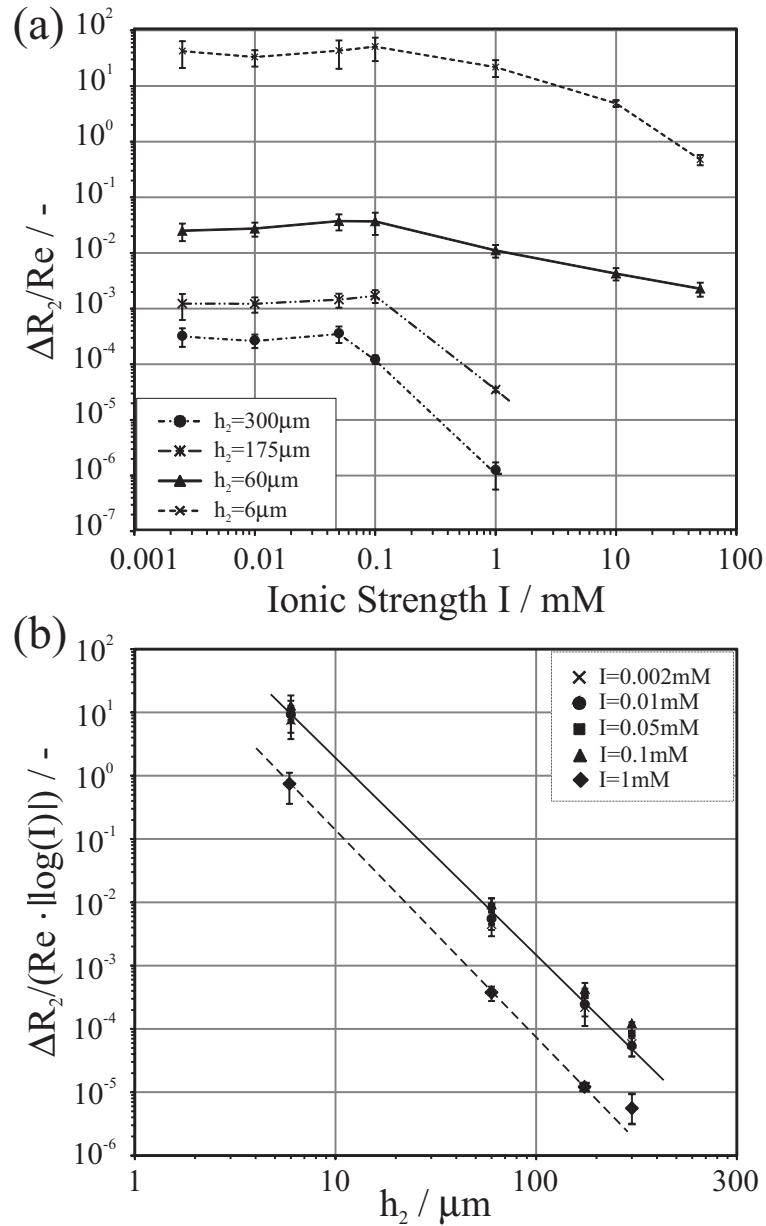
Figure 2.4: Relative change of the microchannel resistance per Reynolds number: (a) for different channel heights vs. the ionic strength; (b) scaled with the absolute logarithmic ionic strength vs. the channel height.

for large channels and high ionic strengths. A specific example, which demonstrates the absolute resistance for different Reynolds numbers, is discussed below. To find an empirical correlation for the relevant data, we scale $\Delta R_2/Re$ with the magnitude of the logarithmic

ionic strength and plot it vs. the channel height, both on a logarithmic scale. Figure 2.4(b) demonstrates that the data collapses onto two different curves, depending on the range of the ionic strength. The slope of the curves is almost identical; the difference is in the y-intercept Finally, we use the collapsed data to derive an empirical correlation for the microchannel resistance as a function of ionic strength, channel height and Reynolds number consisting of eq. (2.9) and the flow correction term

$$f_2(h, I, Re) = \begin{cases} 0 & \text{for} \quad I > 1mM \\ 10^{2.415} \left(\frac{h}{\mu m} \right)^{-3.28} \left| \log \left(\frac{I}{mol/L} \right) \right| Re & \text{for} \quad I \sim 1mM \\ 10^{3.39} \left(\frac{h}{\mu m} \right)^{-3.117} \left| \log \left(\frac{I}{mol/L} \right) \right| Re & \text{for} \quad I \lesssim 0.1mM \end{cases} \qquad (2.10)$$

according to

$$\frac{R_2(h, I, Re)}{M\Omega} \approx R_{2,0}(h, I) \left(1 + f_2(h, I, Re) \right). \qquad (2.11)$$

Note that eq. (2.11) is a reasonable quantitative correlation for most of the investigated range while it gives only qualitative results for the transition between low and high ionic strengths.

To summarize our findings from the EIS experiments: For intermediate to high ionic strengths, there is no significant difference between in-situ and ex-situ measured microchannel resistances. For low ionic strengths, in-situ measurements reveal even for larger channels significantly lower values as well as a dependency on the channel flow.

We employ eq. (2.11) to obtain a deeper insight into the EIS results. First, we investigate the limiting case of a microchannel of vanishing height, i.e. $h_2 \to 0$. For $I \gtrsim 1mM$ the channel resistance approaches infinity. For $I \lesssim 1mM$ a finite value is observed which depends on the ionic strength and the Reynolds number. Recall that for decreasing microchannel height, the influence of the surface conductivity increases whereas the influence

of the bulk liquid decreases. Consequently, the surface conductivity can be derived from the inverse resistance at $h_2 \to 0$. Figure 2.5(a) gives the so inferred surface conductivity
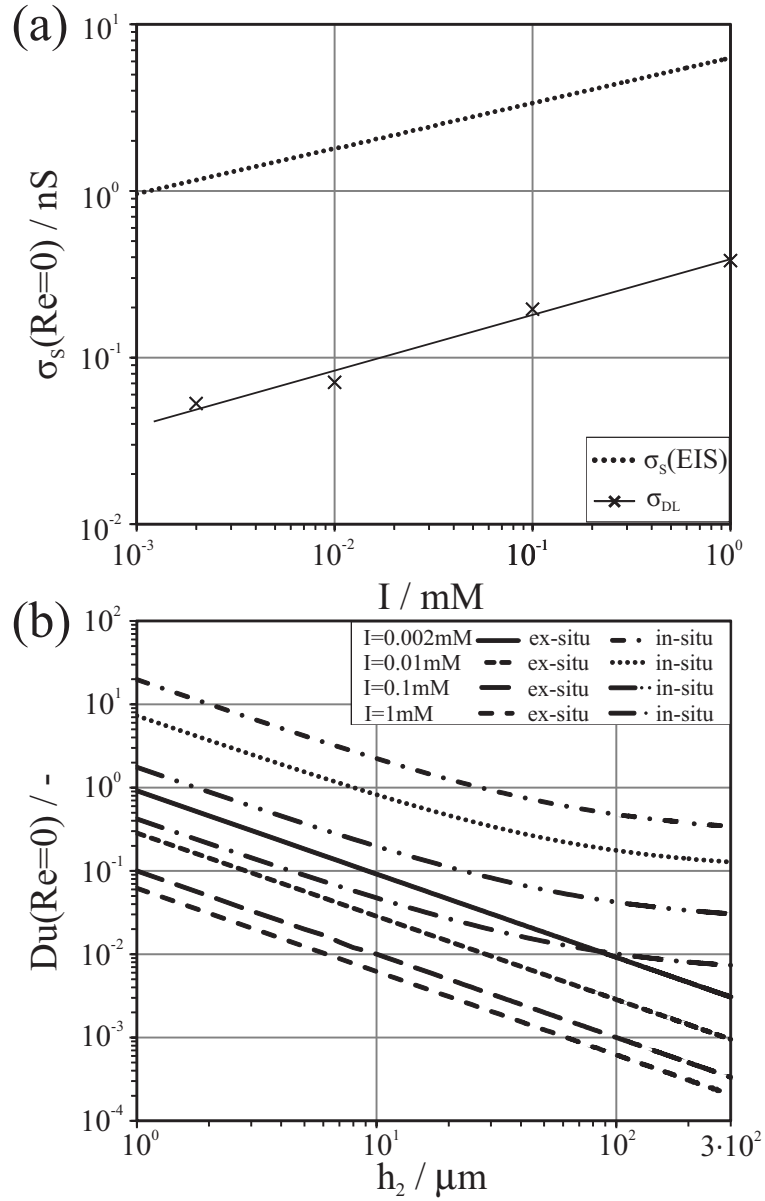
Figure 2.5: (a) Surface conductivity versus the ionic strength of the aqueous electrolyte; (b) Dukhin numbers from in-situ and ex-situ measurements vs. the microchannel height for stagnant liquids ($Re = 0$).

σ_S of the PMMA surface (dotted line) versus the ionic strength and for a stagnant liquid,

both plotted on a logarithmic scale. For the sake of comparison, the Bikerman surface conductivity σ_{DL} is given as well. In detail, we compute σ_{DL} based on eq. (2.8) using ZPs from four SC experiments as described below. Generally, we find that both surface conductivities linearly increase with an increasing ionic strength, even the slopes are fairly similar. The main difference is on the magnitude. While the measured surface conductivity is on the order of nano-Siemens, the Bikerman surface conductivity which accounts only for the diffusive layer is about one order of magnitude less. This would mean that the surface conductivity is mainly determined by the stagnant layer while the double layer contribution is almost negligible. This observation is consistent with the work of Werner et al. [48] and Leroy and Revil [61] who measured the surface conductivity of fluor-polymers and clay minerals, respectively. Both studies found high surface conductivities in the nano-Siemens regime and attributed the main contribution to the stagnant (inner Helmholtz plane) Stern Layer. Nevertheless, the question arises whether there are further phenomena contributing to the surface conductivity which are yet to be identified.

We use the surface conductivities to calculate Dukhin numbers as defined in section 2.3. Figure 2.5(b) shows the Dukhin numbers based on in-situ and ex-situ (i.e., bulk conductivity in conjunction with eq. (2.8)) measurements vs. the channel height and for various ionic strengths. Generally, the Dukhin number increases with decreasing channel heights and decreasing ionic strengths. In terms of the ex-situ data, a significant surface conductivity influence is only predicted for channel heights of $h_2 \lesssim 100\mu m$. In contrast, the in-situ data reveals that even for the largest channel height, Dukhin numbers of $Du \sim 0.1$ for the low ionic strengths are found. For the smallest channels and lowest ionic strengths, even Dukhin numbers of $Du \gtrsim 10$ occur.

To summarize, the influence of the surface conductivity can only be neglected for relatively large channels of height $h_2 \gtrsim 100\mu m$ along with ionic strengths of $I \gtrsim 1mM$.
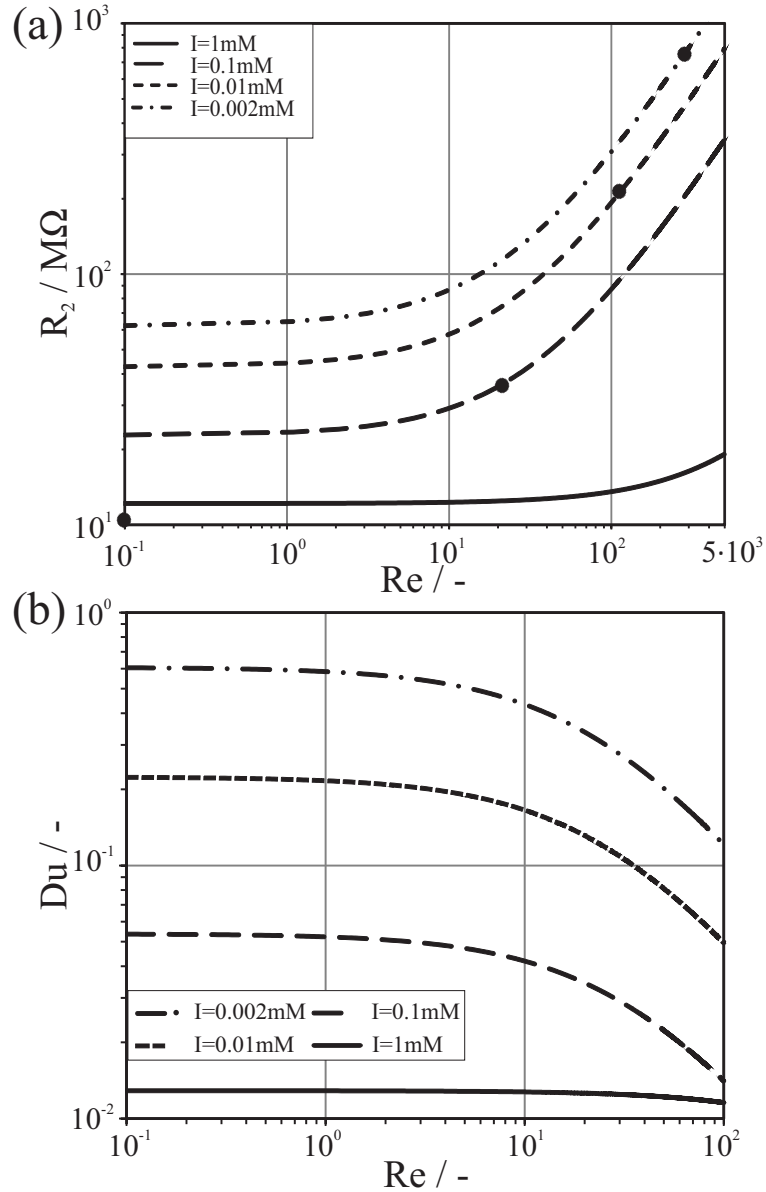
Figure 2.6: (a) Microchannel resistance and (b) Dukhin number vs. the Reynolds number in a microchannel of height $h_2 = 60\mu m$ for aqueous electrolytes of various ionic strengths.

We now demonstrate the influence of the channel flow as predicted by eq. (2.11). Figure 2.6(a) plots the resistance R_2 of a microchannel with height $h_2 = 60\mu m$ for various ionic strengths and depending on the Reynolds number, both on a logarithmic scale. The solid

circles indicate the respective ex-situ resistances which are independent of the flow. We find that for low Reynolds numbers of $Re \approx 0..10$, all channel resistances remain rather constant. However, for higher Reynolds numbers, a considerable increase is observed. The onset of the increase depends on the ionic strength. We observe that the lower the ionic strength, the higher the Reynolds number which is required to observe in-situ measured resistances equal to the ex-situ measured ones. This statement does not hold for the $I = 1mM$ data where the ex-situ value is lower than the in-situ value at $Re = 0$. This is due to the limited accuracy from the regression of an ensemble of collapsed data. It should also be noted that the achievable Reynolds number range for the given channel height, is $Re \approx 0..50$; i.e., higher values are extrapolated.

The influence of the Reynolds number on the Dukhin number is reported in fig. 2.6(b). At the given channel height, a negligible influence of the surface conductivity ($Du \simeq 0.01$) is only observed for $I = 1mM$. For lower ionic strengths, the influence of surface conductivity is mainly significant ($Du \simeq 0.1$). Generally, an increase in Reynolds number decreases the influence of the surface conductivity.

To summarize, the total channel resistance and (the influence of) the surface conductivity strongly depends on the flow through the channel. The smaller the channel height and the lower the ionic strength, the higher the influence.

2.5.2   Electrokinetic experiments

In this section, we discuss the ZPs resulting from various SC and SP measurements using resistances from in-situ and ex-situ measurements.

Streaming current

SCs are measured for varying microchannel heights and ionic strengths. We learned in the previous section that flows through channels of small heights have an impact on the channel resistance. This behaviour must be related to an interfacial phenomena as we

discuss in more detail below in the conclusion section. If the interfacial structure changes with the flow, this must consequently be reflected in a dependency of the ZP on the flow as well. Hence, we plot the SC vs. the Reynolds number (not shown) and perform two types of data regressions, a linear and a quadratic one. The linear regression results in a constant slope and therefore, in conjunction with eq. (2.2), in a ZP which is independent of the Reynolds number. The quadratic regression results in a linear dependency of ZP and Reynolds number. Note, that both regression types generally result in comparable and high coefficients of determination.

Figure 2.7(a) gives the ZP vs. the ionic strength of the aqueous electrolytes, exemplarily for a channel with $h_2 = 60\mu m$. The standard deviation is only given for the linear regression data. Generally, we find that the magnitude of the ZP decreases linearly with increasing ionic strength. Linear correlations between ZPs and the logarithmic ionic strength are observed by multiple researchers, even for high ZP magnitudes and for systems with relatively complex surface chemistries, as summarized in [30, 62]. PMMA in an acidic and neutral milieu features no relevant surface chemistry [50]. Hence, we assume that the nature of the linear correlation between ionic strength and ZP is mainly based on the shielding of the surface charges. The lowest set of ZP magnitudes is observed when the SC data is processed by linear regression. The utilization of the quadratic correlation raises the question of which Reynolds number should be used for the calculation of the ZP. We choose $Re = 0$ and $Re = 20$, where the latter is roughly the median Reynolds number of the experiment. We observe the highest absolute set of ZPs for $Re = 0$. The magnitude decreases with increasing Reynolds number. If we consider the standard deviations of the experiments, there is only a distinct difference for ionic strengths of $I \lesssim 1mM$, likewise to findings of the EIS experiments.

Figure 2.7(b) shows the ZP vs. ionic strength inferred from SC measurements in microchannels of different heights. We employ the quadratic correlation to process the data and give the ZPs for the respective median Reynolds numbers of the experiments. The
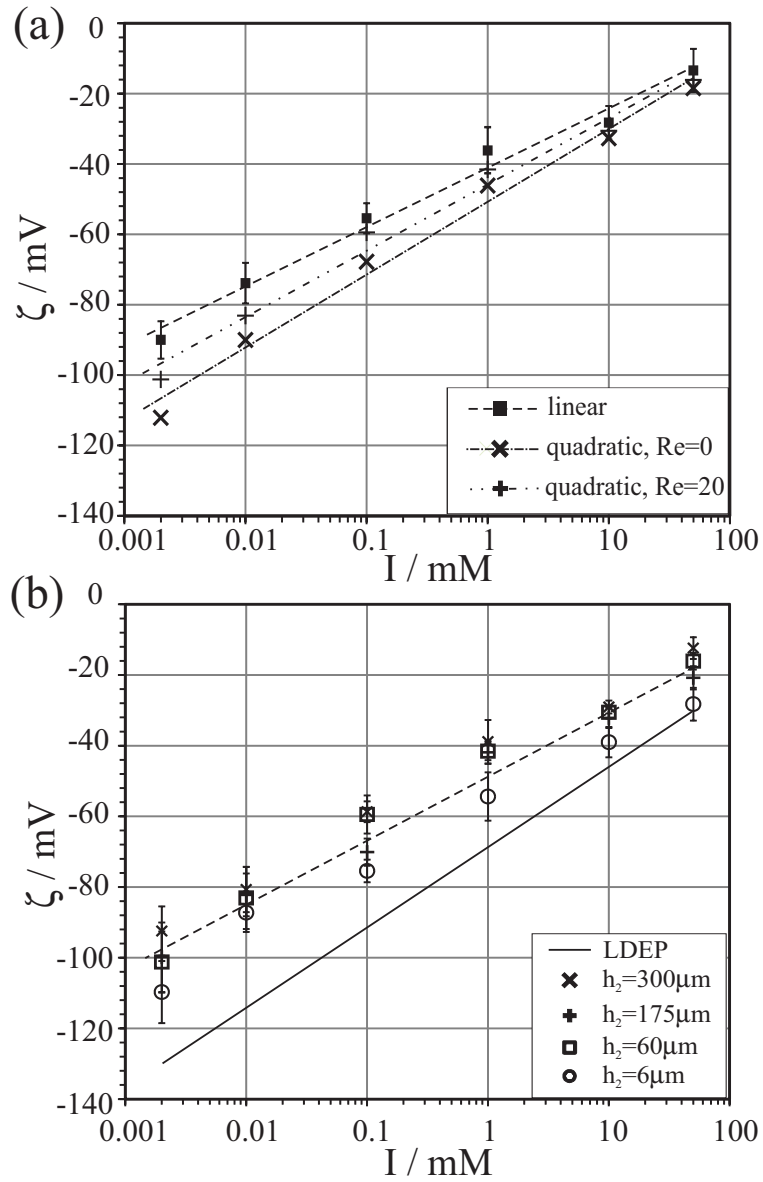
Figure 2.7: ZP vs. ionic strength for (a) measured in a microchannel with $h_2 = 60\mu m$ based on linear and quadratic data regression; and (b) for different microchannel heights and a median Reynolds number.

dashed line gives a regression of the ZPs averaged over all channel heights. Generally, the differences between the ZPs measured in different channels are more or less within the

standard deviation of the experiments. We also plot the ZP based on the empirical correlation $\zeta/mV = (28.21 - 2.7pH + 0.29pH^2)\log(I/(mol/L))$ received from Laser Doppler Electrophoresis (LDEP) experiments of PMMA particles as described in [50]. While the slope of the correlation is in good agreement with the present data, the absolute ZPs measured with LDEP are around 20 to 30% higher for low ionic strengths. Differences are smaller for higher ionic strength.

To summarize: We generally observe linear correlations between ZP and logarithmic ionic strength. Moderate differences in ZPs exist depending on whether a linear or a quadratic correlation between SC gradient and Reynolds number is used. We also observe that the ZP magnitude decreases with increasing Reynolds number.

Streaming potential

SP measurements are performed for varying microchannel heights and ionic strengths. In contrast to the SC experiments, we generally observe that a quadratic correlation reproduces the data with a better quality than a linear one. SPs are calculated based on eq. (2.5) and (2.6) to incorporate the findings from section 2.5.1.

Figure 2.8(a) shows the ZPs inferred from measurements in the microchannel with $h_2 = 60\mu m$. First, we apply the classical HS eq. (2.6) along with the bulk conductivity and a linear regression of the experimental data. The results are labelled as ex-situ and shown with the standard deviations of the experiment. Altogether, we do not observe a linear behaviour between ZP and logarithmic ionic strength. We distinguish between two ranges which are in accordance with those observed in the in-situ resistance measurements. For $I \gtrsim 1mM$ the absolute ZPs decrease with increasing ionic strength. In contrast, the absolute ZPs decrease with decreasing ionic strength in case of $I \lesssim 1mM$. This deviation for $I < 1mM$ has been observed by different researchers who employ HS correlation including refs. [63–65]. Nevertheless, the large majority of work in the literature does not
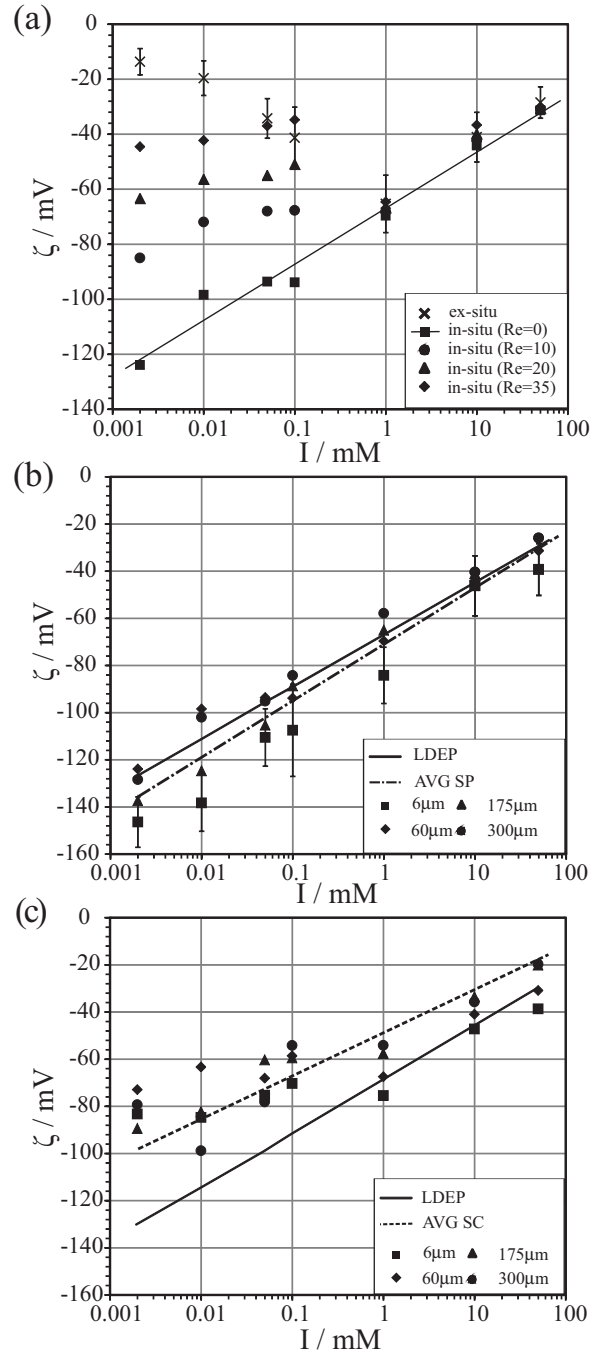
Figure 2.8: Zeta Potential vs. ionic strength: (a) measured in a microchannel with $h_2 = 60 \mu m$ and different Reynolds numbers; (b) for different microchannel heights and $Re = 0$; (c) for different microchannel heights and the median Reynolds numbers of the experiments.

show data for $I < 1mM$. Next, we discuss results based on eq. (2.5) using the channel resistances from the in-situ measurements. In this case, the ZP is two-fold influenced by the Reynolds number: (i) the channel resistance can depend on the flow (cf. eq. (2.11)) and (ii) the use of the quadratic regression results in $d\Delta\varphi_{SP}/dRe = f(Re)$. We compute the ZPs for different Reynolds numbers. Here, it is striking that we recover the linear correlation of ZP and logarithmic ionic strengths for $Re = 0$ as indicated by the respective regression (solid line). For increasing Reynolds numbers, there is no change for $I \gtrsim 1mM$ and the values are nearly identical to the ex-situ ones. For $I < 1mM$ we see that the absolute ZP decreases with increasing channel flow. That is, the higher the Reynolds number the closer the ZPs of in-situ experiments to those of the ex-situ experiments.

Figure 2.8(b) summarizes the results obtained from measurements in microchannels of different heights. All ZPs are computed using the results from the in-situ resistance measurements and for $Re = 0$. We give the standard deviation of the experiments with channel height $h_2 = 6\mu m$, the values of the other experiments are similar or less. Only minor differences are observed for ZPs based on measurements with channels of different heights. Furthermore, we observe a linear correlation between the ZP and the logarithm of the ionic strength in all cases. We also plot a regression of the average values over all channel heights (dot-dash line) and compare it with the LDEP data (solid line). Surprisingly, we find a very good agreement of averaged SP and LDEP data with only minor differences for low ionic strengths.

Finally, we would like to present in figure 2.8(c) the ZPs based on experiments with different channel heights and inferred using the median Reynolds number of the respective experiment. For $I \lesssim 0.1mM$ we find that the ZPs computed with the median Reynolds numbers are generally lower than those at $Re = 0$ (cf. fig. 2.8 (b)). Furthermore, the LDEP results and the averaged SC results are given as a solid and dashed line, respectively. We find an interesting aspect: For $I \gtrsim 1mM$ the SP results for median Reynolds numbers are in good agreement with the LDEP results. However, for $I \lesssim 0.1mM$ the SP results for

median Reynolds numbers rather correspond to the SC results.

2.6   Conclusions

We perform streaming current and potential measurements in PMMA microchannels of different heights and for aqueous electrolytes of various ionic strengths. Electrical impedance spectroscopy is applied to measure the resistance of the microchannel in-situ under experimental conditions. The EIS measurements show that in the case of liquids having low ionic strengths, there is a significant difference between the channel resistances obtained from in-situ and ex-situ measurements. The differences are significant even for relatively large channels and has not yet been reported in literature. In this case, the classical Helmholtz-Smoluchowski correlation fails. We assign the difference to the influence of surface conductivity. A comparison with the Bikerman diffusive layer contribution indicates that the majority of the surface conductivity must either arise from the stagnant part of the EDL or from phenomena which are not yet specified. We also study the effect of the flow field (Reynolds number) on the channel resistance. For low ionic strength liquids, the effect significantly increases with the reciprocal channel height. The scaling with the channel height once more indicates that this behavior is related to an interfacial and not to bulk phenomena. That is, our results indicate that convection influences the configuration of an EDL which is observed as a change of surface conductivity. A possible explanation is that the convection influences the structure of the stagnant layer. This assumption is supported by our observation that the influence of surface conductivity decreases for increasing Reynolds number. Whether the thickness of the stagnant layer, its charge content, or changes in the mobility are responsible for the observed phenomenon remains an open question and must be answered in future work. Consequently, if the EDL is influenced by convection, then there must be a flow dependency of the ZP as well. In terms of SC experiments, we find a moderate influence on the ZPs which is somewhat more pronounced at low ionic

strength. Essentially, the higher the Reynolds number, the smaller the magnitude of the ZP indicating that the change of the EDL structure leads to higher shielding of the surface charge. The influence of the Reynolds number on the ZPs inferred from the SP experiments is considerably higher compared to the SC experiments. This is understood since for SP experiments the convection does not only influence the induced SC (the EDL) but also the conduction current (via the channel resistance). We find that for high ionic strength, i.e., for no or only little influence of surface conductivity, the results of our SC, SP, and LDEP measurements are in a good agreement. For low ionic strength, the ZPs derived from SC and SP experiments, corrected for surface conductivity and flow, show a reasonable agreement to each other but not to the LDEP results. A possible explanation is that the LDEP measurements are buffered and the ZPs at low ionic strength are extrapolated. Finally, this work provides new insights on EDL phenomena and the applicability of the Helmholtz Smoluchowski theory. The influence of convection, which is not covered in the classical theories, is another reason why the Onsager relation between electrokinetic phenomena is usually not observed in experiments.

Chapter 3

Electroosmotic flow through packed beds of particulate materials

3.1 Abstract

Electrical charges originate at many solid surfaces in contact with liquids which together form the Electrical Double Layer (EDL). When we apply an external electric field tangential to the EDL, an electroosmotic flow (EOF) is induced. This phenomenon can be employed in microfluidic systems. Highly porous materials are especially suitable since they generate significant flow rates and pressures. Most of the models used to analyze electroosmotic flow through porous media are based on the so-called parallel capillary flow model. In terms of porous packed beds, these models have the disadvantages of oversimplifying the geometry to tortuous capillaries while neglecting intra-pore connections, varying pore geometries and the influence of the packed bed walls. In the current research, we employ dimensional reasoning (Buckingham Π theorem) to derive semi-empirical correlations which relate the electroosmotic flow to the characteristics of the packed bed material as well as electrical and liquid parameters. Experiments are carried out using a relatively simple and cost-effective set-up including different sets of sintered packed beds of borosilicate microspheres and various experimental conditions.

3.2 Introduction

Electrokinetic phenomena arise from the interaction of an external force with an electrical double layer (EDL), which is formed when an electrically-charged surface is in contact with a liquid containing mobile charges such as ions. The ions of opposite charge to that of the surface (counter-ions) are attracted towards the surface, while ions of equal charge (co-ions)

are repelled. The EDL is defined as the region in which, due to the excess of counter-ions over co-ions, the electrical neutrality of the liquid is violated. Different electrokinetic phenomena can arise depending on the interaction of the external force and the EDL. When we apply a tangential external electric field to the EDL, the counter-ions migrate and drag the surrounding solvent molecules by viscous interactions. This establishes a flow which is termed electroosmosis, electrokinetic flow or electroosmotic flow (EOF). Comprehensive review on EDL and electrokinetic phenomena is available in literature, e.g. in refs. [13, 26].

Typically, electroosmotic (net) flow is only observed in pores/channels having openings of less than around $1mm$ since the flow generating force occurs in the nano-scopic EDL and the much larger volume of the bulk liquid is only dragged. In other words, EOF is a micro-scale phenomenon and only observed when the surface-to-liquid volume ratio is sufficiently large. Consequently, we can expect that EOF is especially prominent if it takes place in porous substrates and indeed electroosmosis was initially observed in porous clay structures by Reuss [66] more than 200 years ago.

In the recent years, research on EOF has experienced a renaissance since it can be employed in microfluidic systems. Typical applications include the (single channel) transport of samples for analytical purposes [67–69], flow focussing [70] or to generate secondary flow patterns to improve mixing [71–74]. Microfluidic pumps, which are based on EOF, offer several advantages such as the absence of mechanical parts, pulse-free flows and the flow rate and direction are conveniently controlled by the electrical field. Additionally, these electroosmotic pumps (EOP) can be fabricated using standard microfabrication technologies and, thus, they can be readily incorporated on micro devices. In this regard, chip-integrated micro pumps can simply consist of single [75] or arrays of open channels [76–78]. However, the more favourable design incorporates porous structures because of the larger surface-to-volume ratio, which is especially beneficial since relatively high flow rates along with high pump pressures can be generated. Such incorporated (on-chip) porous structures usually contain packed beds of micron-sized spherical particles [79, 80]. Review on EOPs for

microfluidic applications is available from ref. [81].

The application of EOF is also beneficial for several chromatography techniques where pressure losses in the separation columns can be up to $600bar$, which has demanding requirements for the design and materials of mechanical pumps. There are some fundamental differences though, depending on the type of chromatography technique. In terms of capillary electrochromatography, the EOP also acts as a separation column; review on capillary electrochromatography is available in refs. [82, 83]. For high-speed liquid chromatography, the flow through the separation column is generated with an external EOP. Hence, a multitude of different external EOP concepts can be found in the literature. Generally, the active materials of external EOPs can be classified into two different structures. On one hand, the EOP is designed as a (consolidated) packed bed which has been realized using silica particles [84–88] or sintered borosilicate particles [62, 89, 90]. Additionally, there are further fabrication methods which produce packed bed like structures including monoliths made from silica [91] and from monomers [92, 93], as well as membranes from mixed cellulose ester and nylon [94]. On the other hand, there are pumping substrates which can be considered as a large array of more or less identical capillary pores. These structures have been realized by membranes made from anodic aluminum oxide [95, 96], glass [97] and from (track-etch) polymeric materials such as polycarbonate and polyethylene terephtalate [98]. Both structure types, the capillary and the packed bed type, create large surface to volume ratios. However, there are some fundamental differences. According to Niven [99], packed beds feature a much more complex network of interconnected pore conduits, consisting of both tetrahedral and octahedral pockets between solid particles, joined by narrower pore necks. The pore conduits themselves are of a complex cross-sectional form, including three-pointed stars, four-pointed stars and a variety of shapes in between [99].

In order to describe the nature of flows through porous structures, two main approaches are widely used (cf. e.g. Dullien [100]). On one hand, it is possible to engage a deterministic approach to model the flow on a microscopic level based on the governing equations of mass

and momentum continuity. Deterministic models give a detailed insight within the flow but their application still suffers from some considerable disadvantages. The detailed geometry of the porous substrate is usually not known and the costly numerical simulation is limited to rather small domains. Hence, we do not consider deterministic approaches in this work since they cannot easily be used for design purposes.

On the other hand, phenomenological models based on averaged (macroscopic) parameters are a useful semi-empirical approach to obtain design guidelines for technical systems. This approach does not intend to resolve the flow field in detail but to correlate macroscopic parameter such as flow rate and pressure drop to the properties of the porous substrate. Some experiments are required but the resulting correlations are usually simple mathematical expressions; well known examples are Darcy's Law, (Carman) Blake-Kozeny and the Ergun equation (cf. eg. [101]). The phenomenological models for EOF in porous structures that can be found in literature correspond to a capillary-type structure. Mazur and Overbeek modelled a porous diaphragm as an idealized arrangement of a large number of parallel and identical capillary pores [102]. The same idealization has been adapted by Vallano and Remco to packed beds of macro-porous particles [103] and by Yao and Santiago to porous glass frits [104]. A generalized volume-averaged model for pressure-driven and electroosmotic flows based on the assumption of an array of tortuous capillaries was proposed by Scales and Tait [105]. The model is based upon a scaling of the Navier Stokes equations extended by Coulomb and Forchheimer forces. Analytical solutions which are derived for several (simple) cases result in extensive expressions. While such capillary models may be appropriate for cellular materials, such as consolidated foams and membranes, they may have little relevance for packed beds of granular materials since they do not exhibit the same inter-pore connectivity and geometrical characteristics such as strongly varying cross-sections and concave rather than convex boundaries.

Consequently, the motivation for this work is the lack of a simple but sufficiently accurate

model for EOF in packed beds of granular materials. Hence, we proceed with a theory section where we examine the underlying physics based on dimensional reasoning. Then, the experimental methodology and materials used for this work are discussed. Subsequently, we proceed with the presentation of the results of defined experiments which are employed to derive a phenomenological expression of comparable simplicity to Blake-Kozeny law. Finally, the article is summarized with some concluding remarks.

3.3   Theory

In this section, EOF through packed beds of granular material is analyzed based on dimensional reasoning. Additionally, we derive a dynamic model for the center-of-mass motion of the fluidic parts of the experimental setup. This model is used to reveal the influence of different phenomena such as Joule heating in our experiment.

3.3.1   Dimensional analysis of electroosmotic flow through packed beds

In our previous work [106], we developed a model for the EOF in a porous frit based on dimensional reasoning. Here we use in principle the same methodology, but deviate in some important aspects which results in an improved averaging of the micro-scale to obtain a more accurate macro-scale behavior.

Generally, Smoluchowski observed that the electroosmotic velocity $\bar{v}_{eof}$ through a single pore - likewise to the flow around a particle - scales linearly with the electric field E, which exerts a Coulomb force in the EDL, the zeta potential ζ of the substrate in contact with the liquid, and the liquid's dynamic viscosity μ and permittivity ε [107]; it is

$$\bar{v}_{eof} \propto \frac{-\varepsilon\zeta}{\mu}E. \tag{3.1}$$

It can be assumed that the superficial EO velocity through a packed bed scales similarly and can be correlated to the relevant independent quantities: Zeta potential of the bed

50

particles, permittivity and viscosity of the liquid, Debye length l_D, electric field, effective hydraulic diameter d_h and the wetted surface area (per bed length) S_L according to

$$v_{eof} \propto q(\zeta, \varepsilon, \mu, l_D, E, d_h, S_L) \tag{3.2}$$

where q is a functional relationship to be derived by the rules of dimensional analysis. The physicochemical liquid parameters viscosity and permittivity along with the electric field do not require any further explanation. Other relevant quantities can have multiple definitions and we discuss our assumptions in the following:

Zeta potential - The zeta potential is an indirect measure for the electrical charge of a surface in contact with a liquid. The origin of the surface charge can be manifold and ranges from lattice defects, preferential adsorption and surface dissociation, just to name a few. The surface charges attract mobile, oppositely-charged counter-ions in the liquid which results in the formation of an EDL. The zeta potential is defined as the potential at the shear plane, which is a sub-layer of the EDL. Extensive review is available e.g. in [13, 26]. The zeta potential depends on various factors such as the kind of substrate and the ion content and pH value of the liquid [30]. Usually, the magnitude of the zeta potential is highest for low ion content in the liquid but there is no general theory which allows for its prediction. Nevertheless, since the zeta potential is an important parameter for many disciplines, various empirical correlations for different substrates can be found in literature as e.g. [30, 50, 108, 109]. In this work, we perform streaming current experiments to obtain an empirical correlation for the zeta potential of borosilicate as a function of the pH value and the ionic strength of an aqueous NaCl electrolyte. The ionic strength I captures the influence of the overall ion content. It can be calculated from $I = \frac{1}{2} \sum_i \bar{z}_i^2 c_i$ where $\bar{z}_i$ and c_i are the valency and the concentration of the ion species i.

Debye length - The Debye length is the physicochemical property which approximately

describes the thickness of the EDL. That is, it gives an estimation of how far the electrostatic effect of the surface charges ranges into the liquid. Interestingly, the Debye length depends only on the liquid parameters and is independent of the surface properties, it is

$$l_D = \sqrt{\frac{\varepsilon R_g \bar{T}}{2IF^2}}, \tag{3.3}$$

where R_g is the universal gas constant, $\bar{T}$ is the absolute temperature and F is the Faraday constant. In terms of electroosmosis, the Debye length indicates the thickness of the volume where the Coulomb force induces electroosmosis. Additionally, for cases where the Debye length is on the same order as the pore diameter, the pore scale electroosmotic velocity (cf eq. (3.1)) scales also with the ratio of Debye length to pore diameter.

Effective hydraulic diameter - The effective hydraulic diameter is one of the macroscopic parameters of the packed bed which results from averaging of the microscopic characteristics. In terms of EOF, the effective hydraulic diameter is a measure for the liquid volume which is pumped due to the EDL flow; further discussion is made in conjunction with the surface area of the packed bed below.

In terms of conventional pressure driven flows, a non-circular pore can be expressed by an equivalent circular pore which features the same pressure loss for a given flow rate. Likewise, for a porous substrate consisting of an ensemble of non-circular pores of different cross-sectional areas, the effective hydraulic diameter describes a porous substrate consisting of uniform circular pores with the same pressure drop for the given flow rate. Note that the hydraulic diameter is four times the hydraulic radius. The hydraulic radius is defined for straight pores as the ratio of the cross-sectional area to the wetted perimeter $r_h = A_c/P_c$ (see any text book such as e.g. [101]).

For cross-sectional areas with a high aspect ratio, the hydraulic diameter concept becomes invalid; however, this is not the case in typical packed beds [99]. Also, the use of

the hydraulic diameter concept for laminar flows can introduce significant errors since the concept stems from turbulent flows, where the pressure loss depends primarily on the shear in the (wall) boundary layer, and thus scales with the wall surface area. For laminar flows friction also occurs within the fluid and the concept of hydraulic diameter is not recommended [99, 101]. However, since the electroosmotic flow is generated in a wall boundary layer as well, i.e. the EDL, the concept of hydraulic diameter is adequate.

In terms of packed beds of granular materials, there is another problem related to the regular concept since the varying cross sections result in a variable hydraulic diameter along the flow direction. A more appropriate hydraulic radius, or characteristic dimension of the porous medium, is the ratio of the volume of voids to their surface area [101].

In our work, we choose the approach of Mehta et al. [110] who also account for the influence of the outer channel wall, which contains the packed bed, on the flow by introducing an additional factor. This approach appears reasonable since the outer channel wall contributes to electroosmosis as well and the M factor allows for an assessment of the influence. Hence, the hydraulic diameter is given as

$$d_h = \frac{2}{3}\frac{\psi}{(1-\psi)}\frac{d_p}{M} \quad \text{where} \quad M = 1 + \frac{2d_p}{3d_{pb}(1-\psi)}. \tag{3.4}$$

Here, ψ is the porosity of the packed bed, d_p is the effective particle diameter, and d_{pb} denotes the diameter of the packed bed. If there is no influence of the outer channel wall, the M factor goes towards one and the hydraulic diameter is computed in the standard way (see any text such as [111]). Note that the effective particle diameter is a function of particle size and its distribution. We use binary mixtures of borosilicate micro spheres to prepare packed beds of different porosities. The effective particle diameter of a mixture of particles, with a number fraction x_i and mean diameter d_i for the particle i can be calculated according to $d_p = \sqrt{\sum_{i=1}^{n} x_i d_i^2}$ where $\sum_{i=1}^{n} x_i = 1$. For a constant particle density, the number fraction x_i of particle i can be calculated from the weight fraction w_i via $x_i = \frac{\frac{w_i}{d_i^3}}{\sum_{i=1}^{n} \frac{w_i}{d_i^3}}$ (cf. e.g. [112])

Wetted surface area - The wetted surface area is another important packed bed parameter since it determines (along with l_D) the volume where the electroosmotic flow is induced. Here, several considerations from the EOF in a single pore should be considered. For increasing channel sizes, the surface-to-volume ratio of a channel decreases and all boundary effects become less important. That is, the EOF flow in the tiny EDL is not sufficient to drag the liquid bulk by viscous forces if the hydraulic diameter of the pore is rather large. Typically, EOF is observed in pores having typical diameters of several hundreds of micrometers. Consequently, EOF only scales with the pore cross sectional area up to a certain degree. To increase the electroosmotic flow rate effectively, more pores rather than larger pores are need. Additionally, the length of a (homogenous) pore does not contribute to the flow rate but rather to the pressure which can be generated. Hence, to account for the active area where electroosmosis is generated, we consider the wetted surface area of the packed bed normalized with bed length as the relevant quantity. We use the specific surface area S_v per unit volume of a packed bed, consisting of a spherical particle mixture, according to the coordination number theory (cf. [113]) and arrive at

$$S_L = \pi r_{pb}^2 S_v = \pi r_{pb}^2 \frac{6 \sum_{i=1}^n x_i d_i^2}{\sum_{i=1}^n x_i d_i^3}. \tag{3.5}$$

We proceed with our dimensional analysis by applying Buckingham Π theorem (cf. [114]). The number of relevant physical quantities in eq. (3.2) corresponds to $n = 7$ while the physical dimensions -mass, time, length and charge- are $m = 4$. The Buckingham Π theorem gives $(n + 1) - m = 4$ preliminary dimensionless groups to develop a functional correlation between the physical quantities. We arrive at

$$\Pi_1 = \frac{v_{eof}}{\frac{\zeta \varepsilon}{\mu} E}, \Pi_2 = \frac{E}{\frac{\zeta}{S_L}}, \Pi_3 = \frac{E}{\frac{\zeta}{l_D}}, \Pi_4 = \frac{E}{\frac{\zeta}{d_h}}.$$

54

To obtain an easier interpretation in terms of physics, we rearrange the preliminary dimensionless groups and choose

$$Sm = \Pi_1 = \frac{v_{eof}}{\frac{\zeta\varepsilon}{\mu}E}, \quad RW = \frac{\Pi_3}{\Pi_4} = \frac{l_D}{d_h}, \quad PB = \frac{\Pi_2}{\Pi_4} = \frac{S_L}{d_h} \tag{3.6}$$

to obtain three dimensional numbers which comprise physicochemical characteristics of the liquid as well as microscopic and macroscopic packed bed parameter. The first dimensionless group is the ratio of superficial packed bed to pore-scale electroosmotic velocity. It follows the general Smoluchowski observation eq. (3.1) and expresses the physicochemical characteristics of liquid and substrate. Hence, we dedicate this dimensionless group to Marian von Smoluchowski and name it Electroosmotic Smoluchowski Number Sm. The microscopic structure is reflected by the second dimensionless group, which is the ratio of Debye length to the hydraulic diameter. The dimensionless group allows for two kinds of interpretations. On the one hand, there is an interpretation in terms of viscous forces. It indicates the length scales of the liquid domains which are "active" and "passive". That is, the EDL where electroosmosis is induced and the liquid bulk which is dragged by viscous interactions. For larger ratios, a plug flow profile in the pore can be assumed. If the ratio is too large, the EDL flow is not sufficient to drag the bulk liquid. On the other hand, there is an electrical interpretation and the ratio indicates whether there is an EDL overlap in the pore. For $d_h/l_D \lesssim 1$, the EDL overlap result in a diminished electroosmotic pore-scale flow. The first paper on this effect in cylindrical capillaries was published by Rice & Whitehead [115] and, thus, we name this dimensionless group Rice-Whitehead number RW. Finally, the third number correlates macroscopic and microscopic packed parameters. It can be best explained by an example. For a constant specific wetted surface area, the electroosmotic flow increases with a decreasing hydraulic diameter, since this is equivalent to a higher number of pores, while the porosity remains the same. We name this number Packed-Bed

PB. Finally, the functional relationship $\Pi_1 = \Phi(\Pi_2, \Pi_3, \Pi_4)$ can be rewritten as

$$Sm = \Phi(RW, PB), \tag{3.7}$$

where the form of the function Φ has to be determined by a set of experiments.

3.3.2   Center-of-mass-model of the fluidic experimental setup

In this work, we utilize a capillary interface tracking method to measure the electroosmotic flow rate which is induced in the packed bed. Here, a capillary tube with a known diameter is connected to the packed bed and the electroosmotic flow induced due to an applied electric field forces the liquid interface to move in the capillary; this method has been utilized by several researchers including refs. [84, 87]. In these works, the authors assume the volumetric flow rate in the capillary to be identical to the electroosmotic flow rate. However, this approach neglects the fact that the capillary flow and other various physical phenomena impact (diminishes) the electroosmotic flow rate. Therefore, we develop a center-of-mass model of the experimental set-up to study its dynamic behavior. Another motivation comes from Joule heating; a term which describes the heat production which occurs when an electrical current is induced in the liquid by the application of the electric field. Research on this effect has been generally performed for single microchannels/capillaries. Joule heating may result in non-uniform temperature profiles across the channel which can have a profound influence on most liquid properties such as density, permittivity, viscosity, etc. [27, 116]. It is difficult to measure the influence of Joule heating on the packed bed and we utilize our model to extract this information from the experimental data.

Figure 3.1(a) gives the sketch of the fluidic parts of the experimental setup used to determine the electroosmotic flow which is induced in a packed bed of granular materials. The setup consists of a liquid reservoir (beaker), the packed bed, a T-connection and an
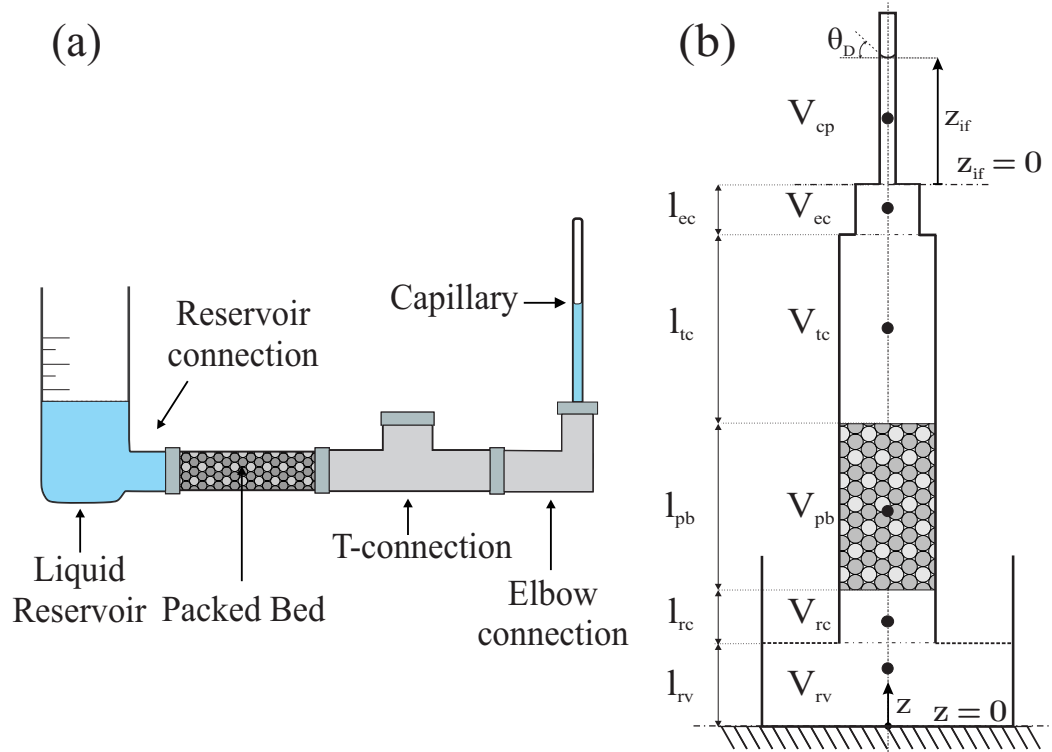
Figure 3.1: (a) Experimental setup for liquid interface tracking to measure the EOF velocity; (b) Schematic of the fluidic experimental used for the translational centre-of–mass model.

elbow connection which also contains the capillary tube. The electric field, induced by electrodes in the reservoir and the T-junction, pumps the liquid from reservoir into the capillary. Figure 3.1(b) shows the corresponding principle sketch which is used to track the translational center-of-mass of the liquid in the setup. The principle sketch comprise all compartments of the fluidic setup where each compartment has a certain height and a volume, the solid circles indicate the position of the respective center-of-mass. We introduce a 1D z-coordinate system with the origin at the bottom of the reservoir. For the sake of simplification, we introduce another z_{if}-coordinate system which tracks the position of the air/liquid interface in the capillary. Both coordinate systems are coupled to each other.

Overall, we simplify the set-up to be one-dimensional and apply Newton's law to the

system's center-of-mass z_c for the total liquid volume consisting of liquid reservoir (rv), reservoir connection (rc), packed bed (pb), T-connection (tc), elbow connection (ec) and capillary (cp); the respective index is given in the brackets. Then, Newton's second law, which states that the momentum change of the center-of-mass equals the forces which act on it, can be written according to

$$\frac{d}{dt}\left(\rho V_T \frac{dz_c}{dt}\right) = \sum_j F_j \tag{3.8}$$

The total volume corresponds to $V_T = V_{rv} + V_{rc} + \psi V_{pb} + V_{tc} + V_{ec} + V_{cp}$. The system's center-of-mass can be derived by a momentum balance of the single mass of the different compartments, i.e. $z_c V_T = z_{rv} V_{rv} + z_{rc} V_{rc} + z_{pb} \psi V_{pb} + z_{tc} V_{tc} + z_{ec} V_{ec} + z_{cp} V_{cp}$. We insert this relationship into eq. (3.8) and consider the following: The centre-of-mass and the volume of all compartments but the capillary are constant. This assumption is justified for the reservoir as well since the liquid volume is very large and a change requires a considerable pumping time. Also, the centre of mass of the capillary moves identically as the air/liquid interface in the capillary, i.e., $\frac{dz_{cp}}{dt} = \frac{dz_{if}}{dt}$. The capillary volume and center-of-mass can be expressed as $V_{cp} = A_{cp} z_{cp}$ and $z_{cp} = l_{rv} + l_{rc} + l_{pb} + l_{tc} + l_{ec} + \frac{z_{if}}{2} \equiv l_T + \frac{z_{if}}{2}$, respectively. Hence, Newton's Law can be written in terms of the coordinate of the moving interface as

$$\frac{d}{dt}\left(\rho V_T \frac{dz_c}{dt}\right) \cong \rho A_{cp}\left(z_{if}\frac{d^2 z_{if}}{dt^2} + 2\left(\frac{dz_{if}}{dt}\right)^2 + \left(l_T + \frac{z_{if}}{2}\right)\frac{d^2 z_{if}}{dt^2}\right) = \sum_{j=1} F_j \tag{3.9}$$

where the following forces act on the system's center-of-mass:

Electroosmotic force: This force is induced when an external electric field is applied to the packed bed. The electroosmotic flow does not induce viscous losses, to good approximation, since it is generated within the packed bed. Hence, the product of electroosmotic

flow rate and an appropriate viscous resistance of the packed bed can be interpreted as an electroosmotic pressure rise as defined by $\Delta p_{eof} \equiv R_\mu \dot{V}_{eof}$. Here, the parameter R_μ is the viscous resistance of the packed bed that results in a similar (viscous) pressure drop for the same flow rate which is induced by a pressure difference across the bed. We use the Blake-Kozeny equation [117] which correlates the pressure drop across the packed bed to the superficial velocity and arrive in

$$F_{eof} = A_{pb}\Delta p_{eof} = A_{pb}\, K_1 \frac{l_{pb}\mu}{d_p^2}\frac{(1-\psi)^2}{\psi^3}v_{eof} \qquad (3.10)$$

We note that the volume-averaging of the microscopic packed bed features results in a rigorous description of the macro-scale resistance R_μ as given in eq. (3.10). Here, the proportionality constant K_1 depends on the packed bed structure. For an array of (uniform) spheres that are just touching, K_1 varies from about 140 to 220 depending on whether the lattice cell arrangement is simple cubic, face-centered cubic, or body-centered cubic [118]. The value of 180 is often used, as it captures experimental results for viscous flow through unconsolidated porous media within $\pm 50\%$ [119]. Other sources use a range of 72 to 150 for consolidated porous media as cited in many texts [101]. Here, we have to consider that most of the work in literature determines the proportionality constant using homogenous spheres of sizes on the order of mm or even higher. Additionally, these experiments are always performed using pressure driven flows through the packed bed. Contrarily, particles as small as $6\mu m$ and electroosmotic flows are used in the current work. Hence, we consider the proportionality constant K_1 as a fitting parameter which has to be determined from our experiments. In detail, we assume that initial flow rate in the capillary is (almost) purely due to electroosmosis and other phenomena have a minor influence at this early time. The average value for the fitting coefficient K_1 is found to be 3.66 ± 1.03 for all packed beds and experimental conditions used in this work. The large difference to the proportionality constant of viscous flow in packed beds are probably not only related to the different packed

bed structures but also to the different velocity profiles. While a pressure driven flow has a parabolic velocity profile, the electroosmotic flow profile is rather plug like where the velocity drops only in the very small EDL.

Viscous force: This force is related to the pressure drop that arises from the viscous losses of the liquid flow through the capillary; $F_{vis} \equiv A_{cp}\Delta p_{cp}$. We use a Hagen-Poiseuille approach to correlate the pressure drop in the capillary to the motion of the interface, which is valid for a laminar flow of incompressible and Newtonian fluids through conduits having constant cross sections. It is

$$F_{vis} = A_{cp}\frac{8\mu}{r_{cp}^2}z_{if}\left(\frac{dz_{if}}{dt}\right) \tag{3.11}$$

where r_{cp} is the radius of the capillary. This force acts against the electroosmotic force. The equation has been used extensively by many researchers to study the dynamic contact angle of a moving air/liquid interface in cylindrical capillary tubes [120–122].

Hydrostatic force: This force arises due to the increasing hydrostatic pressure which is induced when the liquid column in the capillary rises due to the electroosmotic flow. The resulting force can be written as

$$F_g = A_{cp}\rho g\left(z_{if} - z_{if}(t=0)\right) \tag{3.12}$$

where ρ is the liquid density, g is the gravitational constant and $z_{if}(t=0)$ is the height of the air/liquid interface before the electroosmotic flow is induced. The hydrostatic force acts against the electroosmotic force.

Capillary force: This force reflects the influence of capillarity, which is two-fold in our system. On the one hand, the surface tension between liquid and air along with the

adhesive force between the liquid and the capillary results in capillary action. That is, the liquid moves in the capillary (independent of electroosmosis) until an equilibrium with the gravitational force is achieved. Whether the liquid sinks or rises, depends on the contact angle of the air/liquid interface with the solid . That is, the capillary force can be formulated the standard way as $F_c = A_{cp} \frac{2\sigma_o}{r_{cp}} \cos(\theta)$ where σ_o is the liquid-air surface tension, and θ is the contact angle. We use $\sigma_o = 0.072 N/m$ for the surface tension of water-air. The contact angle of a dynamic (advancing or receding) interface not only depends on the material properties but also on the interface velocity; hence it deviates from its equilibrium value. This phenomenon is observed for both natural (capillary action) and forced capillary flows. Several studies investigated the influence of interface velocity on contact angle and derived a number of empirical and theoretical models [123–125]. Most of these studies are based on two approaches known as (i) hydrodynamic theory and (ii) molecular-kinetic theory as explained [126]. For the current work, we have a forced moving interface and we adopt the model based on the molecular kinetic theory as proposed by Blake & Haynes [127] which expresses the dynamic contact angle θ_D as

$$\cos(\theta_D) = \cos(\theta_e) - \frac{\sigma'}{\sigma_o} \sinh^{-1}\left(\frac{v}{v'}\right), \qquad (3.13)$$

where the velocity of the interface corresponds to $v = dz_{if}/dt$ and θ_e is the (static) equilibrium contact angle. We measure the equilibrium height in the capillary before each experiment to be $11.7mm \pm 0.2mm$. The application of the Washburn correlation $h_{eq} = \frac{2\sigma_o \cos\theta_e}{r_{cp}}$ results in a corresponding equilibrium contact angle of $\theta_e = 62 \pm 1°$. The equilibrium contact angle is also analyzed by using a high resolution camera and a good agreement is observed. The parameter σ' is proportional to the thermal energy and has units of surface tension while the parameter v' is a velocity determined by some molecular quantities (average frequency of displacement and distance between minima of the effective free energy). These values cannot be directly computed or experimentally measured [128]. Hence, we

choose the values $\sigma' = 0.0172 N/m, v' = 5 \cdot 10^{-3} \frac{m}{s}$ as proposed by Popescu et al. [128] for a system consisting of a smooth glass capillary, air and aqueous electrolytes. Furthermore, we linearize the inverse hyperbolic sine according to $\sinh^{-1}\left(\frac{v}{v'}\right) \approx v/v'$ which is a good approximation for low interface velocities. Hence, the final capillary force can be written as

$$F_c = A_{cp}\frac{2\sigma}{r_{cp}}\left(\cos\theta_e - \frac{\sigma'}{\sigma_o v'}\frac{dz_{if}}{dt}\right). \tag{3.14}$$

After inserting all forces into eq. (3.9) and some rearrangements, we arrive in

$$gz_{if} + \left(\frac{2\sigma'}{\rho r_{cp}v'} + \frac{8\mu z_{if}}{\rho r_{cp}^2}\right)\frac{dz_{if}}{dt} + 2\left(\frac{dz_{if}}{dt}\right)^2 + \left(l_T + \frac{3}{2}z_{if}\right)\frac{d^2 z_{if}}{dt^2}$$
$$= 3.66\frac{A_{pb}}{A_{cp}}\frac{\mu(1-\psi)^2 l_{pb}}{\rho d_p^2 \psi^3}v_{eof} + \frac{2\sigma_o\cos\theta_e}{\rho r_{cp}} \tag{3.15}$$

We now pass to a non-dimensionalized system for the sake of convenience. The length coordinate is scaled with the radius of the packed bed to obtain the dimensionless coordinate; i.e., $Z_{if} = z_{if}/r_{pb}$. The velocity is scaled with a characteristic velocity v_0 to obtain a dimensionless $V_{eof} = v_{eof}/v_0$, where $v_0 = \frac{\zeta_0\varepsilon}{\mu}E_0$ is an electroosmotic pore-scale velocity. The time is scaled with a characteristic (electroosmotic) convective scale to obtain the dimensionless time $T = tv_0/r_{pb}$. We use the non-dimensional variables just as defined and normalize all terms with a hydrostatic pressure to obtain after some rearrangements

$$Z_{if} + (\Omega_0 + \Omega_1 Z_{if})\frac{dZ_{if}}{dT} + 2\Omega_2\left(\frac{dZ_{if}}{dT}\right)^2 + \Omega_2\left(\frac{l_T}{r_{pb}} + \frac{3}{2}Z_{if}\right)\frac{d^2 Z_{if}}{dT^2} = \Omega_3 + \Omega_4. \tag{3.16}$$

The non-dimensional groups

$$\Omega_0 = \frac{2\sigma' v_0}{g\rho r_{cp} r_{pb} v'}, \ \Omega_1 = \frac{8\mu v_0}{g\rho r_{cp}^2}, \Omega_2 = \frac{v_0^2}{g r_{pb}}, \ \Omega_3 = 3.66\frac{\mu v_0 (1-\psi)^2}{\rho g \psi^3}\frac{r_{pb} l_{pb}}{d_p^2 r_{cp}^2}V_{eof}, \ \Omega_4 = \frac{2\sigma_o \cos\theta_e}{g\rho r_{cp} r_{pb}}$$

(3.17)

arise from the non-dimensionalization. The dimensionless groups Ω_0 and Ω_4 indicate the ratio of capillary force to hydrostatic force. In detail, the first group arises from the dynamics of interface while the second is related to the static interface. Both groups can be interpreted as inverted Bond numbers which indicates the importance of surface tension forces compared to body forces such as the gravitational force. The dimensionless group Ω_1 is the ratio of viscous and hydrostatic forces in the capillary. It is comparable to an inverted Archimedes number which is, however, rather used for phenomena which involve buoyancy effects. The ratio of inertial to hydrostatic force, which is equivalent to an inverted Richardson number, is expressed by Ω_2. Finally, Ω_3 shows the significance of the electroosmotic force relative to the hydrostatic force. Note that, unlike the other dimensionless groups, we cannot compute this group a priori to the experiments. In other words, we have to extract Ω_3 from the experimental observation of the capillary interface position $Z(T)$ over time to infer the real electroosmotic flow in the packed bed.

Unfortunately, there is no analytical solution of this 2nd order non-linear ODE immediately available. Hence, we perform a magnitude of order analysis and compute the dimensionless groups for typical values of our problems. That is, $r_{pb} \sim 1 \ cm, r_{cp} \sim 1 \ mm, l_{pb} \sim 1 \ cm, \ d_p \sim 10 \ \mu m, \ \psi \sim \ 0.1$ together with values for the density, viscosity and surface tension for water and glass-water, respectively. We obtain $\Omega_0 \sim 10^{-3}$, $\Omega_1 \sim 10^{-3}$, $\Omega_2 \sim 10^{-5}$, $\Omega_3 \sim 10^7$, $\Omega_4 \sim 1$. We conclude that the influence of inertia is rather negligible and eq. (3.16) can be simplified to:

$$Z_{if} + \left(\Omega_o + \Omega_1 Z_{if}\right)\frac{dZ_{if}}{dT} \approx \ \Omega_3 + \Omega_4$$

(3.18)

An analytical solution exists but involves the complex Lambert-W function which cannot be expressed in terms of elementary functions. Nevertheless, to correlate the EOF, which is generated in the packed bed, to the motion of the air/liquid interface in the capillary, we fit a 3rd-order polynomial regression to the $Z(T)$ data that we measure in our experiments. The obtained regression is used to determine Ω_3 and V_{EOF} from eq. (3.18) over the measurement time, respectively. It is also used to infer the proportionality constant K_1 which correlates the electroosmotic flow through a packed bed with an equivalent pressure drop of a viscous flow based on Blake-Kozeny equation.

3.4 Experimental methodology

This section describes details of the experimental setups, methods and materials that we use. Here, we have to distinguish between the electroosmosis and the streaming current measurements.

3.4.1 Electroosmosis

Experimental setup

The experimental setup for the EOF measurements consists of several fluidic components, electrical instruments along with electronic equipment for data processing. A sketch of the experimental setup is given in figure 3.2. In detail, the setup consists of an electrolyte beaker which is connected to a glass tube which contains the packed bed of granular material. From the other end, a capillary made from borosilicate glass ($r_{cp,o} = 3mm, r_{cp,i} = 0.6mm, l_{cp} = 30.48cm$, McMaster-Carr, Aurora, OH, USA) is connected via a T-junction ($d_{T,i} = 8.7mm$, Cole-Parmer, Montreal, QC, Canada) and an elbow connection ($d_{e,i} = 8mm$, glass, custom made) to the glass tube. Platinum wire electrodes ($d_{Pt} = 0.584mm$, LabSmith Inc., CA, USA) are inserted to the beaker and the T-junction. The electrodes are connected to a a high voltage power supply (Bertan Model 105-03R, Equiptek Labs Inc., CA, USA). The
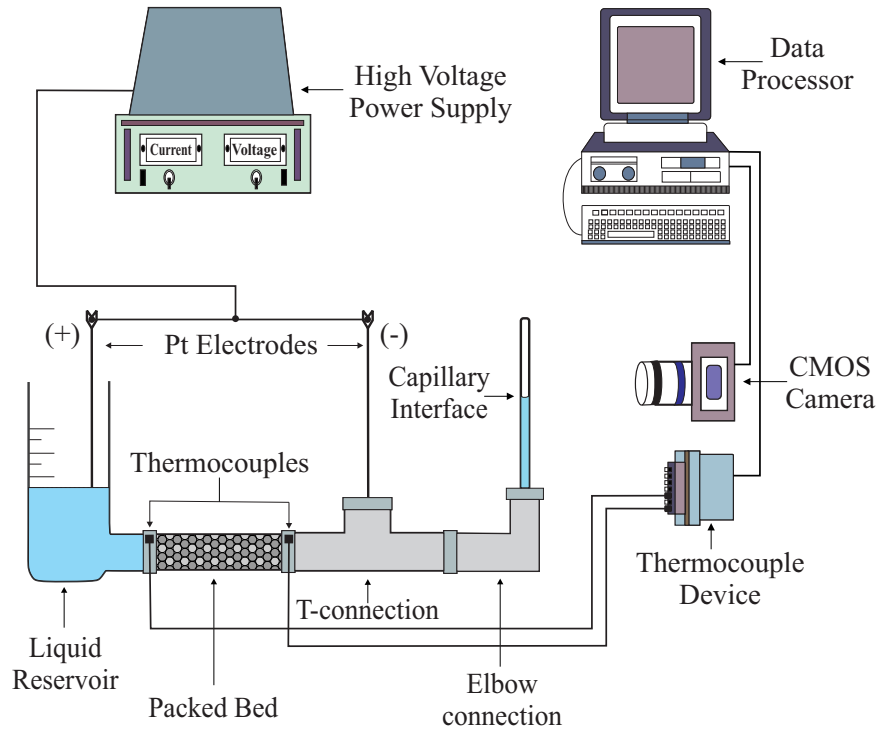
Figure 3.2: Schematic of the experimental setup utilized for the electroosmotic flow experiments.

motion of the air/liquid interface is tracked by using a CMOS camera (DFK 23UM021, The Imaging Source, NC, USA). The data is analyzed by using the LabView Vision Builder software (National Instruments, Austin, TX, USA). To obtain insight into the influence of Joule heating, two PFA insulated thermocouples (5TC-TT-K-20-36, Omega Engineering, QC, Canada) are attached to the ends of the packed bed. Note that these temperature sensors contact the glass outside of the packed bed. It is not possible to insert electrically-based temperature sensors, such as a thermocouple or a Pt-100 resistance thermometer, into the liquid due to the humongous electric fields. This method only gives a rather rough idea of the temperature distribution in the packed bed.

Experimental procedure

First, we prepare packed beds from borosilicate glass particles. In detail, we utilize borosilicate microspheres with mean diameters of $6\mu m$ and $18\mu m$ (Microspheres-Nanospheres, NY, USA) as well as microspheres with mean diameters of $50\mu m, 140\mu m, 230\mu m$ and $1000\mu m$ (Mo-Sci Specialty Products, L.L.C, MO, USA). All packed beds are prepared in borosilicate glass tubes (Pegasus-Glass, ON, Canada) with an inner radius of $r_{pb} = 4.75mm$, the thickness of the glass wall is $1mm$. We prepare packed beds using binary particle mixtures in order to obtain a wide range of porosities, wetted surface areas and effective hydraulic diameters. It is important to retain the particles when the electroosmotic flow is generated in the packed bed. Different techniques are described in literature for the preparation of packed-bed particle-retainers, especially in the field of capillary electrochromatography. These techniques include gluing or sintering of the particles [129, 130] and in-situ polymerization of monolith column [131, 132] among others. Here, we adopt the method used by Bosch et al. [129], where particles are sintered in a way that creates two permeable retention frits at each end of the packed bed. This method appears especially suitable since it produces retention frits with the same features as those of the packed bed. First, a small part of the glass tube is filled with the particle mixture of the packed bed. These particles are consolidated, immersed in a solution of sodium silicate in deionized water, and sintered using a butane torch. The concentration of sodium silicate solution, sintering time and temperature are carefully optimized so that the frits maintain a porosity similar to the rest of the packed bed. Thereafter, the glass tube is filled with more particles until the desired packed bed length is achieved. The particle bed is compacted from the top using a Teflon rod in order to remove any cavities. Finally, the top of the packed bed is sintered in the same way as the first retention frit. After the fabrication, the packed beds are chemically treated to remove any contamination; the cleaning procedure is described in [62]. The porosity is measured by weighing the bed in a dry and water-saturated state using a precise

scale (AZ3102, Sartorius AG, Germany).

Before each electroosmosis experiment, the packed beds are equilibrated in the desired electrolyte solution for at least 48 hours. The electrolyte solutions of desired ionic strength and pH value are prepared using sodium chloride (NaCl, $\geq$ 99.0%, ACS reagent, Sigma-Aldrich, CA) dissolved in a DI water matrix ($\sigma \leq 1\mu S/cm$). The pH value of the aqueous electrolyte is adjusted due to the addition of either sodium hydroxide (NaOH, $\geq$ 97%, ACS reagent, Sigma-Aldrich, CA) or hydrochloric acid (HCl, 32% in water, ACS reagent, Fisher Scientific, CA). Conductivity and pH testings are performed before and after an electroosmosis experiment using a modular pH and conductivity meter (Mettler-Toledo, SevenMulti, Switzerland). We observe that the change in pH and conductivity is less than 1% for all measurements.

To perform an EOF experiment, the packed beds are assembled in the experimental setup as shown in figure 3.2. The aqueous electrolyte is filled in the reservoir along with the other compartments. To remove any gas bubbles inside the setup, the electrolyte solution is pumped through the fluidic parts and the packed bed by utilizing a syringe pump. The electroosmotic flow is induced by applying a voltage between the electrodes. This moves the electrolyte solution from the beaker through the packed bed, the T- and elbow connection into the capillary. Finally, a comprehensive set of experiments based on a full factorial design is performed to obtain the correlation Φ among the dimensionless groups as given in eq. (3.7). In detail, we used 9 packed beds, 3 pH values, 5 electric field strengths, and up to different 4 ionic strengths. The range of the experimental parameters are listed in table 3.1. All in all, 342 measurements were performed to cover the widest possible range of the dimensionless groups given in eq. (3.6).

3.4.2 Streaming current

We employ the streaming current method to infer an empirical correlation for the zeta potential of borosilicate in contact with an aqueous NaCl electrolyte of defined ionic strength

Parameter	Range
Electric field E / kV/m	$1.21 - 71.6$
Ionic strength I / mM	$0.01 - 50$
pH value / $-$	$4 - 9$
Debye length l_D / nm	$1.36 - 96.32$
Zeta Potential $-\zeta$ / mV	$33 - 138$
Porosity ψ / $-$	$0.146 - 0.320$
Specific surface area S_L/m	$3.51 - 14.74$
Effective hydraulic diameter $d_h/\mu m$	$2.57 - 19.70$

Table 3.1: Experimental parameter range of the electroosmosis experiments.

and pH value. The streaming current is, likewise to electroosmosis, one of the various electrokinetic phenomena. It is induced by a pressure-driven flow along a stationary surface which features an EDL. The convective charge transport in the EDL is termed streaming current and can be conveniently measured between an up and a downstream position. Often, streaming current measurements are conducted in very defined geometries. We use a microchannel formed by two parallel flat plates as proposed by [14]. The experimental values can be related to the zeta potential according to the Helmholtz Smoluchowski formula

$$\zeta = \left(\frac{\mu I_2}{\varepsilon b_2 h_2} \right) \frac{-I_{SC}}{\Delta p} \tag{3.19}$$

where b_2, h_2, l_2 are the channel width, height and length, respectively; I_{SC} is the measured (streaming) current and the Δp is the pressure difference which is applied to the channel [26]. Practically, streaming currents are measured for various pressure differences and the respective slope of the correlation $I_{SC} = f(\Delta p)$ is used in eq. (3.19).

Experimental setup

Figure 3.3(a) shows a schematic sketch of the experimental setup that is used for the streaming current experiments. In detail, the setup consists of the measurement (electrokinetic) cell and further fluidic and electrical components. Within the cell, there is a microchannel which wetted surface is made from borosilicate glass. The cell also contains two Ag/AgCl
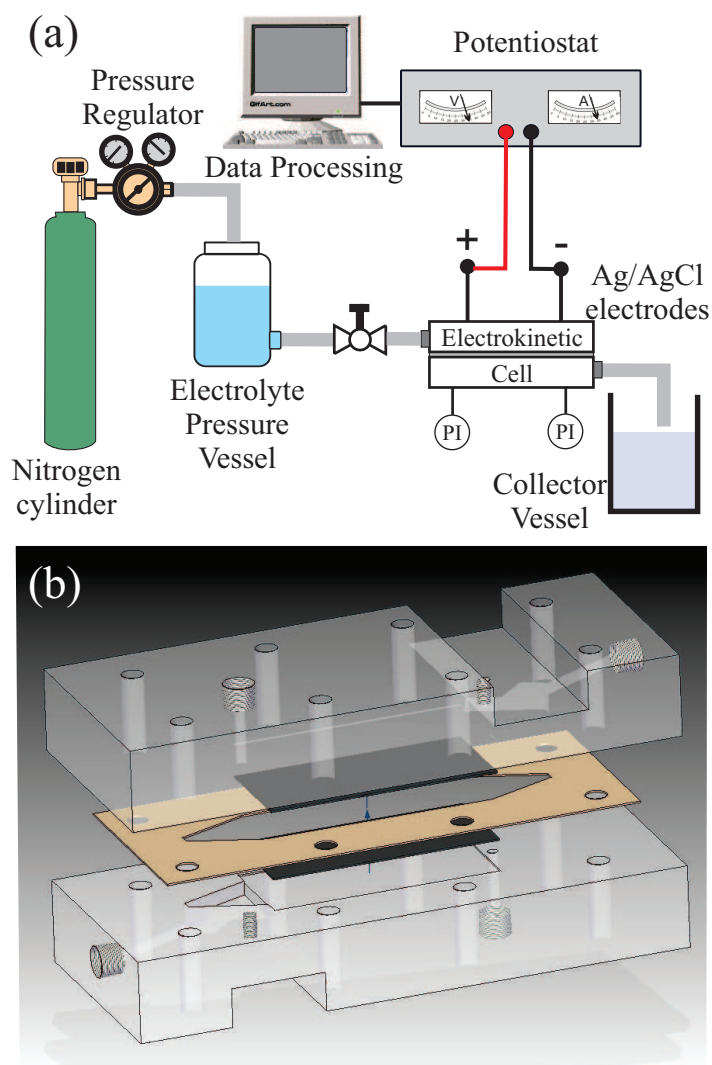
Figure 3.3: (a) Sketch of the streaming current setup; (b) Design of the streaming current measurement cell.

electrodes which join a precise potentiostat (PGSTAT302N, Metrohm Autolab B.V., The Netherlands) which measures various electrical signals. The cell is connected to a polyethylene vessel containing the aqueous electrolyte. This vessel can be charged with a controlled pressure by a nitrogen gas cylinder (Ultra High Purity 99.999%, MEGS, Canada) to pump the aqueous solution through the cell. The pressure drop across the cell is indicated by two pressure gauges which are connected to the cell.

Figure 3.3 (b) gives a detailed insight into the cell design. The cell is made from two Teflon® (PTFE) blocks and allows for the incorporation of two test wafers of dimensions $70mm \times 30mm \times 1.5mm$ to form the microchannel. We use borosilicate wafers of the same composition as the granular material of the packed bed for the sake of comparability. However, any material can be tested as long as it features the specified wafer dimensions. The blocks are assembled with two gasket in between. The inner rigid (spacer) gasket is made of PTFE and maintains a gap between the wafers to adjust the height of the microchannel $h_2 = 175\mu m$. The outer soft gasket is made of latex rubber and is required for sealing purposes.

Experimental protocol

The streaming current measurements are carried out according to the following procedure: First, borosilicate wafers are cleaned using the following cleaning procedure as described in [62]. Wafers and gaskets are then installed in the cell and the assembled device is connected to the setup. Verification of the microchannel height is done each time the cell is assembled by measuring the volumetric flow rate $\dot{V}$ vs. the pressure difference and compute the height according to $h_2 = \sqrt[3]{\frac{12 l_2 \mu \dot{V}}{b_2 \Delta p}}$. We use the same aqueous electrolyte solutions as for the electroosmosis measurements. First, the electrolyte solution is filled in the vessel which is then pressurized by the nitrogen gas. Before each experiment, the respective electrolyte is pumped through the cell for around 30 minutes at $\Delta p = 25kPa$. The actual experiment is undertaken by adjusting pressure differences in the range of $10kPa$ to $75kPa$; the measurement of the streaming current is done for 60 seconds at a constant pressure. We use the corresponding time-averaged value for data evaluation. For each ionic strength and pH, 5 pressure values are applied to obtain a correlation between streaming current and pressure difference. A total number of 60 experiments are performed for 5 pH values for different ionic strengths.

3.5 Results and discussion

We present the experimental results in three subsections. First, we discuss the results of the streaming current experiment. Second, we present results from the characterization of the packed beds to show the relationship between different packed bed parameters. Third, selected results of the electroosmosis experiments are shown and the correlation Φ between the dimensional group is inferred.

3.5.1 Streaming current

Figure 3.4 shows the zeta potentials of a borosilicate surface that are inferred from streaming current measurements for various ionic strength and pH values of the aqueous electrolyte.
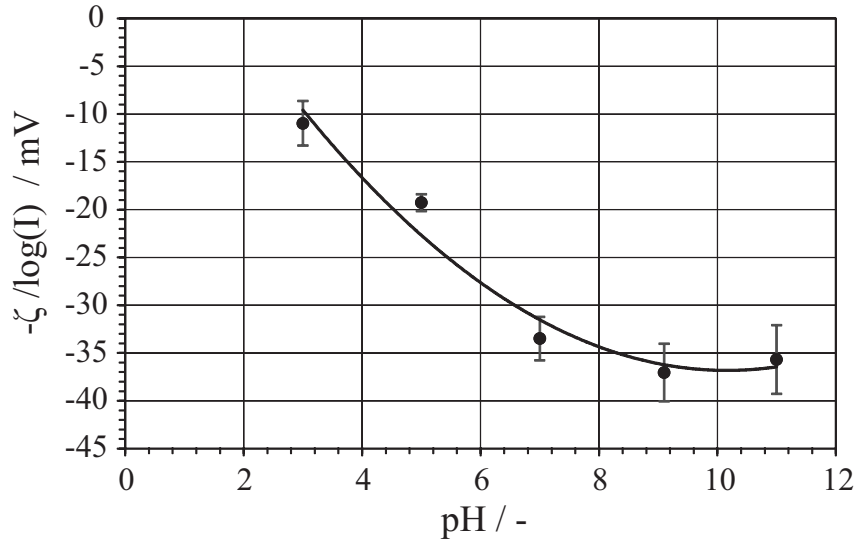
Figure 3.4: Zeta potential normalized with the negative logarithm of the ionic strength as a function of the pH.

We chose to normalize the zeta potentials with the respective negative logarithm of the ionic strength and plot them vs. the pH value. This leads to a collapse of various data points onto a single curve as shown in many works concerned with zeta potential measurements (cf. ref. [30]). In detail, the symbol indicates the average normalized values compiled from

various ionic strengths measurements at a constant pH value. The small standard deviations (for an electrokinetic experiment) underlines the high validity of the normalization approach. Between the pH values of 3 to 7, there is a rather linear increase of the magnitude of the normalized zeta potential. When the pH value exceeds 7, the slope decreases and the normalized zeta potential approaches a limiting value (plateau). This behaviour is in good agreement with the work of Scales et al. who investigated potassium chloride electrolytes in contact with fused-silica surfaces [46]. They noted that the occurrence of the plateau near a pH value of around 8 can be related to the entire deprotonation of the silanol surface sites so that a maximum of negatively charged sites is reached. A second-order regression results in

$$\frac{\zeta(pH)}{-log(I)} = \left(0.532\,pH^2 - 10.80\,pH + 18.04\right)mV \tag{3.20}$$

which can be used to give good accuracy for the phenomenological model that we propose. The fitting curve has a coefficient of determination value 0.965 and is given in figure 3.4 as well.

3.5.2 Packed bed parameters

As already discussed, binary particle mixtures are used for the packed bed preparation to obtain a phenomenological model of general applicability. The properties of the packed beds depend on several factors like the mixture composition, the size ratio of the spheres as well as the mixing procedure. Different models have been developed to describe the porosity of mixed particle beds. However, the accuracy can be insufficient and/or the experimental applicability can be difficult [113, 133–139]. For example, we are not able to enforce a regular packing structure and random packing of binary mixtures results in highly unpredictable packing densities [133]. Hence, we discuss the resulting packed bed parameters in this work solely on the definitions given in section 3.3.1 along with the measured porosities. In other words, we do not assume any model to predict porosities. Note that we prepare 12 packed

beds but utilize only 9 in the EOF experiments since three packed beds had comparable features to others.
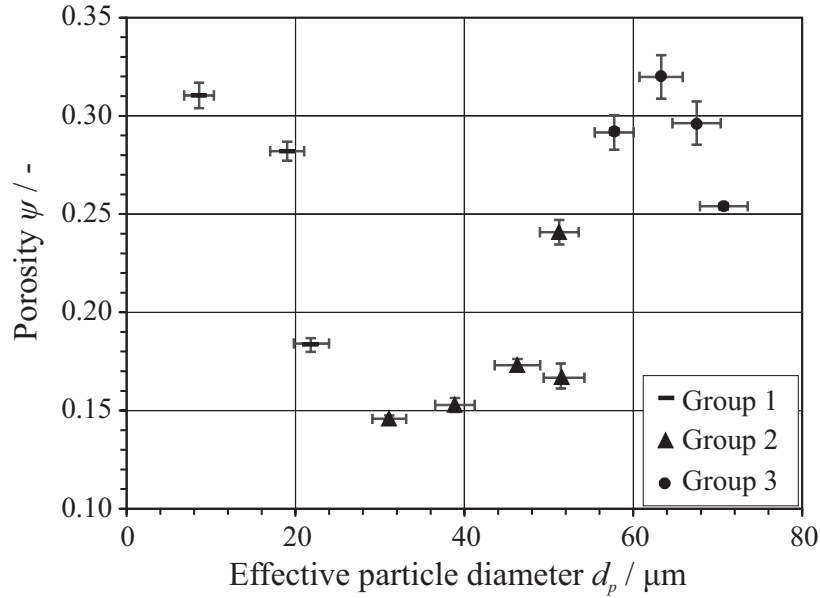
Figure 3.5: Porosity of the packed bed vs. the effective particle diameter of the particle mixtures.

Figure 3.5 shows the relationship between the effective particle diameter and the measured porosities for the different packed beds used in this work. Recall that for a randomly packed bed of a homogenous spherical particles, with a small particle diameter to packed bed diameter, the porosity hardly scales with the particle diameter. Literature values for dense random packing varies between $\psi = 0.359..0.375$ [140]. In contrast, for binary mixtures we find different intervals where, evidently, different mechanisms prevail. Note that the following interpretation is a pure qualitative approach and there are rather smooth transitions between the intervals than stringent boarders. Additionally, we do not have insight into the packing structures that we achieve. In the first interval, we observe that the porosity decreases with an increasing effective particle diameter. Then, the situation changes completely and we observe an increase of the porosity with an increasing effective

particle diameter. Subsequently, the trend changes again and the porosity decreases as the effective particle diameter further increases. The categorization into these intervals also allows for a better interpretation of the underlying mechanisms. To do so, we assign the particle mixtures of an interval to a corresponding group as given in table 3.2. The mixtures are characterized by the small to large particle diameter ratio $\delta = \frac{d}{D}$ and the volume fraction v_d of the small particles.

Group No.	d / μm	D / μm	$\delta = \frac{d}{D}$	$v_d/-$
1	18	230	0.08	0.1
	18	230	0.08	0.2
	6	50	0.12	0.1
2	50	1000	0.05	0.4
	50	1000	0.05	0.5
	18	140	0.13	0.02
	18	100	0.18	0.04
	18	50	0.36	0.1
3	50	230	0.22	0.25
	50	140	0.36	0.2
	18	50	0.36	0.5
	50	100	0.50	0.25

Table 3.2: Particle size ratios and weight fractions for different packed beds.

We realize that the packed beds in group 1 are prepared based on particle mixtures with a high difference in particle size ($\delta \simeq 0.1$) and a relatively low volume fraction of small particles ($v_d \simeq 0.1$) . We assume that such mixtures promote the formation of a "skeleton" in the packed bed. That is, there is a large structure which consists solely of large particles and the void volume of this skeleton provides a space where small particles can accumulate [133]. Considering the high porosity values of around 0.3, we assume that the mixtures with a relatively low volume fraction of small particles $v_d = 0.1$ rather behave like randomly packed bed of a homogenous particles. The mixture with $v_d = 0.2$ features a lower porosity since the small particles occupy the skeleton's void volume.

Group 2 consists of particle mixtures with either very low particle size ratio ($\delta \simeq 0.05$)

along with a high volume fraction of small particles ($v_d \simeq 0.4..0.5$) or with a medium size ratio ($\delta \simeq 0.13..0.36$) and a low volume fraction of small particles ($v_d \simeq 0.02..0.1$). The first combination should feature skeleton formation and we assume that the high volume fraction of small particles considerably fills the void volume of the skeleton. The other combination may promote a skeleton formation in the packed bed as well. However, the very low volume fraction of small size particles occupies only a small part of the void volume. The increase and decrease in porosity that we observe for this group cannot be easily explained and we assume that these mixtures create complex packed bed structures which influence the porosity.

For group 3, there is the highest size ratio of the particles ($\delta \simeq 0.2..0.5$) along with the highest fractions of small particles ($v_d \simeq 0.2..0.5$). We assume that no significant skeletal formation takes place due to the comparable sizes and concentration of small and large particle. This is supported by the relatively high porosity values which are close to those of (dense) randomly packed beds of homogenous particles..

Next, we evaluate the influence of the outer channel wall on the packed bed by computing the M factor as defined in eq. (3.4). In detail, the M factor comprise the ratio of effective particle diameter to packed bed diameter. This ratio has also an important influence on the packing structure. A homogeneous packing structure is only achieved when the ratio of the effective particle size to the packed bed diameter is smaller than 0.1 [133].

Figure 3.6 plots the M factor versus the respective effective particle diameter of the packed bed. We observe that the M factor increases as the effective particle diameter increases. The correlation is of a linear nature, to good approximation. Nevertheless, the values for all packed beds are almost equal to 1 so that we can conclude that there is practically no influence of the outer channel wall on the electroosmotic flow in the packed bed. At the same time, the M value close to 1 means that we can assume a homogeneous packing structure for all packed beds.
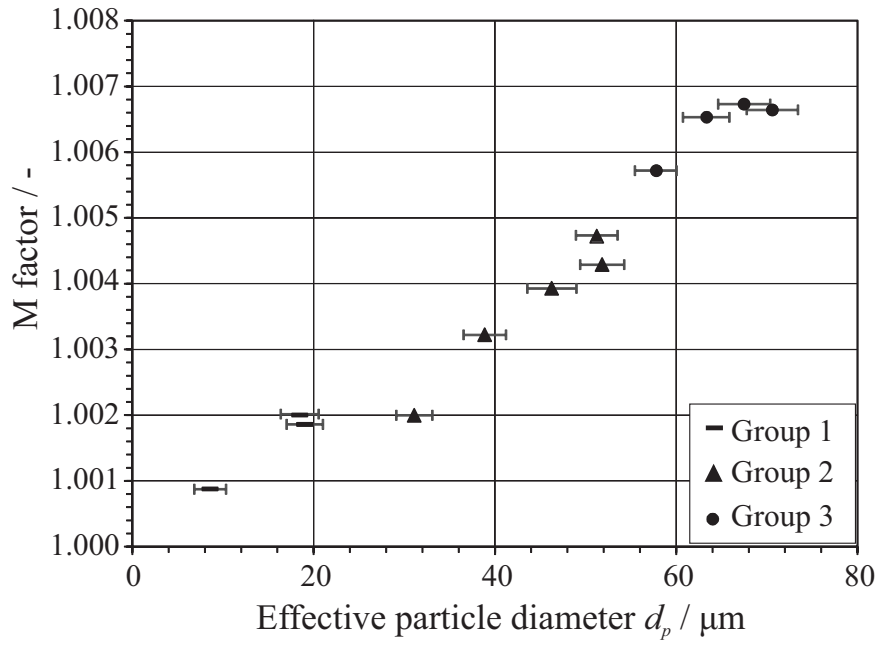
Figure 3.6: M factor vs. the effective particle diameter of the packed beds.
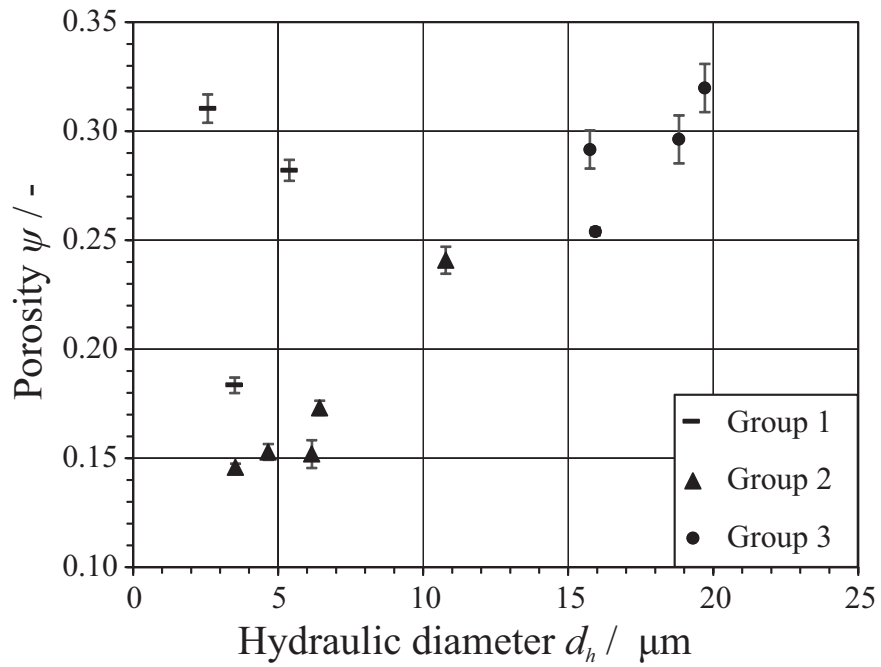

Figure 3.7: Porosity vs. the hydraulic diameter of the packed beds.

Figure 3.7 shows the trend between the (measured) porosity and the (computed) hydraulic diameter of the packed beds. In terms of group 2 and 3 particle mixtures, we find a linear increase in porosity with increasing hydraulic diameter. The group 1 mixture does not scale as the other groups and gives a rather inconsistent picture with large differences in porosity for similar hydraulic diameters. This is understood if we consider that the group 1 mixture with the lowest porosity has also the highest volume fraction of small particles which lowers the porosity.
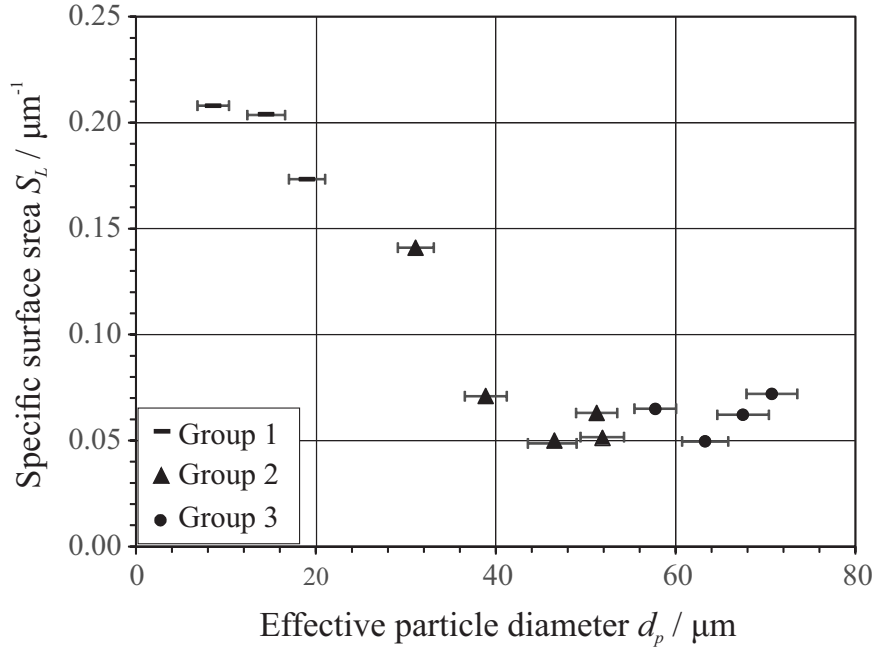
Figure 3.8: Specific surface area vs. the effective particle diameter of the packed beds.

Figure 3.8 shows the relation between the (calculated) specific surface area and the effective particle diameter. If we had a homogenous particle bed, the specific surface area would just decrease as the particle diameter increases. It is obvious that the usage of binary particle mixtures lead to more complex phenomena. As expected, we find the highest values of specific surface area for small effective particle diameters. Then, the specific surface area considerably decreases until the effective particle diameter approaches a value of around $40\mu m$. That is, the group 1 and some of the group 2 mixtures, where we assume skeleton

77

formation and/or we have a large volume fraction of small particles, show a similar behaviour as a packed bed of homogenous particle. For larger effective particle diameters than around $40\mu m$, the specific surface area remains more or less constant, independent of the effective particle diameter. Here, we assume that the influence of effective particle diameter is compensated by the simultaneous increase in porosity (cf. figure 3.5). This happens for mixtures with either no skeleton formation or for those with a low volume fraction of small particles.

Figure 3.9 shows a plot of the hydraulic diameter against the effective particle diameter.
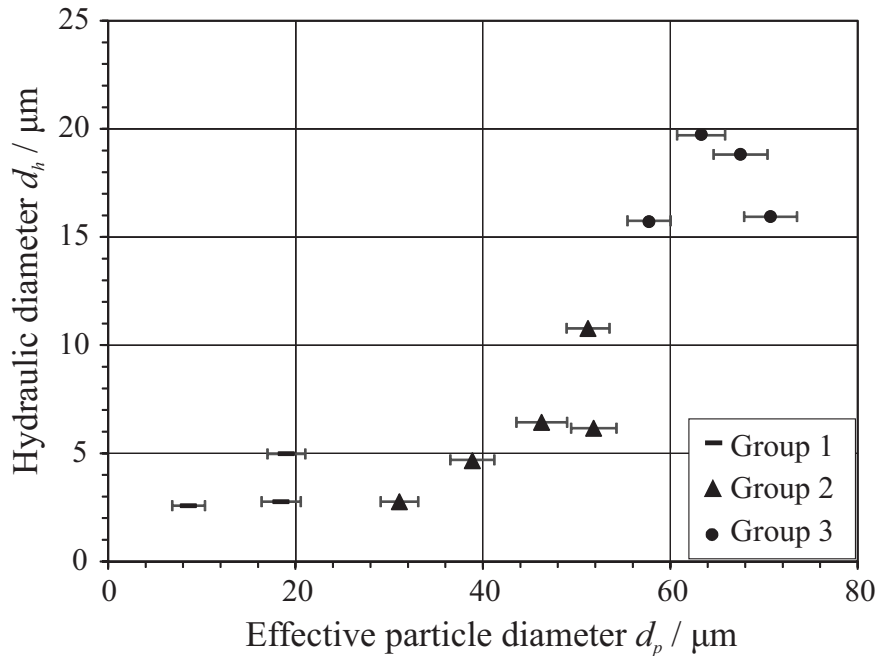
Figure 3.9: Hydraulic diameter vs. effective particle diameter of the packed beds.

For a packed bed of homogeneous particles having a more or less constant porosity, there should be an increase of the hydraulic diameter as the particle diameter increases (cf. eq. (3.4)). In terms of our binary mixtures, we see that the hydraulic diameter remains more or less constant until the effective particle diameter approaches a size of roughly $40\mu m$; i.e. for group 1 mixtures (skeleton formation) and group 2 mixtures with a high fraction

of small particles. We assume that the simultaneous decrease of porosity (cf. figure 3.5) compensates the influence of the effective particle diameter. For effective particle diameters larger than around $40\mu m$, the hydraulic diameter increases which is observed for group 2 (low volume fraction of small particles) and group 3 (no skeleton formation). The lowest and highest values are observed for group 1 and 3 mixtures, respectively; i.e., with and without skeleton formation.

3.5.3 Electroosmosis

Figure 3.10 shows the result of a typical electroosmosis experiment incorporating a packed with a porosity of $\psi = 0.241$ and an electrolyte of ionic strength $I = 0.01mM$ and $pH = 6$. On the left-hand side y-axis, the symbols give the measured (dimensionless) position of the air/liquid interface in the capillary Z over the (dimensionless) measurement time T. Initially, the interface is located at $Z \approx 2.4$ due to capillary action (wicking). After the application of the voltage, an applied electrical field of $E \approx 10.1kV/m$ is induced in the packed bed. The electric field induces the EOF and the interface in the capillary starts to move. First, we observe a linear correlation between interface position and measurement time. At longer times, a decrease of the slope is observed. The solid line shows the 3-order polynomial regression of the experimental data that we use for further data evaluation.

As mentioned in section 3.3.2, we compare two different approaches to compute the superficial electroosmotic velocity, the corresponding results are plotted using the right-hand side y-axis of the diagram in figure 3.10. For the first approach, we assume that the EOF is not influenced by the phenomena in the capillary. That is, we use the capillary flow rate, inferred from $Z(T)$, and apply a continuity assumption; i.e. $V_{eof} \equiv (dZ/dt)A_{cp}/A_{pb}$. The result is given as the dashed line. We observe here that as the time proceeds, a continuous decrease of V_{eof} is found in a linear trend. The situation changes drastically if we use eq. (3.18), which includes the influence of the rising column, the viscous losses and the moving contact line in the capillary, to extract the V_{eof} from the dimensionless group Ω_3. The
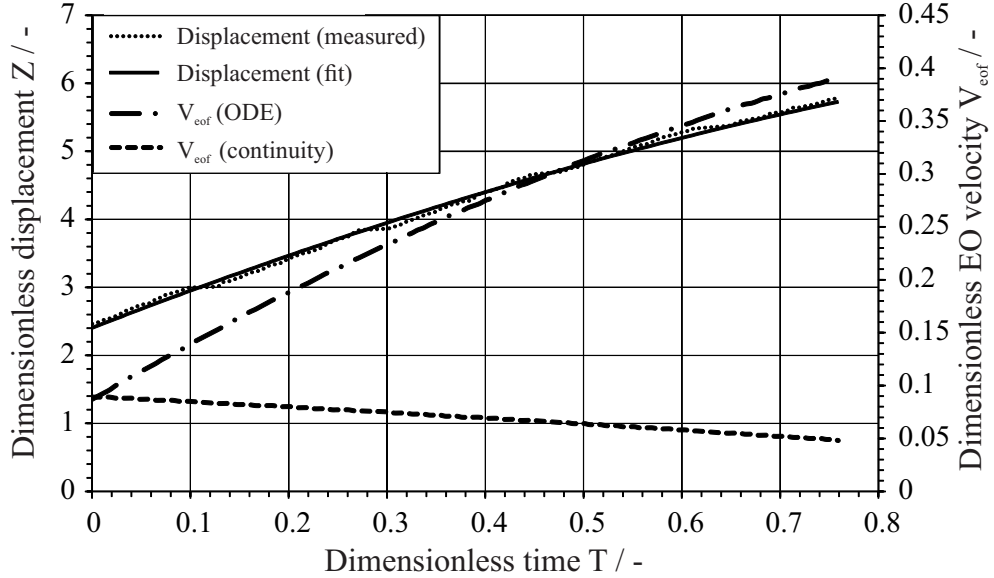
Figure 3.10: Typical outcome of an EOF experiment showing the dimensionless position of the air/liquid capillary interface and the accordingly computed dimensionless superficial EO velocities based on a pure continuity approach as well as based on centre-of-mass model of the fluidic setup eq. (3.18).

result is given by the solid circles. Here, we find that the V_{eof} considerably increases over time; first in a linear fashion and for later times it seems that a limiting value is achieved. Here, we should recall that we fitted the proportionality constant K_1 such that we achieve identical initial values of V_{eof} for both evaluation methods, the continuity assumption and the ODE. However, this fitting does not influence the trend over time which is, as we observe, very different for both approaches. An estimation shows that the consideration of the forces which arise from the capillary flow has only a minor contribution to the increasing V_{eof}. Hence, the massive change of V_{eof} is explained by Joule heating which, depending on the electric field strength and the electrolyte conductivity, results in a considerable temperature gradient along the packed bed. The temperature gradient, in turn, induces a density gradient which triggers a flow additionally to the EOF. We also measure temperature gradients by means of the temperature probes which are located at the outside of the packed bed tube. For high voltages ($\geq 2kV$) and high electrolyte conductivities (ionic strength

$\geq 10mM$), a rise in temperature is measured about 5 seconds after the voltage has been applied. For lower ionic strengths, the times before a temperature gradient is observed are considerably longer. Again, this gives only a rough insight into the time-dependent temperature distribution in the liquid due to the heat capacity of the packed bed tube and the convective and conductive heat transfer in the system. Nevertheless, these observations are qualitatively consistent with those which can be drawn from the comparison of the two different approaches to compute the EOF. However, the comparison of the two differently inferred EOFs demonstrates the influence of Joule heating, if present, with the correct time scale. Hence, we use the insight that we gain from the centre-of-mass-model to evaluate the experimental data in a range which excludes Joule heating effects.

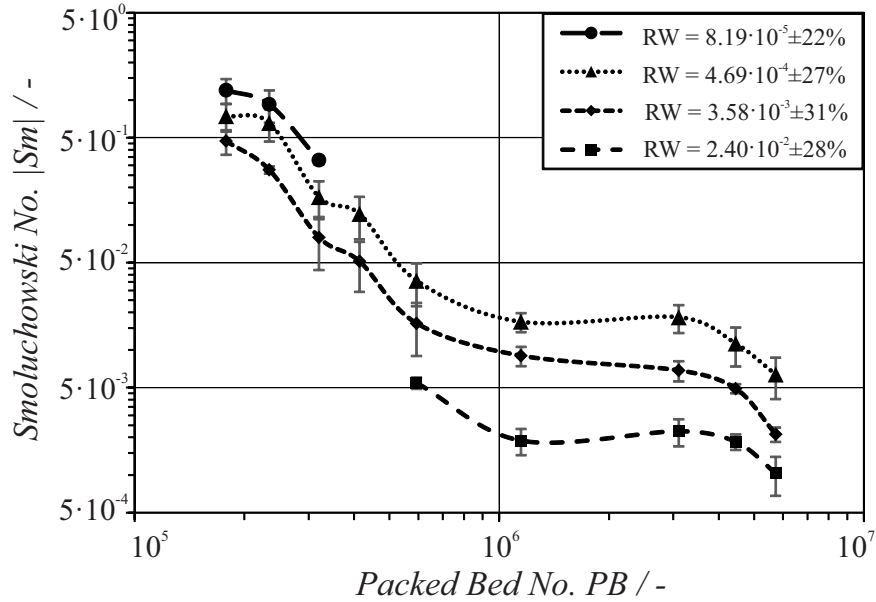Figure 3.11: Magnitude of the electroosmotic Smoluchowski no. *Sm.* vs. the Packed Bed no. *PB* for constant values of the Rice Whitehead no. *RW*.

Finally, the measured EOF is used along with the physicochemical and the packed bed parameters to build the dimensionless groups as defined in eq. (3.6). All diagrams are given on a logarithmic scale which is the standard way for phenomenological correlations

for flow phenomena in packed beds. Additionally, we indicate the standard deviation of the experiments, based on minimum 6 replicates for each point, with error bars.

Figure 3.11 shows results of the electroosmosis experiments plotted as functional relationship between the magnitude of the *Sm* and the *PB* for different values of the *RW*. Note that, due to the nature of our experiments, it is difficult to keep the *RW* constant while varying the other groups. Hence, we group the *RW* data such that we get a relatively narrow range variation but still span over several magnitudes. We see that for a given *RW*, the *Sm* decreases as the *PB* increases. The connections between the data points are for the sake of a better illustration and we realize that the track of the curves appears similar. The correlations, despite being plotted on a logarithm scale, do not appear linear. We rather find different intervals with different behaviours. At first, the scaling between the logarithmic values appears linear. Then, the *Sm* remains more or less constant as the *PB* increases. All curves show a regular behaviour in terms of their *RW*; i.e., the lower the *RW*, the higher the position of the curve on the y-axis. In terms of interpretation of the measured correlation, the behaviour appear counter-intuitive since one would think that the EOF flow should increase with an increasing *PB*. Nevertheless, we should recall that the *Sm* is the ratio of superficial to pore-scale electroosmotic velocity and the scaling of the groups is not the same as the scaling of the single phenomena. That is, if we increase the pore scale velocity in a complex packed bed, we cannot expect that the superficial velocity scales in the same fashion.

Figure 3.12 gives the correlation between the *Sm* and the *RW* for given *PB*. Generally, we observe that the *Sm* decreases as the *RW* increases. The correlation between the logarithmic values appears linear to good approximation. The observed behaviour clearly expresses the influence of the EDL overlap which happens for large Debye lengths in conjunction with small pore sizes (hydraulic diameters). Here, we should emphasize once more that a packed bed of spherical particles features pore conduits of a complex cross-sectional
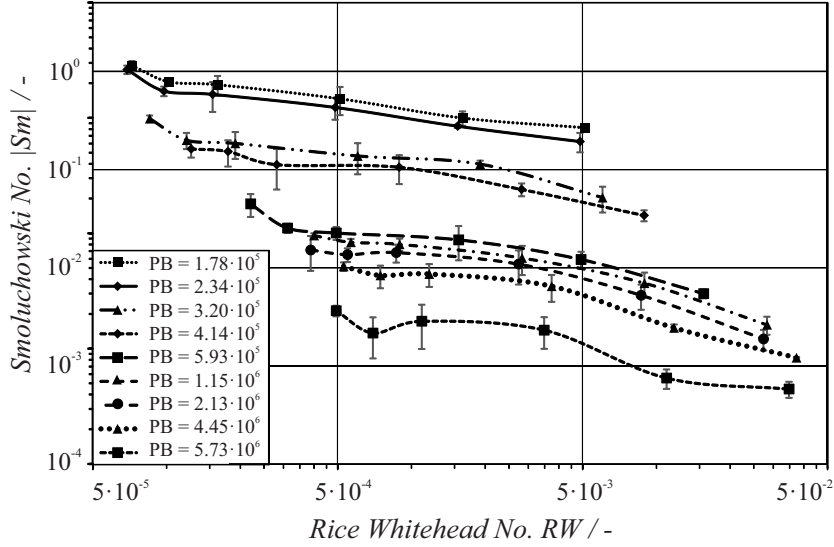
Figure 3.12: Electroosmotic Smoluchowski no. vs. the Rice Whitehead no. for different Packed Bed no.

form which size also varies in flow direction. In other words, there are always locations where an EDL overlap occurs even though the (averaged) hydraulic diameter gives no indication for this. We also find a regular arrangement of the curves in terms of the PB. That is, the lower the PB of a curve the higher its position on the y-axis.

Finally, we try different combinations of the dimensionless groups to derive a correlation which gives a quantitative expression for all physicochemical phenomena which are involved. It turns out that the data points on a logarithmic scale collapse, to good approximation, if we plot the Sm against the product of RW and PB as shown in figure 3.13. A linear regression results in

$$Sm \approx -3.10 \left(PB \cdot RW \right)^{-2/3} \tag{3.21}$$

with a value of 0.94 for the coefficient of determination. Alternatively, we insert the definitions of the dimensionless groups to obtain

$$v_{eof} \approx -3.10 \left(\frac{S_L l_D}{d_h^2} \right)^{-\frac{2}{3}} \frac{\zeta \varepsilon}{\mu} E, \tag{3.22}$$

83
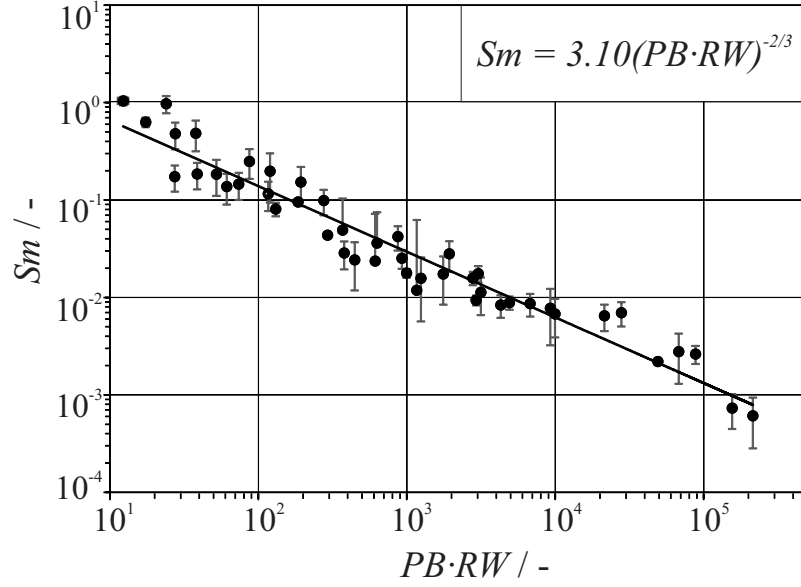
Figure 3.13: Electroosmotic Smoluchowski no. vs. the product of the Rice Whitehead no. and Packed Bed no.

or expressed in term of the measurable porosity and (known) particle size

$$v_{eof} \approx -\frac{1}{4} \left(\frac{\psi}{(1-\psi)} \frac{d_p}{M} \right)^{\frac{4}{3}} \left(l_D r_{pb}^2 \frac{\sum_{i=1}^{n} x_i d_i^2}{\sum_{i=1}^{n} x_i d_i^3} \right)^{-\frac{2}{3}} \frac{\zeta \varepsilon}{\mu} E, \tag{3.23}$$

which is only valid for a M factor similar to one.

3.6   Concluding remarks

In the current research, we derive a phenomenological correlation for the electroosmotic flow through packed beds of granular material in the spirit of the Blake-Kozeny correlation for pressure driven flow; i.e. based on dimensional reasoning. At first, we identify the relevant quantities which can be used for the qualitative description of the related phenomena. Then, we apply Buckingham Π theorem to establish a functional relationship between the relevant dimensionless group.

A detailed correlation for the functional relationship can only be obtained by selected set of experiments where we vary dimensionless groups while keeping others constant. A variety of packed beds made from binary mixtures of borosilicate micro spheres are prepared. The ratio of the particle diameter to the packed bed diameter is kept sufficiently low so that the influence of the packed tube on the electroosmotic flow can be neglected. The packed characterization reveals that the binary particle mixtures feature a different behaviour than packed beds which are made with homogenous particles. Numerous experiments are performed to infer the correlation between the dimensionless groups. In details, we use streaming current measurements to obtain an a detailed expression of the zeta potential of borosilicate in contact with an aqueous electrolyte of defined ionic strength and pH value. The measurements of electroosmotic flow in the packed beds over a wide range of parameters are performed where we utilize the motion of a capillary interface to measure the electroosmotic superficial velocity in the packed beds. We derive a dynamic model based on Newton's law to the translational center-of-mass motion of the fluidic system. The utilization of the model for the interpretation of the experimental results allows for a time evaluation whether there is an influence of Joule heating. This phenomenon induces density gradients in the liquids which, in turn, leads to considerable additional flow rates which falsifies the measurement of the electroosmotic flows. For data evaluation purposes, we consider only results which are not or only little influenced by Joule heating.

Finally, a phenomenological correlation between the dimensionless group is derived which has sufficient accuracy for many engineering applications such as the design of electroosmotic pumps for chromatography or various microfluidic applications. It should be noted that the correlation that we propose is not dependent on the substrate. The packed bed can be made of any granular matter which has a more or less spherical shape. Though, the packed parameter have to be known or experimentally derived. Also, the knowledge of the material's zeta potential in contact with the liquid has to be experimentally determined if the information is not available in literature. The main limitations of our correlation is that it does not account for Joule heating and the influence of the wall of the packed bed tube. Nevertheless, electroosmotic pumps can be designed such that these factors have no major relevance. This should be even easier for microchannels where there is more heat dissipation due to enhanced heat transfer over the channel walls which is a scaling effect of the high surface-to-volume-ratio. Here, the problem of a high particle to channel diameter (wall influence) could be mitigated by considering nano-size granular materials. But these questions can only be definitely answered in future works.

Chapter 4

Conclusions and Recommendations

4.1 Conclusions

The conclusions can be divided into two parts according to the two different thesis projects that constitutes this work.

4.1.1 Streaming potential and streaming current

The major results for the first part of the thesis concerned with the streaming current and streaming potential experiments can be summarized as below:

- We observe relatively high electrode transfer resistances for low value of the ionic strength (<1mM). The corresponding calculated exchange current densities clarify that the Ag/AgCl electrodes employed for this research are not fully reversible. However, we estimate the related error to be small compared to the standard deviations that we observe in the experiments.

- For low ionic strengths, our experiments clearly reveal that there are huge differences in the microchannel resistance depending on whether it is measured in or outside the microchannel. Also, there are different results whether the liquid flows or is at rest.

- An empirical correlation is obtained for the microchannel resistance as a function of the Reynolds number, the channel height and the ionic strength. The dependency is more prominent at lower ionic strength values and lower channel height which can be explained on the basis of surface conductivity.

- In line with the work of others, we observe an increase in surface conductivity with increasing ionic strength values and the smaller the channel height. Also, the observed surface conductivities are a magnitude of order larger than values obtained by using

Bikerman surface conductivity values which only accounts for the diffuse layer part of the EDL. This indicates that the major contribution to surface conductivity comes from the stagnant (Stern) layer.

- For the first time, we observe an increase in channel resistance with increase in Reynolds number for a given ionic strength. Our interpretation of the observed phenomenon is that the flow influences the surface conductivity.

- In the case of streaming current results, we generally observe linear correlations between zeta potential and logarithmic ionic strength. We also observe moderate differences in zeta potentials depending on whether a linear or a quadratic correlation between for the data processing is used. Additionally, the zeta potential magnitude decreases with increasing Reynolds number.

- In the case of streaming potential measurements, the absolute zeta potential decreases as the ionic strength increases. This statement holds for ionic strength values greater than 1 mM, but the opposite trend is observed for ionic strength of less than 1 mM. Only for in-situ measurements and a median Reynolds number, a linear correlation between zeta potential and the logarithmic ionic strength is recovered for all investigated channel heights.

- Finally, the zeta potential results are more affected by Reynolds number in the case of the streaming potential experiments in comparison to the streaming current experiment. A plausible explanation is that the convection does not only influence the induced SC (the EDL) but also the conduction current (via the channel resistance).

4.1.2   Electroosmosis in porous structures

In the same way, the following conclusions can be drawn from the research on electroosmotic flows through packed beds of granular materials:

- A phenomenological correlation is developed based on dimensional reasoning to correlate the superficial velocity in a packed bed to its characteristics and to the parameter of the aqueous electrolyte

- Different combinations of binary BSG micro spheres are used to produce packed beds with a wide range of porosities. Also, the size of the particles and the packed bed is chosen in such a way that the influence of the wall on the electroosmotic flow is minimized.

- The packed beds are characterized and different correlations between the porosity, equivalent particle diameter, hydraulic diameter and specific surface area are observed

- We derive a centre-of-mass model of the experimental setup which allows for the quantification of the electroosmotic flow by observation of the motion of a capillary interface connected to the packed bed. The model also allows for identification of the temporal influence of Joule heating in the packed bed.

4.2 Recommendations

The future work is divided in two separate parts:

4.2.1 Streaming potential and streaming current

- Further materials should be tested in order to investigate the influence of convection on the surface conductivity.

4.2.2 Electroosmosis in porous structures

The recommendations for the future work on electroosmosis in porous structures include:

- Packed beds with M factors which are significantly different to one would result in a more correlation with a wider range of applicability.

- It can be attempted to prepare packed beds with porosity range wider than 0.15-0.32 using different particle sizes and mixtures as in this work. Additionally, packed beds from non-spherical particles could be produced. Here, the question is whether the derived correlation still holds for such cases if equivalent spherical particle diameters are used.

- The experimental setup should be expanded so that a quantification of the temperature distribution in the packed bed is possible. This would give further important insights. Accordingly, it may be possible to add the temperature to the relevant quantities and to derive a revised phenomenological correlation which accounts for Joule heating as well.

- The research can be expanded such that packed bed of various length are fabricated in order to investigate the maximum pressure head which can be generated by the electroosmotic flow. Accordingly, the phenomenological model can be adapted to include the knowledge gained from these experiments.

Bibliography

[1] S. Wall. The history of electrokinetic phenomena. *Curr. Opin. Colloid Interface Sci.*, 15(3):119–124, 2010.

[2] J. Lyklema. Electrokinetics after Smoluchowski. *Colloids Surf., A*, 222(1-3):5–14, 2003.

[3] D. Henderson and D. Boda. Insights from theory and simulation on the electrical double layer. *Phys. Chem. Chem. Phys.*, 11(20):3822–30, 2009.

[4] J. Lyklema and M. Minor. On surface conduction and its role in electrokinetics. *Colloids Surf., A*, 140(1-3):33–41, 1998.

[5] J.J. Bikerman. Wissenschaftliche und technische Sammelreferate: Die Oberflächenleitfähigkeit und ihre Bedeutung. *Kolloid-Zeitschrift*, 72:100–108, 1935.

[6] F. Urban, H. L. White, and E. A. Strassner. Contribution to the theory of surface conductivity at solid-liquid interfaces. *J. Phys. Chem.*, 39(3):311–330, 1935.

[7] C.F. Zukoski IV and D.A. Saville. The interpretation of electrokinetic measurements using a dynamic model of the stern layer: I. The dynamic model. *J. Colloid Interface Sci.*, 114(1):32–44, 1986.

[8] C.F. Zukoski IV and D.A. Saville. The interpretation of electrokinetic measurements using a dynamic model of the stern layer: II. Comparisons between theory and experiment. *J. Colloid Interface Sci.*, 114(1):45–53, 1986.

[9] C. S. Mangelsdorf and L. R. White. Effects of stern-layer conductance on electrokinetic transport properties of colloidal particles. *J. Chem. Soc. Faraday Trans.*, 86(16):2859–2870, 1990.

[10] J. Lyklema, S. Rovillard, and J. D. Coninck. Electrokinetics: The properties of the stagnant layer unraveled. *Langmuir*, 14(20):5659–5663, 1998.

[11] R. J. Hunter. The significance of stagnant layer conduction in electrokinetics. *Adv. Colloid Interface Sci.*, 100–102:153–167, 2006.

[12] L. Joly, C. Ybert, and L. Trizac, E.and Bocquet. Hydrodynamics within the electric double layer on slipping surfaces. *Phys. Rev. Lett.*, 93(25):257805, 2004.

[13] R.J. Hunter. *Zeta Potential in Colloid Science: Principles and Applications*. Academic Press, 1981.

[14] R. A. van Wagenen and J. D. Andrade. Flat plate streaming potential investigations: Hydrodynamics and electrokinetic equivalency. *J. Colloid Interface Sci.*, 76:305–314, 1980.

[15] S. L. Walker, S. Bhattacharjee, E. M. V. Hoek, and M. Elimelech. A novel asymmetric clamping cell for measuring streaming potential of flat surfaces. *Langmuir*, 18(6):2193–2198, 2002.

[16] M. Sbaï, A. Szymczyk, P. Fievet, A. Sorin, A. Vidonne, S. Pellet-Rostaing, A. Favre-Reguillon, and M. Lemaire. Influence of the membrane pore conductance on tangential streaming potential. *Langmuir*, 19(21):8867–8871, 2003.

[17] S. Nishimura, K. Yao, M. Kodama, Y. Imai, K. Ogino, and K. Mishima. Electrokinetc study of synthetic smectites by flat plate streaming potential technique. *Langmuir*, 18(1):188–193, 2002.

[18] E. Donath and A. Voigt. Streaming current and streaming potential on structured surfaces. *J. Colloid Interface Sci.*, 109(1):122–139, 1986.

[19] G.K. Korpi and P.L. de Bruyn. Measurement of streaming potentials. *J. Colloid Interface Sci.*, 40(2):263–266, 1972.

[20] Z. He and F. Mansfeld. Exploring the use of electrochemical impedance spectroscopy (EIS) in microbial fuel cell studies. *Energy Environ. Sci.*, 2(2):215–219, 2009.

[21] M.J. Ariza, A. Cañas, and J. Benavente. Electrokinetic and electrochemical characterizations of porous membranes. *Colloids Surf., A*, 189(1):247–256, 2001.

[22] A. J. Tüdős, G. A. J. Besselink, and R. B. M. Schasfoort. Trends in miniaturized total analysis systems for point-of-care testing in clinical chemistry. *Lab Chip*, 1(2):83–95, 2001.

[23] P. S. Dittrich and A. Manz. Lab-on-a-chip: microfluidics in drug discovery. *Nat. Rev. Drug Discov.*, 5(3):210–218, 2006.

[24] A. V. Pattekar and M. V. Kothare. A microreactor for hydrogen production in micro fuel cell applications. *J. Microelectromech. Syst.*, 13(1):7–18, 2004.

[25] F. Qian, M. Baum, Q. Gu, and D. E. Morse. A 1.5 μl microbial fuel cell for on-chip bioelectricity generation. *Lab Chip*, 9(21):3076–3081, 2009.

[26] A.V. Delgado, F. González-Caballero, R.J. Hunter, L.K. Koopal, and J. Lyklema. Measurement and interpretation of electrokinetic phenomena. *J. Colloid Interface Sci.*, 309(2):194–224, 2007.

[27] X. Xuan. Joule heating in electrokinetic flow. *ELECTROPHORESIS*, 29(1):33–43, 2008.

[28] L. Szekely and R. Freitag. Study of the electroosmotic flow as a means to propel the mobile phase in capillary electrochromatography in view of further miniaturization of capillary electrochromatography systems. *ELECTROPHORESIS*, 26(10):1928–1939, 2005.

[29] M. S. Bello. Electrolytic modification of a buffer during a capillary electrophoresis run. *J. Chromatogr. A*, 744(1):81–91, 1996.

[30] B.J. Kirby and E.F. Hasselbrink Jr. Zeta potential of microfluidic substrates: 1. Theory, experimental techniques and effects on separations. *ELECTROPHORESIS*, 25(2):187–202, 2004.

[31] A. Ramos, H. Morgan, N.G. Green, and A. Castellanos. Ac electric-field-induced fluid flow in microelectrodes. *J. Colloid Interface Sci.*, 217(2):420–422, 1999.

[32] C. Zhao and C. Yang. Advances in electrokinetics and their applications in micro/nano fluidics. *Microfluid. Nanofluid.*, 13(2):179–203, 2012.

[33] F. H. J. van der Heyden, D. J. Bonthuis, D. Stein, C. Meyer, and C. Dekker. Electrokinetic energy conversion efficiency in nanofluidic channels. *Nano Lett.*, 6(10):2232–2237, 2006.

[34] C. L.A. Berli. Electrokinetic energy conversion in microchannels using polymer solutions. *J. Colloid Interface Sci.*, 349(1):446–448, 2010.

[35] H v. Helmholtz. Studien über electrische Grenzschichten. *Ann. Phys. und Chem.*, 7(7):337–382, 1879.

[36] M. Chun, M. Shim, and N. Choi. Fabrication and validation of a multi-channel type microfluidic chip for electrokinetic streaming potential devices. *Lab Chip*, 6(2):302–309, 2006.

[37] Y. Min, N. Pesika, J. Zasadzinski, and J. Israelachvili. Studies of bilayers and vesicle adsorption to solid substrates: development of a miniature streaming potential apparatus (spa). *Langmuir*, 26(11):8684–8689, 2010.

[38] P. J. Sides and D. C. Prieve. Surface conductivity and the streaming potential near a rotating disk-shaped sample. *Langmuir*, 29(44):13427–13432, 2013.

[39] Z. Adamczyk, M. Zembala, P. Warszyalski, and B. Jachimska. Characterization of polyelectrolyte multilayers by the streaming potential method. *Langmuir*, 20(24):10517–10525, 2004.

[40] V. Tandon, S. K. Bhagavatula, W. C. Nelson, and B. J. Kirby. Zeta potential and electroosmotic mobility in microfluidic devices fabricated from hydrophobic polymers: 1. The origins of charge. *ELECTROPHORESIS*, 29(5):1092–1101, 2008.

[41] M.L. Gupta, K. Brunson, A. Chakravorty, P. Kurt, J.C. Alvarez, F. Luna-Vera, and K. J. Wynne. Quantifying surface-accessible quaternary charge for surface modified coatings via streaming potential measurements. *Langmuir*, 26(11):9032–9039, 2010.

[42] M. Dabkowska and Z. Adamczyk. Human serum albumin monolayers on mica: Electrokinetic characteristics. *Langmuir*, 28(44):15663–15673, 2012.

[43] A. D. Dussaud, P. C. Breen, and K. Koczo. Characterization of the deposition of silicone copolymers on keratin fibers by streaming potential measurements. *Colloids Surf., A*, 434(0):102–109, 2013.

[44] M. v. Smoluchowski. Versuch einer Mathematischen Theorie der Koagulationskinetik kolloider Lösungen. *Z. Phys. Chem.*, 92:129–168, 1918.

[45] F. Fairbrother and H. Mastin. CCCXII. – studies in electro-endosmosis. part I. *J. Chem. Soc., Transactions*, 125:2319–2330, 1924.

[46] P.J. Scales, F. Grieser, and T.W. Healy. Electrokinetics of the silica-solution interface: A flat plate streaming potential study. *Langmuir*, 8:965–974, 1992.

[47] A. Crespy, A. Boleve, and A. Revil. Influence of the Dukhin and Reynolds numbers on the apparent zeta potential of granular porous media. *J. Colloid Interface Sci.*, 305(1):188–194, 2007.

[48] C. Werner, H. Körber, R. Zimmermann, S. Dukhin, and H. Jacobasch. Extended electrokinetic characterization of flat solid surfaces. *J. Colloid Interface Sci.*, 208:329–346, 1998.

[49] J. Th G. Overbeek. Thermodynamics of electrokinetic phenomena. *J. Colloid Sci.*, 8(4):420–427, 1953.

[50] H. Falahati, L. Wong, L. Davarpanah, A. Garg, P. Schmitz, and D.P.J. Barz. The zeta potential of pmma in contact with electrolytes of various conditions: Theoretical and experimental investigation. *ELECTROPHORESIS*, 35:870–882, 2014.

[51] L. V. Gorelik. Investigation of dynamic streaming potential by dimensional analysis. *J. Colloid Interface Sci.*, 274(2):695–700, 2004.

[52] A. Boleve, A. Crespy, A. Revil, F Janod, and J.-L. Mattiuzzo. Streaming potentials of granular media: Influence of the dukhin and reynolds numbers. *J. Geophys. Res.: Solid Earth (1978–2012)*, 112(B8), 2007.

[53] F. Lu, J. Yang, and D. Y. Kwok. Flow field effect on electric double layer during streaming potential measurements. *J. Phys. Chem. B*, 108(39):14970–14975, 2004.

[54] C.H. Hamann, A. Hamnett, and W. Vielstich. *Electrochemistry*. Wiley-VCH, Weinheim, 2007.

[55] S.S. Dukhin. Electrokinetic phenomena of the second kind and their applications. *Adv. Colloid Interface Sci.*, 35(0):173–196, 1991.

[56] J. Lyklema, S. S. Dukhin, and V. N. Shilov. The relaxation of the double layer around colloidal particles and the low-frequency dielectric dispersion: Part I. Theoretical considerations. *J. Electroanal. Chem.*, 143(1):1–21, 1983.

[57] J. Ward-Smith. *Internal fluid flow - The fluid dynamics of flow in pipes and ducts*. Clarendon Press, Oxford, 1980.

[58] H. Ohshima, editor. *Electrical Phenomena at Interfaces and Biointerfaces: Fundamentals in Nano-Bio- and Environmental Sciences.* John Wiley & Sons, Hoboken, N.J., 2011.

[59] E. Barsoukov and J. R. Macdonald. *Impedance spectroscopy: Theory, experiment, and applications.* John Wiley & Sons, Hoboken, N.J., 2005.

[60] D.A. Saville. Electrohydrodynamics: The Taylor–Melcher leaky dielectric model. *Annu. Rev. Fluid Mech.*, 29:27–64, 1997.

[61] P. Leroy and A. Revil. A triple-layer model of the surface electrochemical properties of clay minerals. *J. Colloid Interface Sci.*, 270(2):371–380, 2004.

[62] D. P. J. Barz, M. J. Vogel, and P. H. Steen. Determination of the zeta potential of porous substrates by droplet deflection. I. The influence of ionic strength and pH value of an aqueous electrolyte in contact with a borosilicate surface. *Langmuir*, 25(3):1842–1850, 2009.

[63] P. R. Johnson. A comparison of streaming and microelectrophoresis methods for obtaining the ζ potential of granular porous media surfaces. *J. Colloid Interface Sci.*, 209(1):264–267, 1999.

[64] S. F. Alkafeef, R. J. Gochin, and A. L. Smith. Measurement of the electrokinetic potential at reservoir rock surfaces avoiding the effect of surface conductivity. *Colloids Surf., A*, 159(2):263–270, 1999.

[65] M. Zembala and Z. Adamczyk. Measurements of streaming potential for mica covered by colloid particles. *Langmuir*, 16(4):1593–1601, 2000.

[66] F.F. Reuss. Sour un nouvel effet de l'électricité galvanique. *Mémoires de la societé impériale des naturalistes de Moscou*, 2:327–337, 1809.

[67] L.C. Waters, S.C. Jacobson, N. Kroutchinina, J. Khandurina, R.S. Foote, and J.M. Ramsey. Microchip device for cell lysis, multiplex PCR amplification, and electrophoretic sizing. *Anal. Chem.*, 70(1):158–162, 1998.

[68] D. P. J. Barz and P. Ehrhard. Model and verification of electrokinetic flow and transport in a micro-electrophoresis device. *Lab Chip*, 5(9):949–958, 2005.

[69] W. L. Dong and C. Young-Ho. A continuous electrical cell lysis device using a low dc voltage for a cell transport and rupture. *Sens. Actuators B*, 124(1):84–89, 2007.

[70] S. C. Jacobson and J. M. Ramsey. Electrokinetic focusing in microfabricated channel structures. *Anal. Chem.*, 69(16):3212–3217, 1997.

[71] M.H. Oddy, J.G. Santiago, and J.C. Mikkelsen. Electrokinetic instability micromixing. *Anal. Chem.*, 73:5822–5832, 2001.

[72] A. Ould El Moctar, N. Aubry, and J. Batton. Electro–hydrodynamic micro–fluidic mixer. *Lab Chip*, 3:273–280, 2003.

[73] D. P. J. Barz, H. Zadeh, and P. Ehrhard. Measurements and simulations of time-dependent flow fields within an electrokinetic micromixer. *J. Fluid Mech.*, 676:265–293, 2011.

[74] H. Bockelmann, V. Heuveline, and D. P.J. Barz. Optimization of an electrokinetic mixer for microfluidic applications. *Biomicrofluidics*, 6(2):024123, 2012.

[75] J.S. Hu and C.Y.H. Chao. A study of the performance of microfabricated electroosmotic pump. *Sens. Actuators A*, 135(1):273–282, 2007.

[76] L. M. Lazar and B. L. Karger. Multiple open-channel electroosmotic pumping system for microfluidic sample handling. *Anal. Chem.*, 74(24):6259–6268, 2002.

[77] Q. Pu and S. Liu. Microfabricated electroosmotic pump for capillary-based sequential injection analysis. *Anal. Chim. Acta*, 511(1):105–112, 2004.

[78] T. Glawdel, C. Elbuken, L. E.J. Lee, and C. L. Ren. Microfluidic system with integrated electroosmotic pumps, concentration gradient generator and fish cell line (RTgill-W1) – towards water toxicity testing. *Lab Chip*, 9(22):3243–3250, 2009.

[79] J. Borowsky, Q. Lu, and G. E. Collins. High pressure electroosmotic pump based on a packed bed planar microchip. *Sens. Actuators B*, 131(1):333–339, 2008.

[80] J. F. Borowsky, B. C. Giordano, Q. Lu, A. Terray, and G. E. Collins. Electroosmotic flow-based pump for liquid chromatography on a planar microchip. *Anal. Chem.*, 80(21):8287–8292, 2008.

[81] X. Wang, C. Cheng, S. Wang, and S. Liu. Electro osmotic pumps and their applications in microfluidic systems. *Microfluid. Nanofluid.*, 6:145–162, 2009.

[82] M. G. Cikalo, K. D. Bartle, M. M. Robson, P. Myers, and M. R. Euerby. Capillary electrochromatography. tutorial review. *Analyst*, 123(7):87R–102R, 1998.

[83] J. Simal-Gándara. The place of capillary electrochromatography among separation techniques – a review. *Crit. Rev. in Anal. Chem.*, 34(2):85–94, 2004.

[84] S.L. Zeng, C.H. Chen, J.C. Mikkelsen, and J.G. Santiago. Fabrication and characterization of electroosmotic micropumps. *Sens. Actuators B*, 79:107–114, 2001.

[85] S. Zeng, C.-H. Chen, J. G. Santiago, J.-R. Chen, R. N. Zare, J. A. Tripp, Frantisek S., and J. M.J. Fréchet. Electroosmotic flow pumps with polymer frits. *Sens. Actuators B*, 82(2–3):209–212, 2002.

[86] D. S. Reichmuth, G. S. Chirica, and B. J. Kirby. Increasing the performance of high-pressure, high-efficiency electrokinetic micropumps using zwitterionic solute additives. *Sens. Actuators B*, 92(1):37–43, 2003.

[87] Y. Kang, S. C. Tan, C. Yang, and X. Huang. Electrokinetic pumping using packed microcapillary. *Sens. Actuators A*, 133(2):375 –382, 2007.

[88] W. Shin, J. M. Lee, R. K. Nagarale, S. J. Shin, and A. Heller. A miniature, nongassing electroosmotic pump operating at 0.5V. *J. Am. Chem. Soc.*, 133(8):2374–2377, 2011.

[89] S. Yao, D.E. Hertzog, S. Zeng, J.C. Mikkelesen Jr., and J.G. Santiago. Porous glass electroosmotic pumps: design and experiments. *J. Colloid Interface Sci.*, 268:143–153, 2003.

[90] K. Daejoong, D. P. Jonathan, and G. S. Juan. High flow rate per power electroosmotic pumping using low ion density solvents. *Sens. Actuators A*, 141(1):201–212, 2008.

[91] P. Wang, Z. Chen, and H.-C. Chang. A new electro-osmotic pump based on silica monoliths. *Sens. Actuators B*, 113(1):500–509, 2006.

[92] J. A. Tripp, F. Svec, J. M. J. Fréchet, S. Zeng, J. C. Mikkelsen, and J. G. Santiago. High-pressure electroosmotic pumps based on porous polymer monoliths. *Sens. Actuators B*, 99(1):66 –73, 2004.

[93] C. Gu, Z. Jia, Z. Zhu, C. He, W. Wang, A. Morgan, J. J. Lu, and S. Liu. Miniaturized electroosmotic pump capable of generating pressures of more than 1200 bar. *Anal. Chem.*, 84(21):9609–9614, 2012.

[94] K. Kwon, C.-W. Park, and D. Kim. High-flowrate, compact electroosmotic pumps with porous polymer track-etch membranes. *Sens. Actuators A*, 175:108–115, 2012.

[95] Y. Ai, S. E. Yalcin, D. Gu, O. Baysal, H. Baumgart, S. Qian, and A. Beskok. A low-voltage nano-porous electroosmotic pump. *J. Colloid Interface Sci.*, 350(2):465–470, 2010.

[96] H. Leese and D. Mattia. Electroosmotic flow in nanoporous membranes in the region of electric double layer overlap. *Microfluid. Nanofluid.*, 16(4):711–719, 2014.

[97] Z. Cao, L. Yuan, Y.-F. Liu, S. Yao, and L. Yobas. Microchannel plate electro-osmotic pump. *Microfluid. Nanofluid.*, 13(2):279–288, 2012.

[98] C. Wang, L. Wang, X. Zhu, Y. Wang, and J. Xue. Low-voltage electroosmotic pumps fabricated from track-etched polymer membranes. *Lab Chip*, 12(9):1710–1716, 2012.

[99] R. K. Niven. Physical insight into the Ergun and Wen & Yu equations for fluid flow in packed and fluidised beds. *Chem. Eng. Sci.*, 57(3):527–534, 2002.

[100] F.A.L. Dullien. Single phase flow trough porous media and pore structure. *Chem. Eng. J.*, 10:1–34, 1975.

[101] R. B. Bird, W. E. Stewart, and E. N. Lightfoot. *Transport phenomena.* John Wiley & Sons, 2007.

[102] P. Mazur and J.Th.G. Overbeek. On electro-osmosis and streaming-potentials in diaphragms. II. General quantitative relationship between electro-kinetic effects. *Rec. Trav. Chim.*, 70:83–91, 1951.

[103] P. T. Vallano and V. T. Remcho. Modeling interparticle and intraparticle (perfusive) electroosmotic flow in capillary electrochromatography. *Anal. Chem.*, 72:4255–4265, 2000.

[104] S. Yao and J.G. Santiago. Porous glass electroosmotic pumps: Theory. *J. Colloid Interface Sci.*, 268:133–142, 2003.

[105] N. Scales and R.N. Tait. Modeling electroosmotic and pressure-driven flows in porous microfluidic devices: Zeta potential and porosity changes near the channel walls. *J. Chem. Phys.*, 125:094714–1–094714–12, 2006.

[106] D. P.J. Barz and P. H. Steen. A dynamic model of the electroosmotic droplet switch. *Phys. Fluids*, 25(9):097104, 2013.

[107] M. v. Smoluchowski. Contribution à la théorie de l'endosmose électrique et de quelques phenoménes corrélatifs. *Bull. Int. Acad. Sci. Cracovie*, 8:182–200, 1903.

[108] B.J. Kirby and E.F. Hasselbrink Jr. Zeta potential of microfluidic substrates: 2. Data for polymers. *ELECTROPHORESIS*, 25(2):203–213, 2004.

[109] D. P. J. Barz, M. J. Vogel, and P. H. Steen. Determination of the zeta potential of substrates by droplet deflection: II. Generation of electrokinetic flow in a non–polar liquid. *Langmuir*, 26(5):3126–3133, 2010.

[110] D. Mehta and M. C. Hawley. Wall effect in packed columns. *Ind. Eng. Chem. Process Des. Dev.*, 8(2):280–282, 1969.

[111] M.M. Denn. *Process Fluid Mechanics.* Prentice-Hall, Englewood Cliffs, NJ, 1980.

[112] J. J. Benbow, N. Ouchiyama, and J. Bridgwater. On the prediction of extrudate pore structure from particle size. *Chem. Eng. Commun.*, 62(1-6):203–220, 1987.

[113] N. Ouchiyama and T. Tanaka. Porosity of a mass of solid particles having a range of sizes. *Ind. Eng. Chem. Fundam.*, 20(1):66–71, 1981.

[114] E. Buckingham. On physically similar systems; illustrations of the use of dimensional equations. *Phys. Rev. IV*, 4:345–376, 1914.

[115] C.L. Rice and R. Whitehead. Electrokinetic flow in a narrow capillary. *J. Phys. Chem.*, 11:4017–4024, 1965.

[116] G.Y. Tang, C. Yang, J.C. Chai, and H.Q. Gong. Joule heating effect on electroosmotic flow and mass species transport in a microcapillary. *Int. J. Heat Mass Transfer*, 47:215–227, 2004.

[117] P.C. Carman. *Flow of gases through porous media.* Butterworths, London, 1956.

[118] A.A. Zick and G.M Homsy. Stokes flow through periodic arrays of spheres. *J. Fluid Mech.*, 115:13–26, 1982.

[119] F. Macdonald, M.S. El-Sayed, K. Mow, and F.A.L. Dullien. Flow through porous media-the Ergun equation revisited. *Ind. Eng. Chem. Fundam.*, 18:199–208, 1979.

[120] H. T. Xue, Z. N. Fang, Y. Yang, J. P. Huang, and L. W. Zhou. Contact angle determined by spontaneous dynamic capillary rises with hydrostatic effects: Experiment and theory. *Chem. Phys. Lett.*, 432(1):326–330, 2006.

[121] G. Martic, F. Gentner, D. Seveno, D. Coulon, J. De Coninck, and T. D. Blake. A molecular dynamics simulation of capillary imbibition. *Langmuir*, 18(21):7971–7976, 2002.

[122] A. Siebold, M. Nardin, J. Schultz, A. Walliser, and M. Oppliger. Effect of dynamic contact angle on capillary rise phenomena. *Colloids Surf., A*, 161(1):81–87, 2000.

[123] R. L. Hoffman. A study of the advancing interface. I. Interface shape in liquid – gas systems. *J. Colloid Interface Sci.*, 50(2):228–241, 1975.

[124] T.-S. Jiang, O. H. Soo-Gun, and J. C. Slattery. Correlation for dynamic contact angle. *J. Colloid Interface Sci.*, 69(1):74–77, 1979.

[125] A. A. Saha and S. K. Mitra. Effect of dynamic contact angle in a volume of fluid (VOF) model for a microfluidic capillary flow. *J. Colloid Interface Sci.*, 339(2):461–480, 2009.

[126] T. D. Blake. The physics of moving wetting lines. *J. Colloid Interface Sci.*, 299(1):1–13, 2006.

[127] T. D. Blake and J. M. Haynes. Kinetics of liquid/liquid displacement. *J. Colloid Interface Sci.*, 30(3):421–423, 1969.

[128] M. N. Popescu, J. Ralston, and R. Sedev. Capillary rise with velocity-dependent dynamic contact angle. *Langmuir*, 24(21):12710–12716, 2008.

[129] S. E. Van den Bosch, S. Heemstra, J. C. Kraak, and H. Poppe. Experiences with packed capillary electrochromatography at ambient pressure. *J. Chromatogr. A*, 755(2):165–177, 1996.

[130] B. Behnke, E. Grom, and E. Bayer. Evaluation of the parameters determining the performance of electrochromatography in packed capillary columns. *J. Chromatogr. A*, 716(1):207–213, 1995.

[131] I. Gusev, X. Huang, and C. Horváth. Capillary columns with in situ formed porous monolithic packing for micro high-performance liquid chromatography and capillary electrochromatography. *J. Chromatogr. A*, 855(1):273–290, 1999.

[132] R. Asiaie, X. Huang, D. Farnan, and C. Horvath. Sintered octadecylsilica as monolithic column packing in capillary electrochromatography and micro high-performance liquid chromatography. *J. Chromatogr. A*, 806(2):251–263, 1998.

[133] R. P. Dias, J. A. Teixeira, M. G. Mota, and A. I. Yelshin. Particulate binary mixtures: dependence of packing porosity on particle size ratio. *Ind. Eng. Chem. Res.*, 43(24):7912–7919, 2004.

[134] R. P. Dias, C. S. Fernandes, J. A. Teixeira, M. Mota, and A. Yelshin. Permeability analysis in bisized porous media: Wall effect between particles of different size. *J. Hydrol.*, 349(3):470–474, 2008.

[135] R. Dias, J. A. Teixeira, M. Mota, and A. Yelshin. Tortuosity variation in a low density binary particulate bed. *Sep. Purif. Technol.*, 51(2):180–184, 2006.

[136] R. Dias, J. A Teixeira, M. Mota, and A. Yelshin. Preparation of controlled particulate mixtures with glass beads of different sizes. *Sep. Purif. Technol.*, 37(1):69–80, 2004.

[137] E. Guyon, L. Oger, and T.J. Plona. Transport properties in sintered porous media composed of two particle sizes. *J. Phys. D. Appl. Phys.*, 20(12):1637, 1987.

[138] M. Mota, J. A. Teixeira, W. R. Bowen, and A. Yelshin. Binary spherical particle mixed beds: porosity and permeability relationship measurement. 2001.

[139] A. B. Yu and N. Standish. Estimation of the porosity of particle mixtures by a linear-mixture packing model. *Ind. Eng. Chem. Res.*, 30(6):1372–1385, 1991.

[140] A. de Klerk. Voidage variation in packed beds at small column to particle diameter ratio. *AIChE J.*, 49(8):2022–2029, 2003.